The proton charge radius

H. Gao and M. Vanderhaeghen

Rev. Mod. Phys. **94**, 015002 — Published 21 January 2022

DOI: 10.1103/RevModPhys.94.015002

The proton charge radius

H. Gao

Department of Physics,
Duke University and the Triangle Universities Nuclear Laboratory,
Science Drive, Durham, NC 27708,
USA

M. Vanderhaeghen

Institut für Kernphysik and PRISMA$^+$ Cluster of Excellence,
Johannes Gutenberg Universität, D-55099 Mainz,
Germany

(Dated: October 8, 2021)

Nucleons (protons and neutrons) are the building blocks of atomic nuclei and are responsible for more than 99% of the visible matter in the universe. Despite decades of efforts in studying its internal structure, there are still a number of puzzles surrounding the proton such as its spin and charge radius. Accurate knowledge about the proton charge radius is not only essential for understanding how quantum chromodynamics (QCD) works in the non-perturbative region, but also important for bound state quantum electrodynamics (QED) calculations of atomic energy levels. It also has an impact on the Rydberg constant, one of the most precisely measured fundamental constants in nature. This article reviews the latest situation concerning the proton charge radius in light of the new experimental results from both atomic hydrogen spectroscopy and electron scattering measurements, with particular focus on the latter. We also present theoretical backgrounds and recent developments concerning the determination of the proton charge radius using different experimental techniques. We discuss upcoming experiments, and briefly mention the deuteron charge radius puzzle at the end.

CONTENTS

I. INTRODUCTION

Nucleons (protons and neutrons) are the building blocks of atomic nuclei and are responsible for more than 99% of the visible matter in the universe. The force that is responsible for binding nucleons into nuclei – and responsible for the composite nature of nucleons – is the strong force, one of the four fundamental forces in nature. The ultimate goal of modern nuclear physics is to predict properties of nucleons, atomic nuclei and nuclear reactions from the first principles of Quantum Chromodynamics (QCD), the theory of the strong interaction with quarks and gluons as the fundamental degrees of freedom. While QCD has been well tested experimentally at high energies where perturbative calculations can be carried out, how QCD works in the low-energy region still requires much better understanding. Nucleons therefore become important QCD laboratories through studies of their rich internal structure.

Despite decades of efforts studying the internal structure of the proton, there are still a number of puzzles and open questions surrounding the proton such as its spin and charge radius. The so-called "Proton Spin Crisis" was triggered by the European Muon Collaboration (EMC) experiment (Ashman *et al.*, 1988) in which polarized muons were scattered off polarized nucleons – discovering that quarks' spins contribute little to the proton spin. After more than three decades of polarization experiments worldwide, the emerging picture about the proton spin is that the quark spin contributes about a third to the proton spin with comparable contribution likely by the spins of the gluons, and the remaining from the orbital angular momenta of the quarks and gluons inside. For a recent review of the proton spin, we refer readers to (Ji *et al.*, 2020; Kuhn *et al.*, 2009).

The proton mass decomposition has been a topic of increasing interest in recent years motivated by the experimental capability offered by the energy upgraded 12-GeV CEBAF at Jefferson Lab (Dudek *et al.*, 2012), and the future Electron-Ion Collider (EIC) (Accardi *et al.*, 2016) to be built at the Brookhaven National Laboratory. There exists various approaches for the proton mass decomposition (Ji, 1995; Lorcé, 2018; Metz *et al.*, 2020; Shifman *et al.*, 1978). Following Ji's decomposition, the quark mass contribution to the proton mass is found to be $\sim$ 11%, trace anomaly is about 22%, and the rest is due to the quark and gluon energy (Gao *et al.*, 2015). Near-threshold electro- and photo-production cross sections of J/Ψ and Υ particles (Gryniuk *et al.*, 2020; Gryniuk and Vanderhaeghen, 2016; Hatta and Yang, 2018; Kharzeev *et al.*, 1999) from the proton have been proposed as effective ways to access the trace anomaly contribution, and experiments (Gryniuk *et al.*, 2020; Jefferson Lab Proposal E12-12-006, Spokespersons: K. Hafidi, X. Qian, N. Sparveris, Z.-E. Meziani (contact), and Z. W. Zhao, 2012) are being planned at Jefferson Lab and at the future EIC.

The proton root-mean-square (rms) charge radius (a.k.a. proton charge radius) is a quantity that is not only of importance to QCD, but also for bound state QED calculations of atomic energy levels. It additionally has a direct impact on the determination of the Rydberg constant, one of the most well-known fundamental quantities in Nature. Conventionally, the proton charge radius can be determined from electron-proton elastic scattering, a method pioneered by Hofstadter, and atomic spectroscopic measurements using ordinary hydrogen atoms. In the former case, one determines the proton electric form factor from scattering cross sections, from which one then extracts the proton charge radius. In the latter case, experimentally measured atomic transitions combined with state-of-the-art QED calculations allow for an extraction of the proton charge radius.

The proton charge radius puzzle originated in 2010 following a new ultra-precise determination of the proton charge radius from muonic hydrogen Lamb shift measurements (Pohl *et al.*, 2010), which reported a radius value of 0.84184(67) fm. This new result is 4% smaller than the recommended value of 0.8775(51) fm by the Committee on Data for Science and Technology (CODATA-2010) (Mohr, 2012) based on results from electron-proton scattering and ordinary hydrogen spectroscopy measurements, and represents a 7σ difference. In the last ten years, major progress has been made in resolving this puzzle, which is the focus of this review paper. While we cover the latest progress in atomic spectroscopy concerning the proton charge radius, special emphasis will be given in this review to the progress from lepton scattering, and its associated challenges. The rest of the paper is organized as the following. We set the stage and introduce the proton charge radius puzzle in Section II. In Section III we describe how the charge radius is defined, how it can be properly understood in terms of a quark charge distribution, and how it is connected to the quark structure of the proton. We subsequently describe the experimental techniques in determining the proton charge radius from elastic electron-proton scattering in Section III and from atomic hydrogen spectroscopy in Section IV. Section V and VI review the results from the recent lepton scattering and spectroscopy measurements, respectively. In Section VII, we review ongoing and planned lepton scattering experiments. Section VIII provides a brief introduction of another charge radius puzzle which concerns the deuteron before we conclude in Section IX.

II. THE PROTON CHARGE RADIUS PUZZLE

The proton charge radius puzzle developed and quickly became widely known in 2010 when the CREMA collaboration (Pohl *et al.*, 2010) reported the first determination of the proton charge radius from a muonic hydrogen spectroscopic method ever – giving a value of 0.84184(67) fm by measuring the transition between the $2S_{1/2}(F = 1)$ and the $2P_{3/2}(F = 2)$ energy levels. It was the most precise measurement at the time, but 7 σ smaller than the 2010 CODATA recommended value of 0.8775(51) fm (Mohr, 2012). In 2013, the CREMA collaboration reported (Antognini *et al.*, 2013a) a value of 0.84087(39) fm from combined analyses of the original transition they reported in 2010 together with a different transition between the $2S_{1/2}(F = 0)$ and the $2P_{3/2}(F = 1)$ levels. See (Carlson, 2015; Pohl *et al.*, 2013) for some early reviews. From the electron scattering community, two values of the proton charge radius were reported around the same time, and they are 0.8791(79) fm by Bernauer *et al.* (Bernauer *et al.*, 2010), and 0.875 (10) fm by Zhan *et al.* (Zhan *et al.*, 2011) – both were included in the 2010 CODATA compilation and are in excellent agreement with its recommended value. The muonic hydrogen results (Antognini *et al.*, 2013a; Pohl *et al.*, 2010) had not been included into the CODATA compilation until its most recent release (Tiesinga *et al.*, 2021).

The release of the proton charge radius result from a muonic hydrogen spectroscopic measurement by the CREMA collaboration in 2010 (Pohl *et al.*, 2010) triggered a major proton charge radius puzzle. However, there was a puzzle even before that, known perhaps only to a much smaller community. An important motivation to improve the precision in determining the proton charge radius from electron scattering experiments is for precision tests of QED through hydrogen Lamb shift measurements. The standard hydrogen Lamb shift measurement probes the 1057 MHz fine structure transition between the $2S_{1/2}$ and $2P_{1/2}$ states – and can be calculated to high precision with higher-order corrections in QED with the proton rms charge radius as an important input for finite size and other hadronic structure contributions. However, the two most precise values from electron scattering experiments in the literature before 2010 – each with a relative uncertainty of less than 1.5% but differing by about 7% (relative) – are $r_p = 0.805(11)$ fm (Hand and Wilson, 1963) and $r_p = 0.862(12)$ fm (Simon *et al.*, 1980). The result from (Hand and Wilson, 1963) includes data from several experiments. In the late 1990s, several groups published high precision results from hydrogen spectroscopic measurements (Berkeland, 1995; Bourzeix *et al.*, 1996; Hagley and Pipkin, 1994; Weitz *et al.*, 1994; van Wijngaarden *et al.*, 1998), and these results supported a larger value of the proton charge radius (0.862 fm) when compared with QED predictions including the two-loop binding effects. Melnikov and van Ritbergen (Melnikov, 2000) calculated the three-loop slope of the Dirac form factor – the last known contribution to the hydrogen energy levels at order $m\alpha^7$ – and extracted a proton charge radius value of 0.883(14) fm combining the QED calculation of the $1S$ Lamb shift and the experimental measurement (Schwob *et al.*, 1999).

III. ELASTIC ELECTRON-PROTON SCATTERING

Electron scattering has proved to be an effective and clean way to probe the internal structure of the nucleon – as the lepton vertex is well described by QED – and higher-order contributions are suppressed compared with the leading-order, one-photon-exchange contribution. This has been demonstrated by the Nobel Prize winning electron-proton elastic scattering experiment carried out by Robert Hofstadter and collaborators in the 1950s at the Stanford University (Hofstadter and McAllister, 1955; McAllister and Hofstadter, 1956) – in which the root-mean-squared charge radius of the proton – 0.74±0.24 (fm) – was determined for the first time. The success of lepton scattering was further demonstrated by another Nobel Prize awarded to Friedman, Kendall, and Taylor (Bloom *et al.*, 1969; Breidenbach *et al.*, 1969) for leading the DIS experiments with electron beams at SLAC between 1967 to 1973 – that discovered for the first time the existence of point-like-particles – quarks inside the proton. For details about the discovery of quarks, one may refer to the article written by Michael Riordan (Riordan, 1992).

A. Introduction to Electron-Proton Scattering and Proton Electromagnetic Form Factors

To lowest-order in QED, the dominant contribution to the electron-proton elastic scattering is the one-photon-exchange (OPE) Feynman diagram as shown in Fig. 1. The 4-momentum of the incoming (scattering) electron is labeled by k (k'). The 4-momentum of the target (recoil) proton is labeled by p (p'). A virtual photon exchanged between the electron and the proton carries a 4-momentum, q, and the corresponding momentum transfer squared q^2, is a Lorentz invariant. In electron scattering, the opposite of the four-momentum transfer squared, Q^2 ($Q^2 = -q^2 \geq 0$) is commonly used.

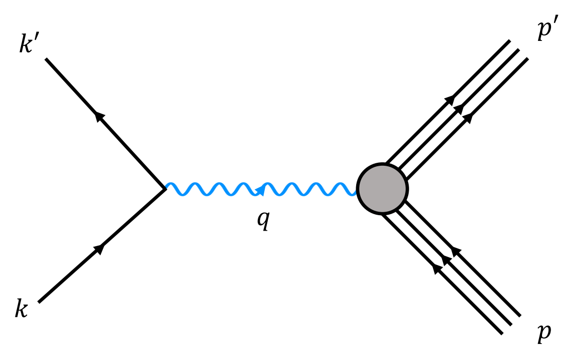

FIG. 1 The one-photon-exchange diagram describing the elastic electron-proton scattering (figure credit: Jingyi Zhou).

The scattering amplitude for the elastic electron scattering from a hadronic target in OPE based on QED can be written, as

$$\mathcal{M} = i\frac{e^2}{Q^2}u(k',h)\gamma_\mu u(k,h)\langle p',\lambda'|J^\mu_{em}(0)|p,\lambda\rangle, \tag{1}$$

in which u denotes the electron Dirac spinors with h the (conserved) helicity of the electrons, λ (λ') denote the helicities of initial (final) hadrons, and $\langle p',\lambda'|J^\mu_{em}(0)|p,\lambda\rangle$ the hadron matrix element of the local electromagnetic current operator (taken at space-time point $x = 0$).

For a spin-$\frac{1}{2}$ extended object such as a nucleon, its electromagnetic transition current – following the requirements of current and parity conservation and covariance under the improper Lorentz group – can be written as

$$\langle p',\lambda'|J^\mu_{em}(0)|p,\lambda\rangle = \bar{N}(p',\lambda')\Gamma^\mu N(p,\lambda), \tag{2}$$

in which N denote the nucleon spinors, and where Γ^μ is the virtual photon-proton vertex:

$$\Gamma^\mu \equiv F_1(q^2)\gamma^\mu + F_2(q^2)\frac{i\sigma^{\mu\nu}q_\nu}{2M}. \tag{3}$$

The functions F_1 and F_2, two independent quantities which depend on $q^2(Q^2)$ only, are called the Dirac and Pauli form factors (FF), respectively, and M is the mass of the nucleon.

The electric (G_E) and the magnetic (G_M) form factor of the nucleon, also called the Sachs' form factors, are two independent linear combinations of F_1 and F_2, originally proposed by Ernst, Sachs and Wali (Ernst and Wali, 1960) as:

$$G_E = F_1 - \frac{Q^2}{4M^2}F_2, \tag{4}$$
$$G_M = F_1 + F_2. \tag{5}$$

In the limit of $Q^2 = 0$, $G_{Ep}(0) = 1$, $G_{En}(0) = 0$, which are just the charge of the proton, and neutron, respectively; while $G_{Mp}(0) = \mu_p$, $G_{Mn}(0) = \mu_n$, the proton and neutron magnetic moments, correspondingly. The Pauli FF at $Q^2 = 0$ is given by the anomalous magnetic moment $F_2(0) \equiv \kappa$, with $\mu_p = 1 + \kappa_p$ and $\mu_n = \kappa_n$. In comparison to the F_1 and F_2 form factors, the G_E and G_M were proposed to have a more intuitive physical interpretation, though $G_E(0) = F_1(0)$. Sachs (Sachs, 1962) showed that in the Breit frame G_E and G_M can be interpreted as Fourier transforms of spatial distributions of charge and magnetization, treating the nucleon as a non-relativistic static system. In the Breit frame the incoming electron has a momentum of $\vec{q}/2$ and the nucleon initial momentum is $-\vec{q}/2$; the scattered electron has a momentum of $-\vec{q}/2$ and the recoil proton has a momentum of $\vec{q}/2$. So it is a special Lorentz frame in which $q^2 = -\vec{q}^{\,2}$, i.e., no energy transfer is involved in this particular reference frame. For each Q^2 value, there is the corresponding Breit frame, in which the form factors are represented as $G_{E,M}(q^2) = G_{E,M}(-\vec{q}^{\,2})$. For non-relativistic (n-rel) static systems, the analogy to a "classical" charge density distribution has then been introduced in the literature through the three-dimensional ($3d$) Fourier transformation of the matrix element of the charge operator in the Breit (B) frame:

$$\begin{aligned}\rho_{3d,n-rel}(r) &= \int \frac{d^3\vec{q}}{(2\pi)^3} e^{-i\vec{q}\cdot\vec{r}} \frac{\langle p', \lambda | J^0_{em}(0) | p, \lambda\rangle_B}{2M}, \\ &= \int \frac{d^3\vec{q}}{(2\pi)^3} e^{-i\vec{q}\cdot\vec{r}} G_E(-\vec{q}^{\,2}),\end{aligned} \tag{6}$$

which only depends on $r = |\vec{r}|$ for a spherical symmetric system.

It has been pointed out in (Lorcé, 2020) that for a relativistic (rel) system, a proper kinematical factor has to be introduced, leading to the modified quantity:

$$\begin{aligned}\rho_{3d,rel}(r) &= \int \frac{d^3\vec{q}}{(2\pi)^3} e^{-i\vec{q}\cdot\vec{r}} \frac{\langle p', \lambda | J^0_{em}(0) | p, \lambda\rangle_B}{2P^0_B}, \\ &= \int \frac{d^3\vec{q}}{(2\pi)^3} e^{-i\vec{q}\cdot\vec{r}} \frac{1}{\sqrt{1 + \vec{q}^{\,2}/(4M^2)}} G_E(-\vec{q}^{\,2}),\end{aligned} \tag{7}$$

where P^0_B is the nucleon energy in the Breit frame. It was furthermore argued in (Lorcé, 2020) from a phase-space perspective that the quantity $\rho_{3d,rel}(r)$ can be interpreted as an internal charge quasi-density of the target. One notices that such relativistic quasi-density is obtained by the Fourier transform of $G_E(q^2)$ multiplied by the relativistic factor $M/P^0_B = 1/\sqrt{1 + Q^2/(4M^2)}$, as $Q^2 \equiv -q^2 = \vec{q}^{\,2}$ in the Breit frame.

To arrive at a strict density or probabilistic interpretation, the momentum transfer is required to remain small compared to the inertia of the system. The concept of a rest-frame density is therefore intrinsically limited by the Compton wavelength of the system. This limitation can however be avoided in the infinite-momentum frame (IMF), in which the magnitude of the nucleon's momentum $|\mathbf{p}| \gg M$, i.e. the nucleon is moving at infinite momentum. The IMF is advantageous in discussing deep inelastic scattering process in which the virtual photon interacts with a parton (quark) inside the nucleon. In the IMF due to relativistic time dilation - the struck quark is essentially free from interacting with other partons inside the nucleon during the short time when the quark interacts with the virtual photon. Rinehimer and Miller (Rinehimer and Miller, 2009) studied the connection between the Breit frame and IMF and showed that when the nucleon matrix element of the time component of the electromagnetic current, which gives $G_E/\sqrt{1 + Q^2/(4M^2)}$ in the Breit frame as discussed above, is boosted to the IMF, one obtains the F_1 form factor, as was also confirmed by the analysis in (Lorcé, 2020) as well as the earlier work of (Chung *et al.*, 1988).

Miller pointed out (Miller, 2019) that the above picture connecting the proton charge density distribution to the Fourier transform of the G_E form factor is not correct, and showed that a three-dimensional charge density, in the strict sense of a probability interpretation, cannot be defined for a nucleon - as a relativistic system of quarks and gluons - because the initial and final state proton wave functions are not the same. Instead, a two-dimensional charge density can be defined, and determined by the Dirac form factor F_1, as a matrix element of a density operator between identical initial and final states which are localized in the plane transverse to the direction of the fast moving nucleons.

Jaffe (Jaffe, 2021) looked at this issue from a fundamental aspect – the interplay between relativity and the uncertainty principle – and pointed out that any attempt to extract spatial distributions of local properties of a hadronic system that is not much larger than its Compton wavelength would fail. In the case of the proton, its Compton wavelength is about 0.2 fm which is not significantly smaller than its size of ∼0.85 fm. Defining the expectation value of the spatial charge density distribution of the proton requires one to localize the proton, which introduces a localization dependence into the relationship between the form factor and the local charge density distribution. Only for systems such as atoms and heavy atomic nuclei – for which the intrinsic sizes of the systems are much larger than the corresponding Compton wavelength – is the connection between the three-dimensional Fourier transform of the charge form factor and the local charge density distribution meaningful. Belitsky *et al.* also discussed the proton form factors and charge distributions in their seminal paper (Belitsky *et al.*, 2004) on the development of the concept of quantum phase-space (Wigner) distributions for quarks and gluons in the proton.

In the last two decades or more, there have been major developments in three-dimensional imaging of the partonic structure of the nucleon – motivated to a large extent by the desire to solve the "proton spin crisis" or "puzzle". These developments also shed new light on the electromagnetic structure of the nucleon. It is important to discuss the proton charge distribution and electric and magnetic form factors in the context of these new developments. In the next section, we briefly introduce the three-dimensional parton distributions first before we discuss the two-dimensional charge density.

B. Three-dimensional parton distributions

The general framework to describe the partonic structure of the proton is through the generalized transverse momentum dependent parton distributions (GTMDs) (Lorcé and Vanderhaeghen, 2011; Meissner and Schlegel, 2009), which are obtained by integrating the fully unintegrated generalized quark-quark correlation functions for a nucleon in momentum space over the light-cone energy component of the quark momentum (Meissner and Schlegel, 2009; Meissner and Goeke, 2008). The thus obtained GTMDs depend on x, $\mathbf{k}_\perp$, and Δ, where x is the longitudinal momentum fraction of the parton, $\mathbf{k}_\perp$, the transverse momentum of the parton, and Δ is the four-momentum transfer to the nucleon. The GTMDs are related to the Wigner distributions (Belitsky *et al.*, 2004; Ji, 2003; Lorcé and Pasquini, 2011) via a Fourier transformation between the transverse momentum transfer $\boldsymbol{\Delta}_\perp$ and the quark's transverse position $\mathbf{b}$. The five-dimensional Wigner distributions $\rho(\mathbf{b}, \mathbf{k}_\perp, x, \vec{S})$ (Lorcé and Yuan, 2012), for a nucleon with polarization $\vec{S}$, are the quantum mechanical analogues of the classical phase-space distributions, with the five dimensions being x, $\mathbf{k}_\perp$, and the transverse coordinates $\mathbf{b}$.

As illustrated in Fig. 2, one can obtain the generalized parton distributions (GPDs) by integrating the GTMDs over the transverse momentum $\mathbf{k}_\perp$. The GPDs can be viewed as the generalization of the parton distribution functions (PDFs) and the form factors. On the other hand, one can obtain the transverse momentum dependent parton distributions (TMDs) by setting the momentum transfer Δ to zero or equivalently by integrating the Wigner distributions over the transverse coordinate $\mathbf{b}$. The TMDs will reduce to PDFs when the transverse momentum is integrated. In Fig. 2, TMFF and TMSD refer to transverse-momentum dependent form factors, and transverse-momentum dependent spin densities, respectively. While the most general one-parton information is contained in the GTMDs, which are connected to the Wigner distributions through Fourier transformations, unfortunately, neither the GTMDs nor the Wigner distributions are measurable in experiments. However, there are ways to access GPDs, which we will briefly discuss next and TMDs experimentally. For TMDs, we refer to a recent review by Anselmino, Mukherjee, and Vossen (Anselmino *et al.*, 2020).

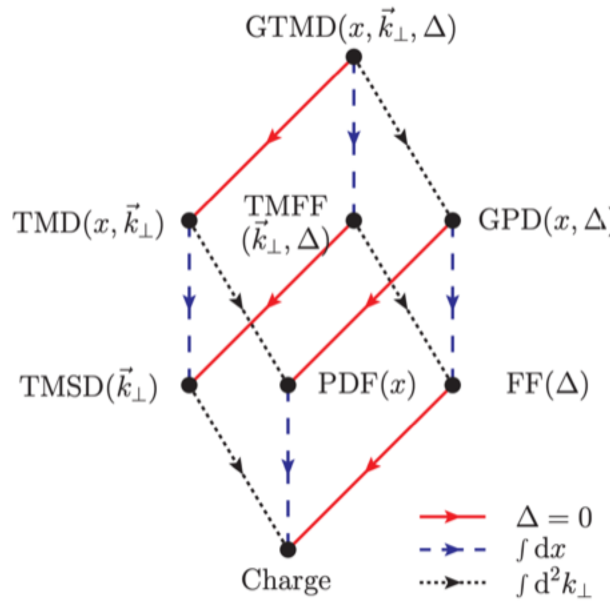

FIG. 2 (Color online) Parton distribution family. The figure is from (Lorcé and Vanderhaeghen, 2011).

In 1997, Deeply Virtual Compton Scattering (DVCS) (Ji, 1997a) was proposed as an experimental tool to probe GPDs. We refer the reader to (Ji, 1997a,b; Müller *et al.*, 1994; Radyushkin, 1996) for the original articles on GPDs and to (Belitsky and Radyushkin, 2005; Boffi and Pasquini, 2007; Diehl, 2003a; Goeke *et al.*, 2001; Guidal *et al.*, 2013; Kumericki *et al.*, 2016) for reviews of the field. In the Björken limit, the DVCS amplitude is described through four off-forward parton distributions (Ji, 1997a): H^q and $\tilde{H}^q$ for a quark of flavor q, which conserve the nucleon helicity, and E^q and $\tilde{E}^q$ that flip the nucleon helicity. These GPDs are functions of x, ξ, and Δ^2 – for example, $H^q(x, \xi, \Delta^2)$, $E^q(x, \xi, \Delta^2)$ – where x is the average fraction of quark longitudinal momentum, ξ is the average fraction of the longitudinal momentum transfer Δ, and Δ^2 is the squared momentum transfer.

In the forward limit, $\Delta^\mu \to 0$, H and $\tilde{H}$ are just the quark momentum, and helicity PDFs:

$$H^q(x, 0, 0) = q(x), \ \tilde{H}^q(x, 0, 0) = \Delta q(x). \tag{8}$$

Furthermore, one can write down the following sum rules relating these new distributions to the quark flavor components of the Dirac and Pauli form factors in a nucleon as:

$$F_1^q(\Delta^2) = \int_{-1}^{+1} dx H^q(x, \xi, \Delta^2), \tag{9}$$

$$F_2^q(\Delta^2) = \int_{-1}^{+1} dx E^q(x, \xi, \Delta^2), \tag{10}$$

where the ξ-independence of these sum rules is a consequence of Lorentz invariance.

C. The nucleon transverse charge densities

We next discuss in more detail how to define a charge density in a nucleon, and how such density is related to the elastic form factors and generalized parton distributions discussed above. For relativistic quantum systems, such as hadrons composed of nearly massless quarks, a proper definition of a charge density requires care as discussed above. For such systems, the number of constituents is not constant as a result of virtual pair production. Consider, as an example, a hadron such as the proton, which is probed by a space-like virtual photon, as shown in Fig. 3. A sizable fraction of the proton's response when probed by a virtual photon with small (or even intermediate) virtuality is coming from wave function components beyond the three valence quark state state (Sufian *et al.*, 2017). In such a system, the wave function contains, besides the three valence quark Fock component $|qqq\rangle$, components where additional $q\bar{q}$ pairs, so-called sea-quarks, or (transverse) gluons g are excited, leading to an infinite tower of $|qqqq\bar{q}\rangle$, $|qqqg\rangle$, ... components. When probing such a system using electron scattering, the exchanged virtual photon will couple to any quark or anti-quark in the proton as shown in Fig. 3 (upper panel). In addition, the virtual photon can also produce a $q\bar{q}$ pair, giving rise e.g. to a transition from a $3q$ state in the initial wave function to a $5q$ state in the final wave function, as shown in Fig. 3 (lower panel). Such processes, leading to non-diagonal overlaps between

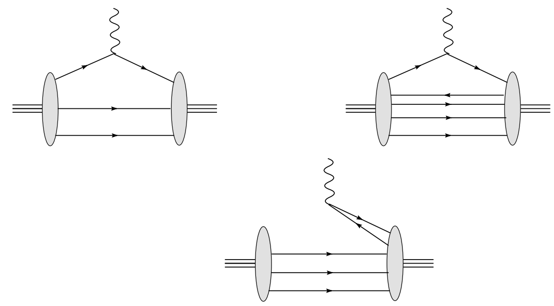

FIG. 3 Coupling of a space-like virtual photon to a relativistic many-body system, as a proton. Upper panel : diagonal transition where the photon couples to a quark, in the leading $3q$ Fock component (left), or in a higher $5q$ Fock component (right). Lower panel : process where the photon creates a $q\bar{q}$ pair leading to a non-diagonal transition between an initial $3q$ state and a final $5q$ state in the proton.

initial and final wave functions, are not positive definite, and do not allow for a simple probability interpretation of the density ρ anymore. Only the processes shown in the upper panel of Fig. 3 with the same initial and final wave function yield a positive definite particle density, allowing for a probability interpretation.

This relativistic dynamical effect of pair creation or annihilation fundamentally hampers the interpretation of density and any discussion of size and shape of a relativistic quantum system. An interpretation in terms of the concept of a density requires suppressing the contributions shown in the lower panel of Fig. 3. This is possible when viewing the hadron from a light-front frame, that allows one to describe the hadron state by an infinite tower of light-front wave functions. Consider the electromagnetic (e.m.) transition from an initial hadron (with four-momentum p) to a final hadron (with four-momentum p') when viewed from a light-front moving towards the hadron. Equivalently, this corresponds with an infinite-momentum frame (IMF) where the hadrons have a large momentum component along the z-axis chosen along the direction of the hadrons average momentum $P = (p + p')/2$. One then defines the light-front plus (+) component by $P^+ \equiv (P^0 + P^3)/\sqrt{2}$, which is always a positive quantity for the quark or anti-quark four-momenta in the hadron. When one views the hadron in a so-called Drell-Yan frame (Drell and Yan, 1970), where the virtual photon four-momentum $\Delta = p' - p$ is purely transverse, satisfying $\Delta^+ = 0$, energy-momentum conservation will forbid processes where this virtual photon splits into a $q\bar{q}$ pair. Such a choice is possible for a space-like virtual photon, and its virtuality is then given by $t \equiv \Delta^2 = -\boldsymbol{\Delta}_\perp^2 < 0$, where $\boldsymbol{\Delta}_\perp$ is the transverse photon momentum, lying in the transverse spatial (x, y)-plane. Here $-t$ or $\boldsymbol{\Delta}_\perp^2$ is the same as the virtuality Q^2 in elastic e-p scattering. In such a frame, the virtual photon only couples to forward moving partons, i.e. only processes such as those shown in the upper panel in Fig. 3 are allowed. We can then define a proper density operator through the + component of the four-current by $J^+ = (J^0 + J^3)/\sqrt{2}$. For one quark flavor q it is given by (Soper, 1977):

$$J_q^+(z^-, \mathbf{b}) = \bar{q}(0, z^-, \mathbf{b})\gamma^+ q(0, z^-, \mathbf{b}) \\ = \sqrt{2} q_+^\dagger(0, z^-, \mathbf{b}) q_+(0, z^-, \mathbf{b}), \qquad (11)$$

where the q_+ fields are related to the quark fields q through a field redefinition, involving the $\pm$ components of the Dirac γ-matrices as $q_+ \equiv (1/2)\gamma^-\gamma^+ q$. In Eq. (11) light-cone coordinates are used with $a^\pm \equiv (a^0 \pm a^3)/\sqrt{2}$, and both quark fields are taken at equal light-cone time $z^+ = 0$. The transverse spatial coordinates are written as two-dimensional vector $\mathbf{b}$. The relativistic density operator J_q^+, defined in Eq. (11), is a positive definite quantity. The electromagnetic charge density operator J_{em}^+ is then obtained by a sum over quarks weighted by their electric charges e_q (in units of e) as :

$$J_{em}^+(z^-, \mathbf{b}) = \sum_q e_q \bar{q}(0, z^-, \mathbf{b})\gamma^+ q(0, z^-, \mathbf{b}). \qquad (12)$$

One can then examine the transverse structure of the nucleon due to the fact that transverse boosts are independent of interactions in the infinite momentum frame (Burkardt, 2006; Kogut and Soper, 1970). Transversely localized nucleon states (Burkardt, 2003; Diehl, 2002, 2003b; Soper, 1977) with its transverse center-of-mass position $\mathbf{R}$ being set to 0, can be defined in terms of linear superposition of states of transverse momentum as (Miller, 2019)

$$|p^+, \mathbf{R} = \mathbf{0}, \lambda\rangle \equiv N \int \frac{d^2\mathbf{p}_\perp}{(2\pi)^2\sqrt{2p^+}} |p^+, \mathbf{p}_\perp, \lambda\rangle, \qquad (13)$$

with $|p^+, \mathbf{R} = \mathbf{0}, \lambda\rangle$ being light-cone helicity (λ) eigenstates (Soper, 1977), and N a normalization factor.

Using the density operator of Eq. (11), one can define transverse densities ρ_λ^q for a quark of flavor q in a transversely localized hadron as (Burkardt, 2000, 2003; Miller, 2007):

$$\rho_\lambda^q(b) \equiv \frac{1}{2P^+} \langle P^+, \mathbf{R} = \mathbf{0}, \lambda | J_q^+(0, \mathbf{b}) | P^+, \mathbf{R} = \mathbf{0}, \lambda\rangle. \qquad (14)$$

Using the translation operator in transverse spatial direction, one can express $J_q^+(0, \mathbf{b}) = e^{-i\hat{\mathbf{P}}_\perp \cdot \mathbf{b}} J_q^+(0) e^{i\hat{\mathbf{P}}_\perp \cdot \mathbf{b}}$, in terms of the local current operator at the origin $J_q^+(0)$. Using Eq. (13) then allows to express the quark transverse density of Eq. (14) as:

$$\rho_\lambda^q(b) \equiv \int \frac{d^2\mathbf{\Delta}_\perp}{(2\pi)^2} e^{-i\,\mathbf{\Delta}_\perp \cdot \mathbf{b}} \frac{1}{2P^+} \\ \times \langle P^+, \frac{\mathbf{\Delta}_\perp}{2}, \lambda \,|\, J_q^+(0) \,|\, P^+, -\frac{\mathbf{\Delta}_\perp}{2}, \lambda\rangle. \qquad (15)$$

In the two-dimensional Fourier transform of Eq. (15), the vector $\mathbf{b}$ denotes the quark position (in the transverse plane) from the transverse center-of-momentum of the hadron. It is the position variable conjugate to the hadron relative transverse momentum $\mathbf{\Delta}_\perp$. The quantity $\rho_\lambda^q(b)$ has the interpretation of the two-dimensional (transverse) density to find a quark of flavor q at distance $b = |\mathbf{b}|$ from the transverse c.m. of the hadron with helicity λ.

For a quark of flavor q in the proton, the matrix element of the J_q^+ operator, entering the two-dimensional Fourier-transform in Eq. (15), can be expressed in terms of the quark flavor contribution F_1^q to the proton Dirac form factor as:

$$\frac{1}{2P^+} \langle P^+, \frac{\mathbf{\Delta}_\perp}{2}, \lambda | J_q^+(0) | P^+, -\frac{\mathbf{\Delta}_\perp}{2}, \lambda\rangle = F_1^q(-\mathbf{\Delta}_\perp^2), \qquad (16)$$

which allows to express the density for a quark of flavor q in the proton, using Eq. (15), as:

$$\rho^q(b) = \int \frac{d^2\mathbf{\Delta}_\perp}{(2\pi)^2} e^{-i\,\mathbf{\Delta}_\perp \cdot \mathbf{b}} F_1^q(-\mathbf{\Delta}_\perp^2), \\ = \int_0^\infty \frac{dQ}{2\pi} Q\, J_0(b\,Q) F_1^q(-Q^2), \qquad (17)$$

where in the last line the circular symmetry of the transverse density was used to convert the two-dimensional Fourier transform to a one-dimensional integral over $Q \equiv |\mathbf{\Delta}_\perp|$, with J_n denoting the cylindrical Bessel function of order n. Furthermore, the helicity subscript λ has been omitted, as for a spin-1/2 system $\rho_{+\frac{1}{2}} = \rho_{-\frac{1}{2}}$.

The two-dimensional electric charge density in a proton is then obtained as sum over the quarks weighted by their electric charges:

$$\rho(b) = \sum_q e_q \rho^q(b). \qquad (18)$$

From the experimentally measured Dirac form factor F_1 of the proton:

$$F_{1p} = \sum_q e_q F_1^q, \qquad (19)$$

one obtains:

$$\rho_p(b) = \int_0^\infty \frac{dQ}{2\pi} Q\, J_0(b\,Q) F_{1p}(-Q^2). \qquad (20)$$

A similar formula holds for the neutron with the interchange $\rho^u \leftrightarrow \rho^d$ in Eq. (18) and $F_1^u \leftrightarrow F_1^d$ in Eq. (19). In this way, it was observed in (Miller, 2007) that the neutron transverse charge density reveals the well known negative contribution at large distances, around 1.5 fm, due to the pion cloud, a positive contribution at intermediate b values, and a negative core at b values smaller than about 0.3 fm. One can understand the negative value of the neutron $\rho(b = 0)$ from Eq. (20) and the observation that over the whole measured Q^2 range the neutron Dirac form factor F_{1n} is negative.

The quark charge densities in Eq. (20) do not fully describe the e.m. structure of the hadron. For a proton, the densities with $\lambda = \pm 1/2$ yield the same information, while a spin-1/2 system is described by two independent electromagnetic form factors. In general, a particle of spin S is described by $(2S+1)$ e.m. moments. To fully describe the structure of a hadron one also needs to consider the charge densities in a transversely polarized hadron state, denoting the transverse polarization direction by $\mathbf{S}_\perp$. The transverse charge densities can be defined through matrix elements of the density operator J_q^+ in eigenstates of transverse spin (Carlson and Vanderhaeghen, 2008, 2009; Lorcé, 2009) as:

$$\rho^q_{T s_\perp}(\mathbf{b}) \equiv \int \frac{d^2\mathbf{\Delta}_\perp}{(2\pi)^2}\, e^{-i\,\mathbf{\Delta}_\perp\cdot\mathbf{b}}\, \frac{1}{2P^+} \times \langle P^+, \frac{\mathbf{\Delta}_\perp}{2}, s_\perp | J_q^+(0) | P^+, \frac{-\mathbf{\Delta}_\perp}{2}, s_\perp\rangle, \quad (21)$$

where $s_\perp$ is the hadron spin projection along the transverse spin direction $\mathbf{S}_\perp \equiv \cos\phi_S \mathbf{e_x} + \sin\phi_S \mathbf{e_y}$, with $\mathbf{e_x}$ and $\mathbf{e_y}$ the two unit-vectors in the transverse plane.

By expressing the transverse spin state in terms of the light-front helicity spinor states as:

$$|s_\perp = +\frac{1}{2}\rangle = \frac{1}{\sqrt{2}}\left\{|\lambda = +\frac{1}{2}\rangle + e^{i\phi_S}\,|\lambda = -\frac{1}{2}\rangle\right\}, \quad (22)$$

the matrix element of the J_q^+ operator, entering the two-dimensional Fourier-transform in Eq. (21), can be expressed in terms of the quark flavor contribution to both the Dirac (F_1^q) and Pauli (F_2^q) form factors as:

$$\frac{1}{2P^+}\langle P^+, \frac{\mathbf{\Delta}_\perp}{2}, s_\perp | J_q^+(0) | P^+, -\frac{\mathbf{\Delta}_\perp}{2}, s_\perp\rangle = F_1^q(-\mathbf{\Delta}_\perp^2) + \frac{i}{2M}\left(\mathbf{S}_\perp \times \mathbf{\Delta}_\perp\right)_z F_2^q(-\mathbf{\Delta}_\perp^2). \quad (23)$$

Taking the weighted sum over the quark charges, the Fourier transform defined by Eq. (21) can then be worked out as (Carlson and Vanderhaeghen, 2008):

$$\rho_{T s_\perp}(\mathbf{b}) = \rho(b) + \sin(\phi_b - \phi_S)\int_0^\infty \frac{dQ}{2\pi}\frac{Q^2}{2M}\, J_1(b\,Q) F_2(-Q^2), \quad (24)$$

where the second term, which describes the deviation from the circular symmetric unpolarized charge density, depends on the quark position $\mathbf{b} = b(\cos\phi_b \mathbf{e_x} + \sin\phi_b \mathbf{e_y})$. Whereas the density ρ_λ for a hadron in a state of definite helicity is circularly symmetric for all spins, the density $\rho_{T s_\perp}$ depends also on the orientation of the position vector $\mathbf{b}$, relative to the transverse spin vector $\mathbf{S}_\perp$, as illustrated in Fig. 4. Therefore, it contains information on the hadron shape, projected on a plane perpendicular to the line-of-sight. It was emphasized recently in (Guo *et al.*, 2021) that in order to define intrinsic quark densities in transverse space, one needs to remove the center-of-mass motion. This amounts to the replacement of F_2 by $F_1 + F_2$ in Eqs. (23) and (24).

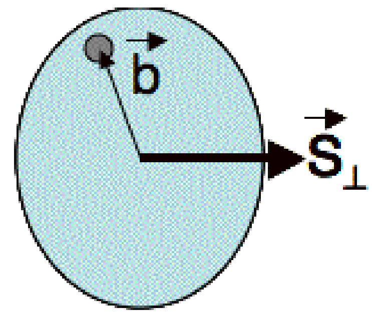

FIG. 4 Schematic view of the projection of the charge density along the line-of-sight (perpendicular to the figure), for a hadron polarized along the direction of $\mathbf{S}_\perp$. The position of the (quark) charge inside the hadron is denoted by $\mathbf{b}$.

As the density ρ_T is not circularly symmetric, one can calculate the dipole moment of its distribution as

$$\mathbf{d} \equiv e\int d^2\mathbf{b}\,\mathbf{b}\,\rho_{T s_\perp}(\mathbf{b}) = -\frac{e}{2M}F_2(0)\left(\mathbf{S}_\perp \times \mathbf{e_z}\right). \quad (25)$$

Eq. (25) implies that polarizing the proton along the x-axis leads to an induced electric dipole moment along the y-axis which is equal to the value of the anomalous magnetic moment, *i.e.* $F_2(0)$ (in units $e/2M$) as first noticed in (Burkardt, 2000). One can understand this induced electric dipole field pattern from special relativity, as the nucleon spin along the x-axis is the source of a magnetic dipole field, denoted by $\vec{B}$. An observer moving towards the nucleon with velocity $\vec{v}$ will see an electric dipole field pattern with $\vec{E}' = -\gamma(\vec{v}\times\vec{B})$ giving rise to the observed effect.

We show the transverse charge densities in a proton and neutron in Fig. 5 based on the recent parameterization of (Ye *et al.*, 2018) for the proton and neutron form factors. One notices that, for the proton, the unpolarized charge density is positive everywhere. For a transversely polarized proton along the x-axis one notices a small displacement of the charge density along the y-axis proportional to the proton's anomalous magnetic moment. For the neutron, the unpolarized density shows the negatively charged core, positive intermediate contribution, and negative pion cloud contribution at large distances, as described above. The corresponding transverse charge density for a neutron polarized along the x-axis gets significantly displaced due to the large (negative) value of the neutron anomalous magnetic moment.

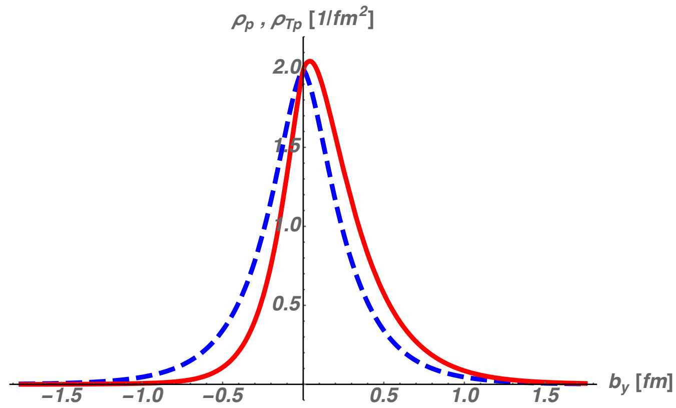

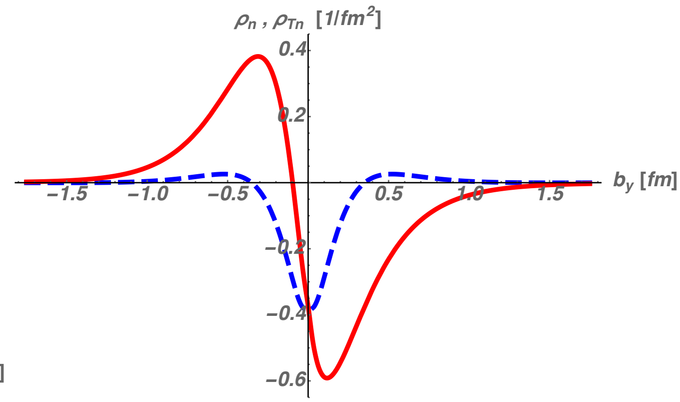

FIG. 5 (Color online) Transverse charge densities for proton (left panel) and neutron (right panel). The curves show the density along the y-axis for an unpolarized nucleon (dashed blue curves), and for a nucleon polarized along the x-axis (solid red curves). For the nucleon form factors, the empirical parameterization of (Ye *et al.*, 2018) was used.

The above discussed light-front densities require us to develop some new intuition, as they are defined at equal light-front time ($z^+ = 0$) of their constituents. When constituents move non-relativistically, it does not make a difference whether they are observed at equal time ($t = 0$) or equal light-front time ($z^+ = 0$), since the constituents can only move a negligibly small distance during the small time interval that a light-ray needs to connect them. This is not the case, however, for bound systems of relativistic constituents such as hadrons (Hoyer, 2009; Jarvinen, 2005). For the latter, the transverse density at equal light-front time can be interpreted as a 2-dimensional flash photograph of a 3-dimensional object (Brodsky *et al.*, 2015), reflecting the position of charged constituents at different times, which are (causally) connected by a light-ray.

D. Radii of quark distributions in a proton

As discussed above, to define and reconstruct a 3-dimensional charge distribution from elastic electron scattering measurements of the form factors of a system requires that one is able to localize the object and fix its center-of-mass, with respect to which one defines the charge distribution (Jaffe, 2021). This is possible for non-relativistic (static) systems for which the typical size is much larger than its Compton wavelength, allowing the probe to localize the charges at distances between both scales. For atomic nuclei, this condition is well satisfied as their Compton wavelength (of order 0.2/A fm) is typically much smaller than their size (of order 1.2 A$^{1/3}$ fm). As an example, for the ^{12}C nucleus, its size of around 2.5 fm is much larger than its Compton wavelength of around 0.02 fm, allowing one to localize charges in between these length scales and reconstruct a charge distribution. For such systems, one can define a 3-dimensional charge distribution as Fourier transform of the measured electric form factor G_E as given in Eq. (6). For such charge distribution, one can define a radius through the normalized moment:

$$\langle r_E^2 \rangle \equiv \frac{\int d^3\vec{r}\, r^2\, \rho_{3\mathrm{d,n-rel}}(r)}{\int d^3\vec{r}\, \rho_{3\mathrm{d,n-rel}}(r)}. \tag{26}$$

Inserting the 3-dimensional density defined in Eq. (6) allows one to express the charge radius as:

$$\langle r_E^2 \rangle = -6 \frac{G_E'(0)}{G_E(0)}, \tag{27}$$

where $G_E'(0) \equiv \frac{dG_E}{dQ^2}\big|_{Q^2=0}$, with $Q^2 = \vec{q}^{\,2}$. One can therefore express the Taylor expansion of G_E at low values of Q^2 as:

$$G_E(-Q^2) \equiv G_E(0) \left\{ 1 - \frac{1}{6} \langle r_E^2 \rangle Q^2 + \mathcal{O}(Q^4) \right\}, \tag{28}$$

and access the charge radius experimentally from the electric form factor slope at the origin.

Applying the above concepts to a nucleon becomes problematic since the nucleon's size (of order 0.85 fm) is not very much larger than its Compton wavelength (of order 0.2 fm), making it impossible to localize the center-of-mass in three spatial dimensions. Besides for light-quark systems, we have discussed that an interpretation in terms of a positive definite quantity is spoiled in the rest frame due to pair creation processes. In the previous section, we reviewed how to properly define density distributions for a nucleon, which is a relativistic bound state. By going to the infinite momentum frame, it allows one to localize the hadron in a plane perpendicular to the direction of a fast moving observer and define density distributions in that plane. For the resulting two-dimensional transverse distributions for a quark of flavor q in the proton, one can then define a mean-squared transverse radius as:

$$\langle b^2 \rangle^q = \frac{\int d^2\mathbf{b}\, \mathbf{b}^2\, \rho^q(b)}{\int d^2\mathbf{b}\, \rho^q(b)} = -4 \frac{F_1'^q(0)}{F_1^q(0)}, \tag{29}$$

where $F_1'^q(0) \equiv \frac{dF_1^q}{dQ^2}\big|_{Q^2=0}$ denotes the slope at the origin of the corresponding Dirac form factor. Note that the radius definition of Eq. (29) for each quark flavor is properly normalized to the number of valence quarks in the proton: $F_1^u(0) = 2$ and $F_1^d(0) = 1$, yielding:

$$\langle b^2 \rangle^u = -2F_1'^u(0), \qquad \langle b^2 \rangle^d = -4F_1'^d(0). \tag{30}$$

To determine the mean-squared transverse radii Eq. (30) for each quark flavor, we start by expressing the proton and neutron Dirac form factors, using isospin symmetry, as:

$$\begin{aligned} F_{1p} &= e_u F_1^u + e_d F_1^d, \\ F_{1n} &= e_u F_1^d + e_d F_1^u, \end{aligned} \tag{31}$$

which allows one to extract the Dirac form factors for the u- and d-quark flavors. These enter the corresponding transverse quark densities, as:

$$F_1^u = 2F_{1p} + F_{1n}, \qquad F_1^d = 2F_{1n} + F_{1p}. \tag{32}$$

Combining Eqs. (30) and (31), this allows one to express the proper mean-squared transverse radii for the u- and d-quark distributions in a proton as:

$$\begin{aligned} \langle b^2 \rangle^u &= -2\left\{2F_{1p}'(0) + F_{1n}'(0)\right\}, \\ \langle b^2 \rangle^d &= -4\left\{F_{1p}'(0) + 2F_{1n}'(0)\right\}. \end{aligned} \tag{33}$$

The last equation allows one to express the difference of the mean-squared radii for d- and u-quark distributions in a proton as:

$$\langle b^2 \rangle^d - \langle b^2 \rangle^u = -6F_{1n}'(0). \tag{34}$$

In order to empirically determine the mean-squared transverse radii of u- and d-quark distributions in a proton, we relate the derivative of the Dirac form factors to the conventional Sachs form factors G_E and G_M, defined through Eqs. (4, 5), which yields:

$$F_1'(0) = G_E'(0) + \frac{\kappa}{4M^2}. \tag{35}$$

Following the convention for non-relativistic (static) systems, one can Taylor expand the proton and neutron Dirac form factors at low momentum transfer Q^2 as:

$$G_{Ep}(-Q^2) \equiv 1 - \frac{1}{6}\langle r_{Ep}^2 \rangle Q^2 + \mathcal{O}(Q^4), \tag{36}$$

$$G_{En}(-Q^2) \equiv -\frac{1}{6}\langle r_{En}^2 \rangle Q^2 + \mathcal{O}(Q^4). \tag{37}$$

We like to emphasize again that for relativistic bound states, such as a nucleon, where the concept of a 3-dimensional charge distribution is not well defined, Eqs. (36,37) are merely used as operational definitions for the form factor slopes at the origin, even though we will refer to these quantities for simplicity as "radii" in the remainder of this review. Eqs. (36,37) then allow one to express for the nucleon ($N = p, n$):

$$-6F_{1N}'(0) = \langle r_{EN}^2 \rangle - \frac{3\kappa_N}{2M^2}, \tag{38}$$

where the anomalous magnetic moment contribution is known as the Foldy term.

The radius of the transverse charge distribution in a proton is then obtained as sum over the radii for the quark distributions weighted by their charges:

$$\langle b^2 \rangle_p = \frac{4}{3}\langle b^2 \rangle^u - \frac{1}{3}\langle b^2 \rangle^d = -4F_{1p}'(0). \tag{39}$$

For the neutron, assuming isospin symmetry, we define a transverse charge radius as[1]:

$$\langle b^2 \rangle_n = \frac{2}{3}\langle b^2 \rangle^d - \frac{2}{3}\langle b^2 \rangle^u = -4F_{1n}'(0). \tag{40}$$

In Table I, we show the empirical values of proton and neutron radii $\langle r_E^2 \rangle$, the Foldy terms, the extracted Dirac slopes $F_1'(0)$, and transverse charge radii $\langle b^2 \rangle$. For the proton values for $\langle r_{Ep}^2 \rangle$ we are showing both the recent analysis of (Cui *et al.*, 2021) based on e-p scattering results, which will be discussed in Section V, Eq. (73), and the extracted value from the μH Lamb shift measurements, which will be discussed in Section VI, Eq. (76). Anticipating the discussion in Section VI, the quantity entering the hydrogen spectroscopy Lamb shift experiments is also given by the slope $G_{Ep}'(0)$. Therefore, it is important and meaningful to compare the proton charge radius values obtained by these two experimental techniques. We see from Table I that the extracted mean-squared transverse radii $\langle b^2 \rangle$ are consistent between both analyses, showing that the transverse charge distribution in a proton has a rms radius around 0.63 fm, as seen by an observer moving with a light-front. For the neutron, one notices that its Dirac slope value $F_{1n}'(0)$ is the result of a large cancellation between the $\langle r_{En}^2 \rangle$ term and the Foldy term, which have opposite signs, resulting in a value of $F_{1n}'(0)$ around 10% of the size of each contribution. As the Foldy term for the neutron is slightly larger in absolute value than the $\langle r_{En}^2 \rangle$ term, the positive value of $-6F_{1n}'(0)$ results from Eq. (34) in a slightly larger mean-squared radius for the d-quarks in a proton in comparison with the u-quarks in the proton, confirming the observation of (Cates *et al.*, 2011) based on a flavor decomposition of proton and neutron form factors.

[1] Note that for a neutron, this follows the convention in defining a charge radius for a neutral system, as one cannot use the definition of Eq. (29) which is normalized to the total charge.

	$\langle r_E^2 \rangle$ (fm^2)	$-\frac{3\kappa_N}{2M^2}$ (fm^2)	$-6F_1'(0)$ (fm^2)	$\langle b^2 \rangle$ (fm^2)
proton (e-p)	0.717 ± 0.014 (Cui *et al.*, 2021)	-0.1189	0.598 ± 0.014	0.399 ± 0.009
proton (μH)	0.7071 ± 0.0007 (Antognini *et al.*, 2013a)		0.5882 ± 0.0007	0.3921 ± 0.0005
neutron (PDG)	-0.1161 ± 0.0022 (Zyla *et al.*, 2020)	0.1266	0.0105 ± 0.0022	0.0070 ± 0.0015

TABLE I Empirical values of the proton and neutron radii $\langle r_E^2 \rangle$, Foldy terms, Dirac slopes $F_1'(0)$, and transverse charge radii $\langle b^2 \rangle$. For the proton, we show the values both using the e-p scattering data analysis of (Cui *et al.*, 2021), and the values from μH Lamb shift measurements (Antognini *et al.*, 2013a).

	$\langle b^2 \rangle^u$ (fm^2)	$\langle b^2 \rangle^d$ (fm^2)
proton (e-p)	0.402 ± 0.009	0.413 ± 0.010
proton (μH)	0.396 ± 0.001	0.406 ± 0.003

TABLE II Extracted values of the mean-squared transverse radii for u- and d-quark distributions in the proton, using the neutron PDG value for $\langle r_{En}^2 \rangle$ given in Table I, and for the proton values for $\langle r_{Ep}^2 \rangle$ from both the analysis of (Cui *et al.*, 2021) based on e-p scattering results, as well as the extracted value from the μH Lamb shift measurements (Antognini *et al.*, 2013a).

In Table II, we show the extracted values of the mean-squared transverse radii for u- and d-quark distributions in the proton, using the neutron PDG value for $\langle r_{En}^2 \rangle$, and both analyses for the proton as shown in Table I. For the more accurate values extracted from the μH Lamb shift measurements, one obtains a precision of 0.3% (0.7%) on the mean-squared transverse radii for the u (d)-quark distributions. Using the values in Table I, we notice that the neutron $F_{1n}'(0)$ term contributes 1% (4%) to the mean-squared radii for the u (d)-quark distributions respectively in Eq. (33). One also notices that the uncertainty on the neutron $F_{1n}'(0)$ value is at present the limiting uncertainty in the extraction of the mean-squared transverse radius value for the d-quark distribution.

In the next sections, we will discuss unpolarized and polarized electron-proton elastic scatterings and the methods to extract the proton electric form factor and the proton charge radius value based on the definition of Eq. (36) as slope of the form factor G_E at the origin. Likewise, one can also define a magnetic radius as slope at the origin of the form factor G_{MN} for the nucleon ($N = p, n$):

$$G_{MN}(-Q^2) \equiv \mu_N \left\{ 1 - \frac{1}{6} \langle r_{MN}^2 \rangle Q^2 + \mathcal{O}(Q^4) \right\}, \quad (41)$$

where μ_N is the nucleon magnetic moment, $\mu_p = 2.79$ and $\mu_n = -1.91$, in the units of the nucleon magneton.

Ideally, to extract the proton charge radius value, one needs to extract the proton electric form factor, G_E all the way down to $Q^2 = 0$, and then determine its slope. In practice, it is not possible to measure G_E at $Q^2 \sim 0$, which corresponds to near 0° scatterings. Therefore some type of extrapolation is unavoidable which may introduce systematic uncertainties associated with the determination of $\langle r_{Ep}^2 \rangle^{1/2}$ as discussed below.

A theoretical determination of the proton radius starting from QCD requires a nonperturbative framework. The only ab-initio tool so far is lattice QCD. The standard procedure in lattice QCD is to compute the electric form factor for finite values of the momentum transfer and then perform a fit to determine the slope at zero momentum transfer, e.g. through a popular dipole fit or a z-expansion fit. However, on a finite lattice, the smallest nonzero momentum is $2\pi/L$ with L is the spatial size of the lattice. Therefore, reaching very small momentum transfers is challenging as it requires very large lattices. Furthermore, although electromagnetic form factors have been studied within lattice QCD for many years, it is only recently that they have been extracted using simulations with physical values of the light quark masses.

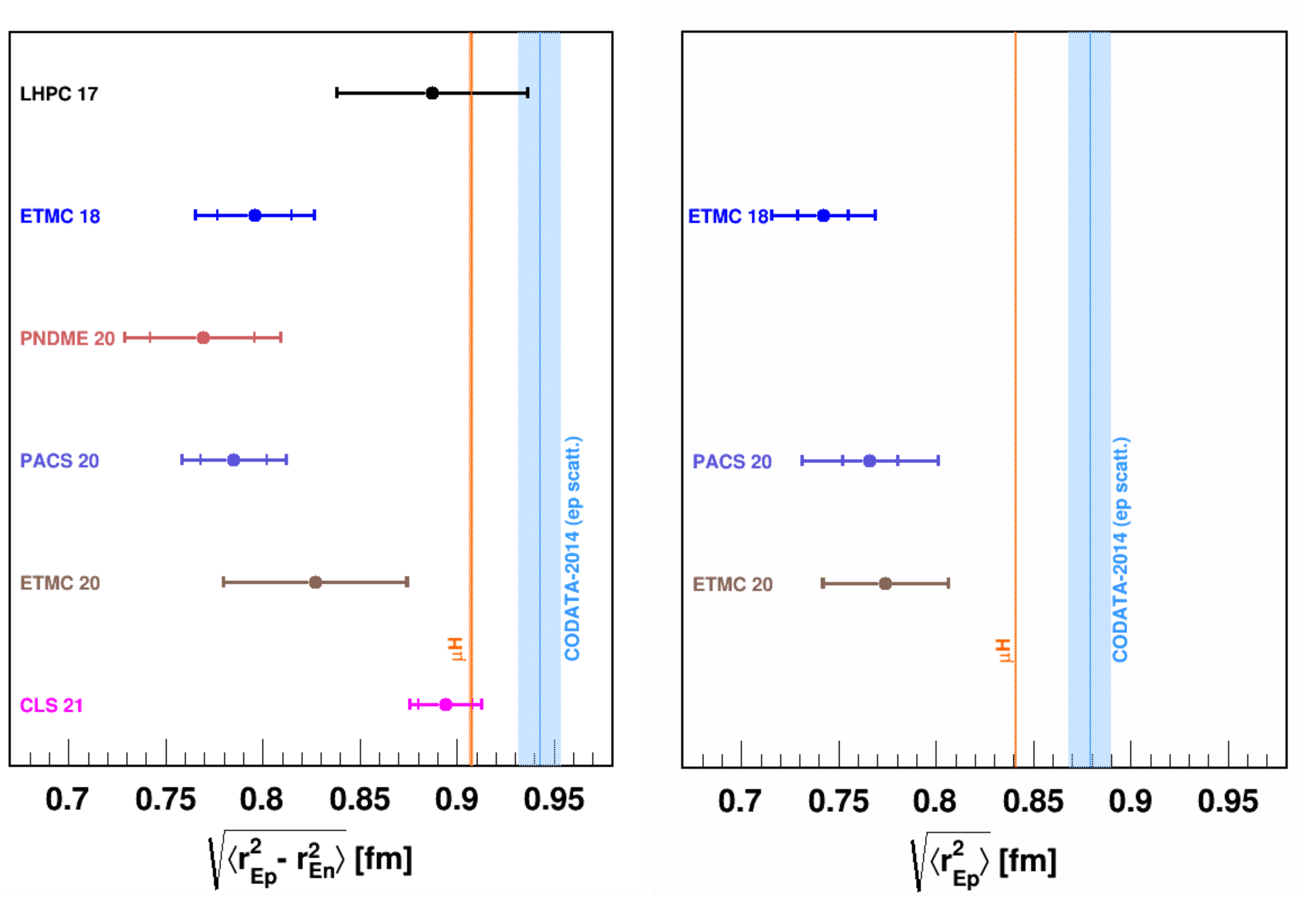

FIG. 6 (Color online) Compilation of recent lattice QCD results for the isovector charge radius (left panel) and the proton charge radius (right panel), obtained from ensembles at the physical pion mass. Results shown are from LHPC (Hasan *et al.*, 2018); ETMC, both using a form factor fit ETMC 18 (Alexandrou *et al.*, 2019), as well as the direct calculation of the radius ETMC 20, avoiding an extrapolation through a form factor fit (Alexandrou *et al.*, 2020); PNDME (Jang *et al.*, 2020); PACS (Shintani *et al.*, 2019); CLS (Djukanovic *et al.*, 2021). Inner error bars display the statistical errors, whereas outer error bars display the full error. The vertical bands show the empirical result extracted from muonic hydrogen spectroscopy and the CODATA-2014 recommended value, as discussed in Sections V and VI (figure credit: Jingyi Zhou).

In Fig. 6, we show a compilation of recent lattice QCD results for both the isovector charge radius $(\langle r^2_{Ep}\rangle - \langle r^2_{En}\rangle)^{1/2}$, as well as the proton charge radius, obtained from ensembles at or near the physical pion mass. For the isovector radius, only the connected quark diagrams, in which the photon couples to the quarks connected to either the intial or final nucleon, contribute. The proton charge radius also requires the much harder calculation of the contribution from disconnected diagrams, in which the photon couples to a $q\bar{q}$ loop, which interacts with the quarks in the intial and final proton through gluon exchanges. Although the disconnected contribution to the proton electric form factor at low momentum transfer is found to be in the 1 % range (Alexandrou *et al.*, 2019), its omission would result in an uncontrolled systematic error. Such systematics need to be under control for precision comparisons of the proton charge radius at the 1% level or better.

Improving on the precision of the lattice extractions of the proton charge radius also requires reducing the model error induced by a form factor fit, which is done in most of the lattice results so far. To this end, a first step was taken in the lattice study of (Alexandrou *et al.*, 2020), which has explored a direct method to extract the proton radius that does not depend on fitting the form factor, displayed by ETMC 20 in Fig. 6.

The lattice calculations have made important progress in recent years by controlling excited state contamination and by performing calculations at the physical point. One notices however from Fig. 6 that further improvements are called for to reach the precision level obtained in the empirical extractions.

E. The extraction of proton electromagnetic form factors

The differential cross-section based on OPE for elastic electron-nucleon scattering can be written as:

$$\frac{d\sigma}{d\Omega}_{lab} = \frac{\alpha^2}{4E^2 \sin^4 \frac{\theta}{2}} \frac{E'}{E} \times \left\{ \frac{G_E^2 + \tau G_M^2}{1+\tau} \cos^2 \frac{\theta}{2} + 2\tau G_M^2 \sin^2 \frac{\theta}{2} \right\}, \quad (42)$$

where E is the incident electron energy; E' the energy of the scattered electron, and θ the electron scattering angle, α is the fine structure constant, $\tau \equiv \frac{Q^2}{4M^2}$, and where the mass of the electron is neglected.

To separately determine the proton electric and magnetic form factor for each Q^2 value, ideally one would need to perform two measurements with independent combinations of the G_E and G_M at the corresponding Q^2 value, with one of the measurements involving polarizations which we will discuss further on. However, polarization experiments only became possible in recent decades. Historically, the Rosenbluth technique (Rosenbluth, 1950) had been used extensively which allows for the separation of these two form factors by performing unpolarized differential cross section measurements only. To see how this works, one can rewrite Eq. (42) as:

$$\frac{d\sigma}{d\Omega}_{lab} = \sigma_M \frac{1}{1+\tau} \left\{ G_E^2 + \frac{\tau}{\epsilon} G_M^2 \right\}, \quad (43)$$

where $\epsilon = \left(1 + 2(1+\tau)\tan^2 \frac{\theta}{2}\right)^{-1}$ is the virtual photon longitudinal polarization, and σ_M is the Mott cross section describing the scattering from a pointlike spinless target (where we included the recoil factor E'/E):

$$\sigma_M = \frac{\alpha^2 \cos^2 \frac{\theta}{2}}{4E^2 \sin^4 \frac{\theta}{2}} \left(\frac{E'}{E} \right). \quad (44)$$

At a fixed Q^2 value, one can take a series of measurements by varying the incident electron beam energy and the scattering angle. According to Eq. (43), one can then fit the measured reduced cross section $G_M^2 + \epsilon/\tau G_E^2$ as a function of ϵ. Then from the slope and the intercept of the fit, one can determine G_E^2 and G_M^2. There are limitations to the Rosenbluth method: at low Q^2, due to the kinematic suppression, the extraction of the proton magnetic form factor is problematic while at high Q^2, the magnetic contribution dominates the cross section and the extraction of the proton G_E becomes difficult.

To overcome the aforementioned limitations associated with the Rosenbluth technique, an independent combination of the proton electric and magnetic form factors can be obtained by a double polarization measurement from electron-proton elastic scattering in addition to unpolarized differential cross section measurements, thereby separating these two form factors. Double polarization measurements in the context of electron-proton scattering refer to the following two cases: (i) longitudinally polarized electrons scattering from a polarized proton target; (ii) longitudinally polarized electrons scattering from an unpolarized proton target with the recoil proton polarization measured by a polarimeter. In this paper, we will not review the technical aspects of polarized electron beams, polarized proton targets, nor the recoil proton polarimeters. We refer interested readers to review articles (Gao, 2003; Perdrisat *et al.*, 2007) instead.

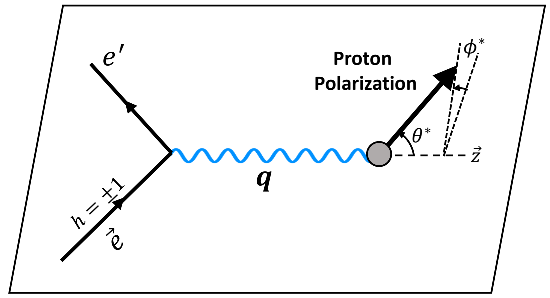

FIG. 7 (Color online) The one-photon-exchange diagram for spin-dependent electron-proton scattering (figure credit: Jingyi Zhou).

The one-photon-exchange diagram for spin-dependent electron-nucleon scattering is shown in Fig. 7. In this picture the incident electron is longitudinally polarized with helicity of $h = \pm 1$, corresponding to an electron's spin being parallel or anti-parallel to its momentum direction, respectively. The target proton spin vector is shown by a thick arrow, with θ^* and ϕ^* as its polar and azimuthal angles defined with respect to the three-momentum transfer vector $\mathbf{q}$ of the virtual photon. The scattering plane is defined as the x, z plane with $\hat{z} = \mathbf{q}/|\mathbf{q}|$ and $\hat{y} = (\mathbf{k} \times \mathbf{k}')/(|\mathbf{k}||\mathbf{k}'|)$, with $\mathbf{k}$ and $\mathbf{k}'$ being the incident and scattered electron three-momentum vector, respectively. The spin-dependent asymmetry A is defined as $A = (\sigma^{h+} - \sigma^{h-})/(\sigma^{h+} + \sigma^{h-})$, where $\sigma^{h^\pm}$ denotes the differential cross sections for the two different helicities of the polarized electron beam.

For longitudinally polarized electrons scattering from a polarized proton target, the differential cross section can be written (Donnelly and Raskin, 1986) as:

$$\frac{d\sigma}{d\Omega} = \Sigma + h\Delta, \quad (45)$$

where Σ is the unpolarized differential cross section given by Eq. (42), and Δ is the spin-dependent differential cross section given by:

$$\Delta = \sigma_{Mott}[v_z \cos\theta^* G_M^2 + v_x \sin\theta^* \cos\phi^* G_M G_E], \quad (46)$$

where

$$v_z = -2\tau \tan\frac{\theta}{2}\sqrt{\frac{1}{1+\tau}+\tan^2\frac{\theta}{2}}, \quad (47)$$

$$v_x = -2\tan\frac{\theta}{2}\sqrt{\frac{\tau}{1+\tau}}, \quad (48)$$

are kinematic factors. The spin-dependent asymmetry A is defined in terms of the polarized and unpolarized cross-sections as:

$$A = \frac{\Delta}{\Sigma} = \frac{v_z \cos\theta^* G_M^2 + v_x \sin\theta^* \cos\phi^* G_M G_E}{(\epsilon G_E^2 + \tau G_M^2)/[\epsilon(1+\tau)]}\ . \quad (49)$$

The experimental asymmetry A_{exp} is related to the spin-dependent asymmetry of Eq. (49) by the relation

$$A_{exp} = P_b P_t A\ , \quad (50)$$

where P_b and P_t are the beam and target polarization, respectively. A determination of the ratio G_E/G_M, independent of the knowledge of the beam and target polarization can be precisely obtained by measuring the so-called super ratio

$$R = \frac{A_1}{A_2} = \frac{v_z \cos\theta_1^* G_M^2 + v_x \sin\theta_1^* \cos\phi_1^* G_M G_E}{v_z \cos\theta_2^* G_M^2 + v_x \sin\theta_2^* \cos\phi_2^* G_M G_E}\ , \quad (51)$$

where A_1 and A_2 are elastic electron-proton scattering asymmetries measured at an identical value of Q^2 simultaneously, but at two different proton spin orientations relative to $\mathbf{q}$, corresponding to (θ_1^*, ϕ_1^*) and (θ_2^*, ϕ_2^*), respectively. However, the proton spin direction is fixed in the laboratory frame, therefore it is feasible if one has a symmetric detection system. For a symmetric detector configuration with respect to the incident electron momentum direction, the A_1 and A_2 can be measured simultaneously by forming two independent asymmetries with respect to either the electron beam helicity or the target spin orientation in the beam-left and beam-right sector of the detector system, respectively. Thus, the proton form factor ratio can be determined with high systematic accuracy using this technique because it is insensitive to the uncertainties in determining the beam and the target polarizations. Such a technique was pioneered (Crawford *et al.*, 2007) in the BLAST experiment (Hasell *et al.*, 2011) at the former MIT-Bates linear accelerator center, where the proton electric to magnetic form factor ratio was extracted in the Q^2 range from 0.15 to 0.65 (GeV/c)^2.

In polarization transfer measurements – the polarization from the incident electron beam is transferred to the recoil protons – and the recoil proton polarization is measured using a recoil proton polarimeter as illustrated in Fig. 8. Such a polarimeter relies on secondary scatterings – recoil protons from e-p scattering off an analyzer such as CH_2 – and spin-orbital interaction of protons and nuclei, and spin-dependent proton-proton interaction which give rise to azimuthal angular dependence in

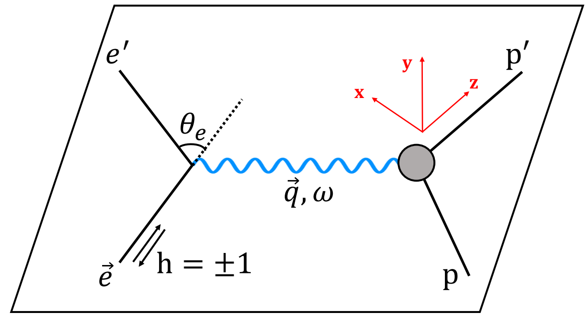

FIG. 8 (Color online) The one-photon-exchange diagram for polarization transfer from longitudinally polarized electron to unpolarized proton (figure credit: Jingyi Zhou).

the distribution of the scattered protons. By analyzing such azimuthal angular dependence, one can determine the recoil proton polarization components in the reaction plane ($x - z$ plane in Fig. 8). Such secondary scatterings take place at the focal plane of the spectrometer and the polarimeter is also called focal-plane polarimeter (FPP). In order to determine the proton electric to magnetic form factor ratio at the target from the proton polarization components measured at the focal plane, an involved spin transport process is needed because the proton spin rotates as it goes through various magnetic components inside a magnetic spectrometer. The proton polarization measured by FPP, $\vec{P}_{\text{fpp}}$, and the proton polarization at the target, $\vec{P}$, are related through a 3-dimensional spin rotation matrix. The elements of the spin rotation matrix can be calculated from a detailed modeling of the magnetic spectrometer including all spectrometer magnets (dipole, quadrupoles), fringe fields, and dipole field gradient, etc. For details about such polarimeters, we refer interested readers to the review article by Perdrisat, Punjabi, and Vanderhaeghen (Perdrisat *et al.*, 2007).

In the one-photon exchange Born approximation, the scattering of longitudinally polarized electrons results in a transfer of polarization to the recoil proton with only two nonzero components, P_x perpendicular to, and P_z parallel to the proton momentum in the scattering plane as illustrated in Fig. 8 (Arnold, 1981). The form factor ratio can be determined from a simultaneous measurement of the two recoil polarization components in the scattering plane as

$$\frac{G_E}{G_M} = -\frac{P_x}{P_z}\frac{E+E'}{2M}\tan(\theta/2), \quad (52)$$

in terms of the incident and scattered electron energies E and E' respectively, and electron scattering angle θ. The polarization transfer measurement was carried out by Zhan *et al.* (Zhan *et al.*, 2011) and a proton charge radius value was extracted combining unpolarized electron-proton scattering data (see Section VB).

F. Two-Photon-Exchange Contribution to Electron-Proton Scattering

Note so far all our discussions are based on the dominant one-photon-exchange (OPE) Born diagram contribution in electron-proton scattering as higher orders contributions are suppressed due to the smallness of the fine-structure constant, $\alpha \simeq 1/137$. The next-to-leading-order contribution is the two-photon-exchange (TPE) contribution, as shown in Fig. 9, which is proportional to the doubly-virtual Compton subprocess on the proton side.

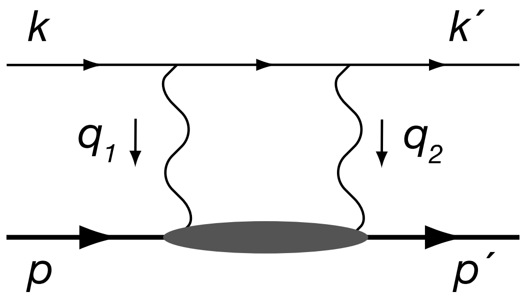

FIG. 9 The two-photon-exchange diagram for elastic electron-proton scattering. The blob denotes the doubly-virtual Compton subprocess on the proton.

The TPE contribution became a strong interest after a drastic difference was reported on the proton G_E/G_M ratio measured directly using a recoil proton polarimeter (Jones *et al.*, 2000) from those using Rosenbluth separation. The data from (Jones *et al.*, 2000) and the subsequent recoil polarization experiments (Gayou *et al.*, 2002; Puckett *et al.*, 2010; Punjabi *et al.*, 2005) show very intriguing behavior at higher Q^2, i.e., G_{Ep} falls off much faster than G_{Mp} as a function of Q^2, while the two form factors extracted from unpolarized differential cross section measurements using the Rosenbluth separation method show a similar Q^2 dependence. The near constant behavior of the proton G_{Ep}/G_{Mp} ratio extracted from unpolarized measurements was confirmed, and extended to a higher Q^2 value near 5.5 (GeV/c)^2 by another experiment at Jefferson Lab (Christy *et al.*, 2004). The first explanations of such puzzling behavior pointed towards hard TPE processes between the electron and the proton, which become relevant once experiments aim to access terms which contribute at or below the percent level to the scattering cross section as is the case in the Rosenbluth method at larger Q^2 values (Blunden *et al.*, 2003; Guichon and Vanderhaeghen, 2003). This unexpected behavior triggered intensive experimental and theoretical studies of the TPE effect in electron-proton scattering in the last two decades as its effect is expected to be different in unpolarized cross section measurements compared to recoil polarization experiments; see (Arrington *et al.*, 2011; Carlson and Vanderhaeghen, 2007) for some early reviews of this field.

To account for two- and multi-photon exchange effects in a model independent way requires one to generalize the amplitude of Eq. (1) describing the elastic e-p scattering. Neglecting the electron mass, the elastic e-p scattering amplitude, following the notations introduced in Section III.A, can be expressed through three independent structures (Guichon and Vanderhaeghen, 2003) :

$$\begin{aligned}\mathcal{M}_{h,\,\lambda'\lambda} \,&=\, i(e^2/Q^2)\,\bar{u}(k',h)\gamma_\mu u(k,h)\\ &\times \bar{N}(p',\lambda')\left(\tilde{G}_M\,\gamma^\mu - \tilde{F}_2\frac{P^\mu}{M} + \tilde{F}_3\frac{\gamma\cdot K P^\mu}{M^2}\right)N(p,\lambda),\end{aligned} \tag{53}$$

in which $K \equiv (k+k')/2$, and where the functions $\tilde{G}_M$, $\tilde{F}_2$, and $\tilde{F}_3$ are complex functions of ϵ and Q^2. In the OPE approximation, the functions $\tilde{G}_M$ and $\tilde{F}_2$ reduce to the Q^2 dependent form factors G_M and F_2 respectively, while the function $\tilde{F}_3$ vanishes. When accounting for the (very small) electron helicity flip effects, which are proportional to its mass, it was shown in (Gorchtein *et al.*, 2004) that three more amplitudes are needed to fully describe the e-p scattering amplitude. Based on such general analysis, the TPE corrections to both unpolarized and polarization observables have been expressed in (Guichon and Vanderhaeghen, 2003) in terms of the amplitudes $\tilde{G}_M$, $\tilde{F}_2$, and $\tilde{F}_3$. In that work it was shown that by adding a TPE contribution of the size expected from perturbation theory, it is possible to simultaneously account for the relatively large correction to the unpolarized observable when extracting the G_{Ep}/G_{Mp} ratio at larger Q^2, while maintaining a small correction in the polarization observables.

To use electron scattering as a precision tool, it is clearly indispensable to arrive at a better quantitative understanding of TPE processes, and a lot of activities have taken place over the past two decades or are planned in the near future. Firstly, there exists observables which provide us with very clear indications of the size of TPE effects, as they would be exactly zero in the absence of two- or multiphoton-exchange contributions. Such observables are normal single-spin asymmetries (SSA) of electron-nucleon scattering, where either the electron spin or the nucleon spin is polarized normal to the scattering plane. Because such SSAs are proportional to the imaginary part of a product of two amplitudes, they are zero for real (nonabsorptive) processes such as OPE. At leading order in the fine-structure constant, they result from the product of the OPE amplitude and the imaginary part of the TPE amplitude. For the target normal SSA, they were predicted to be in the (sub) percent range some time ago (De Rujula *et al.*, 1971). A measurement of the normal SSA for the elastic electron-^{3}He scattering, by the JLab Hall A Coll., has extracted a SSA for the elastic electron-neutron subprocess in the percent range (Zhang *et al.*, 2015). For the experiments with polarized beams, the corresponding normal SSAs were predicted to be in the range of a few to hundred ppm for electron beam energies in the GeV range (Afanasev *et al.*, 2002; Gorchtein *et al.*, 2004; Pasquini and Vanderhaeghen, 2004). Although such beam normal spin asymmetries are small, being proportional to the electron mass, the parity-violation programs at the major electron laboratories have reached precisions on asymmetries with longitudinal polarized electron beams well below the ppm level, and the next generations of such experiments are designed to reach precisions at the sub-ppb level (Kumar *et al.*, 2013). The beam normal SSA, which is due to TPE and thus parity conserving, has been measured over the past two decades as a spinoff in the parity-violating electron scattering programs at MIT-BATES (SAMPLE Coll.) (Wells *et al.*, 2001), at MAMI (A4 Coll.) (Balaguer Rios, 2012; Gou *et al.*, 2020; Maas *et al.*, 2005), and at JLab (G0 Coll. (Androic *et al.*, 2011; Armstrong *et al.*, 2007), HAPPEX/PREX Coll. (Abrahamyan *et al.*, 2012), and Qweak Coll. (Androić *et al.*, 2020)). The resulting beam normal SSA range from a few ppm in the forward angular range to around a hundred ppm in the backward angular range, in qualitative agreement with theoretical TPE expectations.

While the nonzero normal SSAs in elastic electron-nucleon scattering quantify the imaginary parts of the TPE amplitudes, measurements of their real parts have also been performed by several dedicated experiments over the past few years. In particular, the deviation from unity of the elastic scattering cross-section ratio $R_{2\gamma} \equiv e^+p/e^-p$ is proportional to the real part of the product of OPE and TPE amplitudes. Recent measurements of $R_{2\gamma}$, for Q^2 up to 2 GeV^2, have been performed at VEPP-3 (Rachek *et al.*, 2015), by the CLAS Coll. at JLab (Adikaram *et al.*, 2015; Rimal *et al.*, 2017), and by the OLYMPUS Coll. at DESY (Henderson *et al.*, 2017). These experiments show that $R_{2\gamma}$ ranges, for the kinematic region corresponding with $Q^2 = 0.5 - 1$ GeV^2 and virtual photon polarization parameter $\epsilon = 0.8 - 0.9$, from a value $R_{2\gamma} \approx 0.99$ (Henderson *et al.*, 2017), showing a deviation from unity within $2-3\,\sigma$ (statistical and uncorrelated systematic errors), to a value $R_{2\gamma} = 1.02 - 1.03$ for $Q^2 \approx 1.5$ GeV^2 and $\epsilon \approx 0.45$ (Rachek *et al.*, 2015; Rimal *et al.*, 2017). Furthermore, the GEp2gamma Coll. at JLab (Meziane *et al.*, 2011) has performed a pioneering measurement of the deviation from the OPE prediction for both double-polarization components P_x and P_z of the $\vec{e}p \to e\vec{p}$ process at $Q^2 = 2.5$ GeV^2. While for P_x the TPE corrections were found to be negligible, for P_z it has found a deviation from the OPE result at the 4σ level at $\epsilon = 0.8$ (Meziane *et al.*, 2011). In combination with the unpolarized data, these measurements of the ϵ dependence of both double-polarization observables in the $\vec{e}p \to e\vec{p}$ process at a fixed value of Q^2 have been used in (Guttmann *et al.*, 2011) to provide a first disentanglement of the three TPE amplitudes describing elastic e-p scattering for massless electrons, as given by Eq. (53).

While the TPE effects have been shown by experiments to be of the size needed to bring the form factor ratio results from unpolarized measurements closer to those from the recoil polarization experiments, further quantitative studies are needed to reach a conclusive statement, especially in the larger Q^2 range. On the theoretical side, various dispersion theoretical approaches have been developed in recent years, see (Ahmed *et al.*, 2020; Borisyuk and Kobushkin, 2015; Tomalak *et al.*, 2017b) and older references therein, which relate the TPE amplitudes at intermediate Q^2 values to empirical input on the electromagnetic structure of the nucleon and its excitations, while at very large Q^2 approaches based on perturbative QCD have been proposed (Borisyuk and Kobushkin, 2009; Chen *et al.*, 2004; Kivel and Vanderhaeghen, 2013, 2009). Further experiments investigating the TPE effect at larger values of Q^2 will be highly desirable to further test and constrain the TPE model descriptions.

In the low Q^2 region, the TPE effect can be predicted with less model dependence (Hill *et al.*, 2013; Tomalak *et al.*, 2017a). Especially in the forward angular range, relevant for the proton electric charge radius determination from elastic e-p scattering, it is found to be understood at the level of precision of current experiments. The TPE effect increases for the backward angular range, where a better understanding is required for improving the extraction of the proton magnetic radius.

G. Radiative Corrections in Electron Scattering

Besides the TPE correction corresponding with two hard photons in Fig. 9, another important aspect associated with lepton scattering, especially with electron scattering is the so-called radiative correction (RC) effect to the OPE picture. RC refers to effects from various types of radiation and soft-photon exchanges in electron scattering which need to be corrected before one can extract information such as the proton electric and magnetic form factors defined in the OPE picture. A few examples can be the initial state electron radiates a photon prior to the scattering, or the final state electron radiates a photon before it is detected in the detector. Similar pictures can be applied to the proton side, though such radiative effects are suppressed because the proton mass is significantly larger than that of an electron. A different way to look at the proton side is that such RC effect in principle can be included in the definition of the proton electric and magnetic form factors. Another important RC contribution is due to the QED vacuum polarization, which refers to the fact that a virtual photon can fluctuate into an electron-positron pair before they are absorbed, and the vertex correction on electron and proton sides. Furthermore, the radiative corrections conventionally also include a part of the TPE correction, in which one of the photons in the box diagram of Fig. 9 has a soft four-momentum. These are just examples of leading-order RC contributions, which are at the next-to-leading order compared to the leading-order OPE in electron-proton scattering. Two classic review articles on this subject still widely used and cited are by Mo and Tsai (Mo and Tsai, 1969) and by Maximon (Maximon, 1969). In recent years, there have been renewed interests in performing and pushing the state-of-the-art calculations on RC for various lepton-nucleon scattering processes not only due to the demand from the experimental side to improve precision, but also due to the need for other processes such as semi-inclusive deep-inelastic-scattering to probe partonic three-dimensional momentum distributions and fragmentation functions. The effect of RC is also experiment specific for which we refer readers to specific experiments that are discussed in this review for further details.

H. The Extraction of the Proton Charge Radius from Proton Electric Form Factor

The proton charge radius can be extracted from the experimentally determined proton electric form factor values. According to Eq. (36), the proton rms charge radius is directly related to the G_{Ep} Q^2-slope at $Q^2 = 0$. Experimentally this is of course not possible due to the requirement of conducting electron-proton elastic scattering at zero-degree scattering angle. Therefore, while it is important to reach as low a Q^2 value as possible, it is inevitable that one needs to extrapolate from the measured values of Q^2 down to zero. Furthermore, it is also important for any scattering experiment to cover a sufficient range of Q^2, i.e. to have a good leverage in Q^2 coverage. When Q^2 is sufficiently close to zero, the slope becomes rather flat because G_E would converge to 1, which is just the net charge of the proton as expected. Therefore, it is important to experimentally cover a Q^2 range in which one can capture whatever a Q^2 dependence nature calls for, and at the same time still be as close to $Q^2 = 0$ as practically possible.

Given the aforementioned limitations, it is important to develop ways that allow for a robust extraction of the proton charge radius. Such a study was carried out by Yan *et al.* (Yan *et al.*, 2018). Below we briefly describe this study. Pseudo-data sets on the proton electric form factor are generated for a particular experiment or a planned measurement according to various proton electromagnetic form factor parametrizations/models in the literature. These parametrizations/models in general describe the existing data on the proton form factors well. One then smears the generated pseudo data sets according to the experimental resolutions, and any other relevant experimental aspects such as the statistical and systematic uncertainties. The way to take into account the experimental systematic uncertainties is quite elaborate and we refer interested readers to the original paper (Yan *et al.*, 2018) for more details. One then fits the smeared data sets to various functional forms and extracts for each functional form the corresponding proton charge radius value, r_{Ep}, and its uncertainty, δr_{Ep}. The bias is defined as the difference between the input r_{Ep} value from the parameterization/model used to generate the pseudo-data set in the first place, and the r_{Ep} obtained from the fit. The goodness of a fit is to consider both the bias and the variance from the fit by using the root-mean-square error (RMSE) defined as $RMSE = \sqrt{bias^2 + \sigma^2}$.

The functional forms studied by Yan *et al.* (Yan *et al.*, 2018) include monopole, dipole, Gaussian, multi-parameter polynomial expansion of Q^2, multi-parameter rational function of Q^2, continuous fractional (CF) expansion of Q^2, and also the multi-parameter polynomial expansion of z, defined as:

$$z = \frac{\sqrt{t_{cut} + Q^2} - \sqrt{t_{cut} - t_0}}{\sqrt{t_{cut} + Q^2} + \sqrt{t_{cut} - t_0}}, \tag{54}$$

where $t_{cut} = 4m_\pi^2$ corresponds to the threshold for the lowest 2π intermediate state in the timelike region, with m_π being the mass of π^0, and t_0 is a free parameter set to zero in (Yan *et al.*, 2018). So the full functional form is expressed as:

$$f_{polyz}(Q^2) = p_0 G_E(Q^2) = p_0(1 + \sum_{i=1}^{N} p_i z^i). \tag{55}$$

The CF expansion form is expressed as:

$$f_{CF}(Q^2) = p_0 G_E(Q^2) = p_0 \frac{1}{1 + \frac{p_1 Q^2}{1 + \frac{p_2 Q^2}{1 + \dots}}}, \tag{56}$$

and has been used previously in (Griffioen and Maddox, 2016; Hill and Paz, 2010) to extract the proton charge radius from proton electric form factor values.

The multi-parameter rational function of Q^2 is written as:

$$f_{rational}(Q^2) = p_0 G_E(Q^2) = p_0 \frac{1 + \sum_{i=1}^{N} p_i^{(a)} Q^{2i}}{1 + \sum_{j=1}^{M} p_j^{(b)} Q^{2j}}. \tag{57}$$

In all these functional forms of Eqs. (55,56,57), the p_0 is a floating normalization parameter. For the PRad experiment (Xiong *et al.*, 2019) in its entire data range, the study found that the $(N = M = 1) = (1, 1)$ rational function, the two-parameter continued fraction, and the second-order polynomial expansion in z can all extract the proton charge radius in a robust way with small variance independent of the model or parameterization used for generating the pseudo data. The published r_{Ep} result (Xiong *et al.*, 2019) from the PRad experiment is based on fits to the rational (1,1) function. While in (Yan *et al.*, 2018) the case study was presented for the PRad experiment, the approach can be applied to any lepton scattering experiment to extract the proton charge radius.

IV. ATOMIC HYDROGEN SPECTROSCOPY

The proton charge radius is an important input to QED calculations of bound states such as ordinary atomic hydrogen and muonic hydrogen. High precision spectroscopic measurements, combined with the state-of-the-art QED calculations, can determine the proton charge radius. In this section, we provide a brief discussion and focus on aspects most relevant to the finite size of the proton due to our interest in the determination of the proton charge radius. We follow closely the review paper by Eides, Grotch and Shelyuto (Eides, 2001), to which we refer for a comprehensive discussion of the QED calculations including various higher-order effects.

The energy levels for one-lepton atoms can be obtained in the first approximation by solving the non-relativistic Schrödinger equation for an electron in the field of an infinitely heavy Coulomb center with a charge Z in units of the proton charge. The energy levels are written as:

$$E_n = -\frac{m(Z\alpha)^2}{2n^2}, \tag{58}$$

where $n = 1, 2, 3, ...$ is the principal quantum number, α the fine structure constant, and m is the mass of the lepton. Considering the Coulomb source still to be infinitely heavy, solving the Dirac equation for a lepton in such a Coulomb field, one obtains the following Dirac spectrum:

$$E_{nj} = mf(n, j), \tag{59}$$

where

$$\begin{aligned} f(n,j) &= \left[1 + \frac{(Z\alpha)^2}{\left(\sqrt{(j+\frac{1}{2})^2 - (Z\alpha)^2} + n - j - \frac{1}{2}\right)^2}\right]^{-1/2} \\ &\approx 1 - \frac{(Z\alpha)^2}{2n^2} - \frac{(Z\alpha)^4}{2n^3}\left(\frac{1}{j+1/2} - \frac{3}{4n}\right) - \frac{(Z\alpha)^6}{8n^3}\left[\frac{1}{(j+1/2)^3} + \frac{3}{n(j+1/2)^2} + \frac{5}{2n^3} - \frac{6}{n^2(j+1/2)}\right] + ..., \end{aligned} \tag{60}$$

where $j = 1/2, 3/2, ...n - 1/2$ is the total angular momentum of the state. Compared with the nonrelativistic Schrödinger spectrum – where all levels with the same n are degenerate – the energy levels in the Dirac spectrum with the same principal quantum number n but different j are no longer degenerate. However, energy levels with the same n and j, but different $l = j \pm 1/2$ remain degenerate. Such degeneracy is lifted when one takes into account the finite size of the proton, recoil contributions and most importantly the QED loop corrections, where the corresponding energy shifts are called the Lamb shifts. Details on calculating the QED radiative corrections, recoil and radiative-recoil corrections can be found in (Eides, 2001).

Below we briefly review the leading relativistic corrections with exact mass dependence in the external field approximation following (Eides, 2001). For a nonrelativistic system of two particles with Coulomb interaction such as a hydrogen atom, the Hamiltonian in its center-of-mass system can be written as:

$$H_0 = \frac{\mathbf{p}^2}{2m} + \frac{\mathbf{p}^2}{2M} - \frac{Z\alpha}{r}, \tag{61}$$

where $\mathbf{p}$ is the momentum, and in the case of hydrogen (muonic hydrogen), $Z = 1$, and where m and M are the masses of the electron (muon), and the proton, respectively. In the remainder of this section, we will focus on hydrogenlike atoms only. For a nonrelativistic loosely bound system such as a hydrogen atom, expansions over α^2 correspond to expansions over v^2/c^2. Therefore, an effective Hamiltonian including terms of the first order in v^2/c^2 would provide proper corrections of relative order α^2 to the nonrelativistic energy levels. Breit (Breit, 1929, 1930, 1932) proposed such a potential realizing that all corrections to the nonrelativistic two-particle Hamiltonian of the first order in v^2/c^2 can be written as the sum of the free relativistic Hamiltonian of each of the particles and the relativistic one-photon exchange between the two. Barker and Glover (Barker, 1955) derived the following Breit potential from the one-photon-exchange amplitude using the Foldy-Wouthuysen transformation (Foldy, 1950):

$$V_{Br} = \frac{\pi\alpha}{2}\left(\frac{1}{m^2}+\frac{1}{M^2}\right)\delta^3(\mathbf{r}) - \frac{\alpha}{2mMr}\left(\mathbf{p}^2 + \frac{\mathbf{r}(\mathbf{r}\cdot\mathbf{p})\cdot\mathbf{p}}{r^2}\right) + \frac{\alpha}{r^3}\left(\frac{1}{4m^2}+\frac{1}{2mM}\right)[\mathbf{r}\times\mathbf{p}]\cdot\vec{\sigma}. \tag{62}$$

In the above potential, the hyperfine structure is not considered, i.e., terms which depend on the proton spin are omitted. The corrections to the energy levels up to order α^4 can be calculated from the total Breit Hamiltonian of $H_{Br} = H_0 + V_{Br}$, where the interaction potential is the sum of the Coulomb and the Breit Potential. These corrections are just the first-order matrix elements of the Breit interaction between the eigenfunctions of the Coulomb Hamiltonian H_0, and the result is

$$E^{tot}_{nj} = (m+M) - \frac{m_r\alpha^2}{2n^2} - \frac{m_r\alpha^4}{2n^3}\left(\frac{1}{j+1/2} - \frac{3}{4n} + \frac{m_r}{4n(m+M)}\right) + \frac{\alpha^4 m_r^3}{2n^3M^2}\left(\frac{1}{j+1/2} - \frac{1}{l+1/2}\right)(1-\delta_{l0}), \tag{63}$$

where $m_r = mM/(m+M)$ is the reduced mass of the hydrogenlike atom. One can see that the last term in Eq. (63) breaks the degeneracy in the Dirac spectrum between states with the same j and $l = j \pm 1/2$, and contributes to the classical Lamb shift defined as $E(2P_{1/2}) - E(2S_{1/2})$. However, due to the smallness of the electron to proton mass ratio, the contribution of this term is extremely small in the hydrogen case and the leading contribution to the Lamb shift is the QED radiative correction. Fig 10 shows the hydrogen $1S$, $2S$ and $2P$ energy levels.

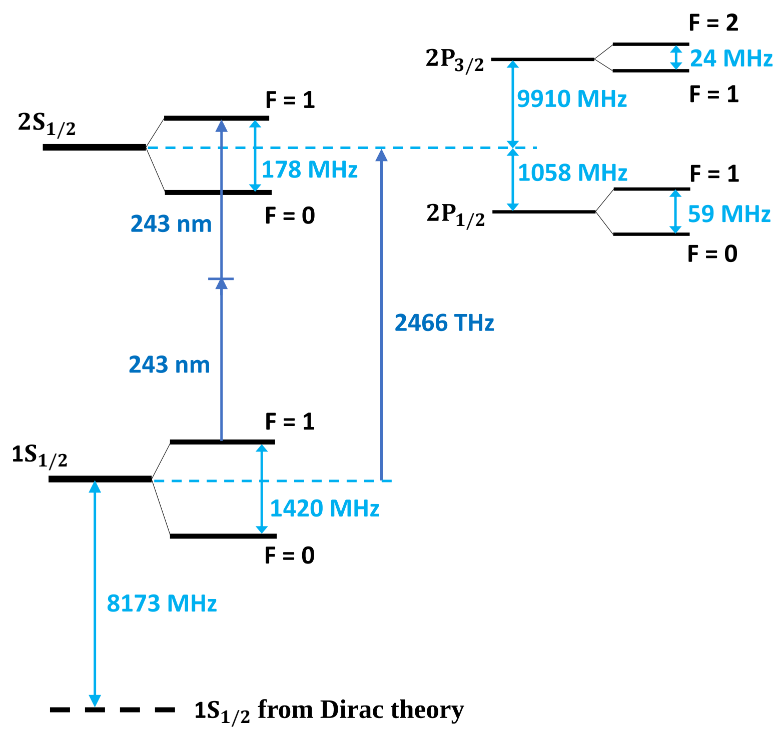

FIG. 10 (Color online) Hydrogen $1S$, $2S$, and $2P$ energy levels (figure credit: Jingyi Zhou).

In the discussion so far, the proton has been treated as a point-like charge. Eq. (3) provides the photon-proton vertex operator involving the Dirac (F_1) and Pauli (F_2) form factors of the proton. Calculating the finite size contribution to the hydrogen atom energy levels amounts to evaluating the zero component of Eq. (3) between nucleon spinors, normalized as $N^\dagger N = 1$. An elementary calculation yields the spin independent term at low momentum transfer $\mathbf{q} \equiv \mathbf{p'} - \mathbf{p}$ (Eides, 2001), see e.g. (Miller, 2019) for an explicit derivation, as:

$$N(p',\lambda)\Gamma^0 N(p,\lambda) = \left(1 - \frac{\mathbf{q}^2}{8M^2}\right) G_E(-\mathbf{q}^2) + \mathcal{O}\left(\frac{1}{M^4}\right) \\ \approx 1 - \mathbf{q}^2 \left[\frac{1}{8M^2} + \frac{1}{6}\langle r_{Ep}^2\rangle\right], \tag{64}$$

where in the last line we have used the low-momentum expansion of the proton electric form factor G_E in terms of the proton charge radius $\langle r_{Ep}^2\rangle$, defined through Eq. (36). For a point-like proton, the only term that survives in Eq. (64) is the first term in the square brackets, which leads to the well-known local Darwin term in the lepton-proton interaction (Barker, 1955) that gives rise to the term proportional to δ_{l0} in Eq. (63). Note that the leading relativistic correction factor in front of G_E in Eq. (64) is the same as the one appearing in Eq. (7). The established convention is not to include it in the definition of G_E, but to include it separately. Therefore, the leading nuclear (proton) structure contribution to the energy shift is determined by the slope of the conventionally defined nuclear (proton) form factor G_E. The corresponding perturbative potential which corrects the Coulomb potential of a point charge to account for the finite proton size is therefore given by (Eides, 2001)

$$\delta V_{\text{fin.size}} = \frac{2\pi\alpha}{3}\langle r_{Ep}^2\rangle. \tag{65}$$

The associated energy level shift is then

$$\Delta E_{\text{fin.size}} = \frac{2\pi\alpha}{3}\langle r_{Ep}^2\rangle|\psi_{nl}(0)|^2, \\ = \frac{2\alpha^4}{3n^3} m_r^3 \langle r_{Ep}^2\rangle \delta_{l0}. \tag{66}$$

One notices from Eq. (66) that the radius entering the finite size correction to the S-levels of the hydrogen atom is the proton charge radius, obtained from the form factor G_E as measured in electron-proton scattering experiments. This consistency between the proton charge radius determined from spectroscopic experiments of hydrogenlike atoms and from electron scattering experiments has also been emphasized recently in (Miller, 2019).

While the Lamb shift of hydrogenlike atoms is dominated by the QED radiative effects of the lepton, the contribution from the proton charge radius is the leading term due to the finite size of the proton. By measuring Lamb shifts or other transitions between energy levels involving at least one S-state of hydrogenlike atoms precisely and utilizing the state-of-the-art QED calculations, one can determine the proton charge radius value. In the case of muonic hydrogen, the proton charge radius effect is 6.4×10^6 times larger compared to that of ordinary hydrogen atoms for the same nS level, due to the m_r^3 dependence. For the $2P - 2S$ Lamb shift in muonic hydrogen, the term due to the proton charge radius amounts to around -3.7 meV, and contributes to about 2% of the overall Lamb shift (Eides, 2001). This large relative contribution is the important reason why muonic hydrogen spectroscopic measurements are significantly more precise in extracting the proton charge radius than those from ordinary hydrogen atoms.

In order to extract the proton radius from muonic hydrogen spectroscopic measurements accurately, it is important to also calculate the proton structure corrections of next order in α, i.e. $\mathcal{O}(\alpha^5)$. These proton structure corrections, which arise from the two-photon exchange (TPE) diagram shown in Fig. 11, in which both photons in the loop carry the same four-momentum, are known as the polarizability correction. They have been evaluated using different approaches: chiral effective field theory, see (Hagelstein *et al.*, 2016) and references therein for a review of the ongoing activity in this field; within non-relativistic QED (Dye *et al.*, 2016; Hill *et al.*, 2013; Hill and Paz, 2011; Pineda, 2003); or by connecting them model-independently to other data through dispersive frameworks (Birse, 2012; Carlson and Vanderhaeghen, 2011; Pachucki, 1999).

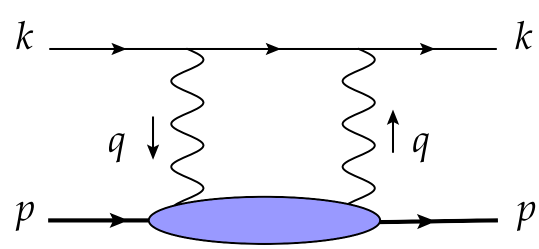

FIG. 11 (Color online) The box diagram for the $\mathcal{O}(\alpha^5)$ corrections to $l = 0$ energy levels in muonic hydrogen. The blob denotes all possible hadronic intermediate states.

The n-th S-level shift in the (muonic) hydrogen spectrum due to TPE is related to the spin-independent *forward* double virtual Compton amplitudes as:

$$\Delta E_{\rm TPE}(nS) = 8\pi e^2 m\,\phi_n^2\,\frac{1}{i}\int_{-\infty}^{\infty}\frac{d\nu}{2\pi}\int\frac{d^3\mathbf{q}}{(2\pi)^3}\frac{\left(Q^2-2\nu^2\right)T_1(\nu,Q^2)-(Q^2+\nu^2)\,T_2(\nu,Q^2)}{Q^4(Q^4-4m^2\nu^2)}, \tag{67}$$

where $\phi_n^2 = 1/(\pi n^3 a^3)$ is the wave function at the origin and $a^{-1} = \alpha m_r$ is the inverse Bohr radius. Furthermore, T_1 and T_2 are the forward double virtual Compton amplitudes which are complex functions of photon energy ν and photon virtuality Q^2. The optical theorem relates the imaginary parts of T_1 and T_2 to the two unpolarized structure functions of inclusive electron-nucleon scattering as:

$$\begin{aligned}\text{Im}\; T_1(\nu,\, Q^2) &= \frac{e^2}{4M} F_1(x,\, Q^2)\,,\\ \text{Im}\; T_2(\nu,\, Q^2) &= \frac{e^2}{4\nu} F_2(x,\, Q^2)\,,\end{aligned} \tag{68}$$

where $x \equiv Q^2/2M\nu$, and where F_1, F_2 are the conventionally defined structure functions parametrizing inclusive electron-nucleon scattering.

The TPE contribution to the hydrogen spectrum can be separated in two distinct contributions. Firstly a Born contribution, which corresponds with the nucleon intermediate state in Fig. 11 and depends solely on the elastic nucleon Dirac and Pauli form factors. Secondly a polarizability contribution, corresponding to all non-Born contributions to T_1 and T_2, denoted by $\bar{T}_i \equiv T_i - T_i^{\rm Born}$, which depends on the excitation spectrum of the nucleon.

The polarizability effect on the hydrogen spectrum can be further split into the contribution of the subtraction function $\bar{T}_1(0, Q^2)$ (Carlson and Vanderhaeghen, 2011):

$$\Delta E^{\rm subtr.}(nS) = \frac{2e^2 m\,\phi_n^2}{\pi}\int_0^\infty \frac{dQ}{Q^3}\frac{v_l+2}{(1+v_l)^2}\,\bar{T}_1(0,Q^2), \tag{69}$$

with $v_l = \sqrt{1+4m^2/Q^2}$, and contributions of the inelastic structure functions (Carlson and Vanderhaeghen, 2011; Hagelstein *et al.*, 2016):

$$\begin{aligned}\Delta E^{\rm inel.}(nS) = &-32\alpha^2 Mm\,\phi_n^2\int_0^\infty\frac{dQ}{Q^5}\int_0^{x_0}dx\frac{1}{(1+v_l)(1+\sqrt{1+x^2\tau^{-1}})}\\ &\times\left\{\left[1+\frac{v_l\sqrt{1+x^2\tau^{-1}}}{v_l+\sqrt{1+x^2\tau^{-1}}}\right]F_2(x,Q^2)+\frac{2x}{(1+v_l)(1+\sqrt{1+x^2\tau^{-1}})}\left[2+\frac{3+v_l\sqrt{1+x^2\tau^{-1}}}{v_l+\sqrt{1+x^2\tau^{-1}}}\right]F_1(x,Q^2)\right\},\\ &,\end{aligned} \tag{70}$$

with τ as in Eq. (42), and x_0 the πN inelastic threshold in the hadronic blob in Fig. 11.

Table III shows the TPE corrections due to the inelastic structure functions estimate of (Carlson and Vanderhaeghen, 2011) and resulting from the subtraction-function estimate of (Birse, 2012), both of which are currently used in estimating the total polarizability contribution to the $2S$-level in the muonic hydrogen analyses (Antognini *et al.*, 2013b). The estimate of (Birse, 2012) assumes a dipole ansatz for $\bar{T}_1(0,Q^2)/Q^2$, and constrains the mass parameter by a HBChPT calculation to fourth-order in the chiral expansion for the Q^4 term in $\bar{T}_1(0,Q^2)$. We compare these results with the LO BChPT analysis of (Alarcon *et al.*, 2014), a NLO BChPT analysis which includes the Δ-pole contribution (Hagelstein, 2017; Lensky *et al.*, 2018), and with the NLO HBChPT analysis of (Peset and Pineda, 2014). One notices that the BChPT result which includes the Δ-pole is in very good agreement with the DR estimate for the inelastic contribution and with the estimate of (Birse, 2012) for the subtraction function contribution. It is also interesting that, although the Δ-pole contributes sizeably to both terms, these contributions come with opposite sign, resulting in a small total polarizability contribution due to the Δ-pole, and a total result close to the LO BChPT estimate. The NLO HBChPT estimate (Peset and Pineda, 2014), shown in the last column of Table III comes with a larger error estimate, and its value is larger (in magnitude), deviating by about 2σ from the BChPT and DR estimates. It was noticed however (Peset and Pineda, 2014), that upon adding the nucleon Born term contributions it yields a total TPE result which is similar in size as the DR and BChPT results.

Recall that the Lamb shift is the difference between the shifts of the $2P$ and $2S$ levels; the TPE contribution to the former is negligible, and the TPE contribution to the Lamb shift is thus just $-\Delta E_{\rm TPE}(2S)$.

Using dispersion relations, with input from forward proton structure functions and a subtraction function, the value for the $\mathcal{O}(\alpha^5)$ TPE proton structure correction to the $2P-2S$ Lamb shift which is presently used in the extraction of the proton charge radius from the muonic hydrogen Lamb shift measurements as discussed further in Section VI, is given by (Antognini *et al.*, 2013b; Birse,

	DR + HBChPT	BChPT (LO) (Alarcon *et al.*, 2014)	BChPT (LO + Δ) (Hagelstein, 2017), (Lensky *et al.*, 2018)	HBChPT (NLO) (Peset and Pineda, 2014)
$\Delta E^{\text{inel.}}$	-12.7 ± 0.5 (Carlson and Vanderhaeghen, 2011)	-5.2	-11.8	–
$\Delta E^{\text{subtr.}}$	4.2 ± 1.0 (Birse, 2012)	-3.0	4.6	–
$\Delta E^{\text{pol.}}$	-8.5 ± 1.1 (Antognini *et al.*, 2013b)	$-8.2^{+1.2}_{-2.5}$	$-7.2^{+1.2}_{-2.5}$	-26.2 ± 10.0

TABLE III TPE corrections to the $2S$-level in muonic hydrogen. All values are given in μeV. The first two rows are the dispersive, $\Delta E^{\text{inel.}}$, and subtraction function, $\Delta E^{\text{subtr.}}$, contributions. The sum of both yields the total polarizability contribution, $\Delta E^{\text{pol.}}$.

2012; Carlson and Vanderhaeghen, 2011):

$$\Delta E_{TPE}(2P - 2S) = 0.0332(20) \text{ meV}. \qquad (71)$$

V. MODERN LEPTON SCATTERING EXPERIMENTS

A. Mainz 2010

Bernauer *et al.* (Bernauer *et al.*, 2010) (the A1 Collaboration) carried out an unpolarized electron-proton elastic scattering experiment at the Mainz accelerator facility MAMI and extracted the proton charge and the magnetic radii. The experiment utilized electron beam energies up to 855 (180, 315, 450, 585, 720 and 855) MeV and three high-resolution magnetic spectrometers with one serving as a relative luminosity monitor at a fixed laboratory angle. The other two spectrometers were moved as a function of electron scattering angle during the experiment to provide the kinematic coverage and also redundancy in the coverage. The targets used in this experiment were 2 and 5 cm long cells filled with liquid hydrogen. Fig. 12 shows the schematics of the three-spectrometer setup for this experiment (top) and a photo of the setup is shown at the bottom where the red, blue and green apparatus are spectrometer A, B and C, respectively.

In total the experiment measured over 1400 differential cross sections covering a Q^2 range of 0.004 to 1 (GeV/c)^2 and achieved a statistical precision better than 0.2% for these cross section measurements. To extract the proton electric and magnetic form factors, least square fits to models of G_{Ep} and G_{Mp} were carried out on the 1400 cross section data points, covering all Q^2 and scattering angles of the experiment. The proton form factors up to $Q^2 = 0.6$ (GeV/c)^2 were extracted from this approach. The authors carried out detailed studies of model dependence in extracting the proton form factors using various form factor models and parameterizations. The experiment extracted the following for the proton charge and magnetic radii:

$$\langle r^2_{Ep}\rangle^{1/2} = 0.879(5)_{stat}(4)_{syst}(2)_{model}(4)_{group} \text{ fm},$$
$$\langle r^2_{Mp}\rangle^{1/2} = 0.777(13)_{stat}(9)_{syst}(5)_{model}(2)_{group} \text{ fm},$$

where the uncertainty labeled as "group" is assigned to account for the difference between the radius values obtained using two groups of models for the form factors in the fits, namely the spline and the polynomial groups. Details can be found in (Bernauer *et al.*, 2010, 2014). The result on the proton charge radius from this electron scattering experiment was consistent with the CODATA06 (Mohr, 2008) value at the time of the publication, but 5 standard deviations larger than the value from the muonic hydrogen Lamb shift measurement (Pohl *et al.*, 2010). The magnetic radius obtained is smaller than those from previous fits of electron scattering data, but consistent with the result of 0.778(29) (Volotka *et al.*, 2005) fm from hyperfine splitting in hydrogen.

B. JLab recoil polarization experiment

The Jefferson Lab experiment E08-007 (Zhan *et al.*, 2011) carried out a high-precision measurement of the polarization transfer from electron-proton elastic scattering using a recoil proton polarimeter covering a momentum transfer squared Q^2 region between 0.3 to 0.7 (GeV/c)^2. The experiment was performed in Hall A and utilized a longitudinally polarized electron beam with polarization higher than 80% at 1.2 GeV, beam currents between 4 and 15 μ-A, and a 6-cm long unpolarized liquid hydrogen target. There were two high-resolution magnetic spectrometers (HRS) in Hall A placed on each side of the electron beam line. In E08-007, the recoil proton was detected in the left HRS with its polarization being measured by a focal plane polarimeter, in coincidence with the scattered electron which was measured in a large acceptance spectrometer ("BigBite"). The experiment extracted the proton electric to magnetic form factor ratio $\mu_p G_{Ep}/G_{Mp}$ with a total uncertainty of about 1%. Using

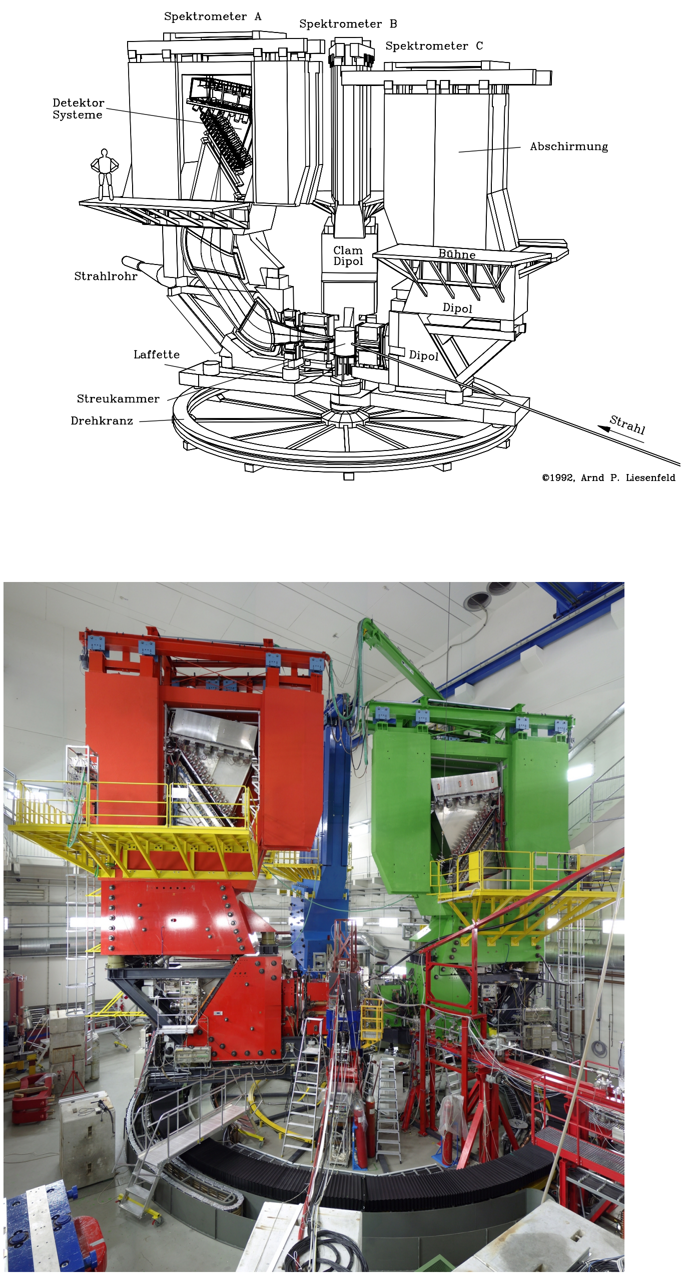

FIG. 12 (Color online) Top: the schematics of the three-spectrometer setup of the A1 experiment at Mainz, and a photo is shown at the bottom in which Spectrometer A, B and C are shown in red, blue and green respectively. The electron beam is from right to left (figure credit: Arnd P. Liesenfeld (top), and Markus Weis (bottom)).

these results together with a few other proton form factor ratio measurements from Jefferson Lab (Paolone *et al.*, 2010; Puckett *et al.*, 2010; Ron *et al.*, 2011), a global fit of the proton form factors (Arrington, 2007) was updated. This updated global analysis did not include the Mainz

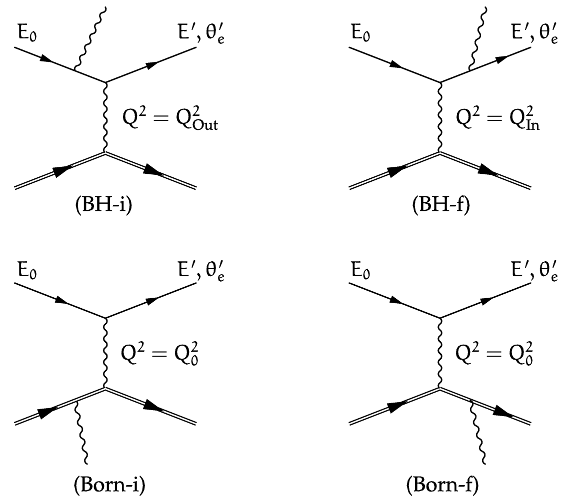

FIG. 13 (Color online) Feynman diagrams showing electron-proton scattering with electron or proton radiates a real photon in the initial state or final state. In the electron case, the two diagrams are labeled as Bethe-Heitler (BH-i) and (BH-f), while for the proton: (Born-i) and (Born-f), where i and f stand for the initial-state and final-state radiation, respectively. The figure is from (Mihovilovič *et al.*, 2017).

data (Bernauer *et al.*, 2010), and gave the following values for the proton electric and the magnetic charge radii:

$$\langle r^2_{Ep} \rangle^{1/2} = 0.875 \pm 0.010 \text{ fm},$$
$$\langle r^2_{Mp} \rangle^{1/2} = 0.867 \pm 0.020 \text{ fm}.$$

The proton charge radius value from this updated global analysis is in excellent agreement with the value from the Mainz electron-proton scattering experiment (Bernauer *et al.*, 2010), and also with the CODATA 2006 value (Mohr, 2008) which is based mostly from ordinary hydrogen spectroscopic measurements. It is in disagreement with the muonic hydrogen result (Pohl *et al.*, 2010). The magnetic radius value from this global analysis is more than 5 standard deviations (larger) away from the Mainz value (Bernauer *et al.*, 2010).

C. Mainz ISR measurements

Following the Mainz experiment by Bernauer *et al.* (Bernauer *et al.*, 2010), another electron-proton elastic scattering experiment at Mainz was carried out using the same three-spectrometer setup but reached lower values of Q^2 (0.001 to 0.004 GeV/c^2) using the technique of initial-state radiation (ISR) (Mihovilovič *et al.*, 2017). For electron-scattering experiments, the lowest Q^2 value that is achievable is determined by the lowest electron beam energy the associated accelerator can deliver, and the most forward electron scattering angle the corresponding detector can reach. The ISR technique overcomes such limits by utilizing the information within the radiative tail of the elastic peak. The technique works in the following way, as depicted by Fig. 13. The incoming electron can radiate a real photon before the scattering takes place. As a result, the corresponding Q^2 value for the e-p scattering would be lower than what's limited by the accelerator and the detector because the incident electron energy is lower than its original value delivered by the accelerator and before the initial state radiation of the real photon by the incoming electron. This is the diagram labeled as Bethe-Heitler (BH-i) in Fig. 13. Such an ISR technique was proposed and used successfully in particle physics experiments previously (Arbuzov *et al.*, 1998; Aubert *et al.*, 2004). One of the challenges of such an ISR experiment is in separating the contribution from the diagram labeled as (BH-f), where the scattered electron radiates a real photon, as only scattered electrons are measured (inclusive measurement). Furthermore, although contributions from diagrams involving the proton initial-state and final-state radiation are suppressed due to the proton mass, they need to be included as they also contribute to the radiative tail of the elastic scattering, as well as higher order radiative effects. For details on how to account for these effects, see (Mihovilovič *et al.*, 2017), which extracted a proton charge radius value of $\langle r_{Ep}^2\rangle^{1/2} = 0.810 \pm 0.035_{stat.} \pm 0.074_{syst.} \pm 0.003_{mod.}$ fm, with the last uncertainty accounting for higher moments in parameterizing the proton electric form factor. The collaboration reported a follow-up result through a comprehensive reinterpretation of the existing cross section data from this first ISR e-p scattering experiment by improving the description of the radiative tail. They obtained $\langle r_{Ep}^2\rangle^{1/2} = 0.878 \pm 0.011_{stat.} \pm 0.031_{syst.} \pm 0.002_{mod.}$ fm with major improvements in both the statistical and systematic uncertainties, see (Mihovilovič *et al.*, 2021).

D. The PRad experiment at JLab

The proton charge radius (PRad) experiment (Xiong *et al.*, 2019) at Jefferson Lab was designed with a number of important points in mind: (i) an experiment that is different from previous e-p scattering experiments, therefore having different systematics; (ii) the reach of unprecedentedly low values of Q^2; (iii) the ability to precisely measure e-p elastic scattering cross sections by accurate control of the integrated luminosity; (iv) minimizing changes during the experiment and taking all the data using a fixed experimental apparatus.

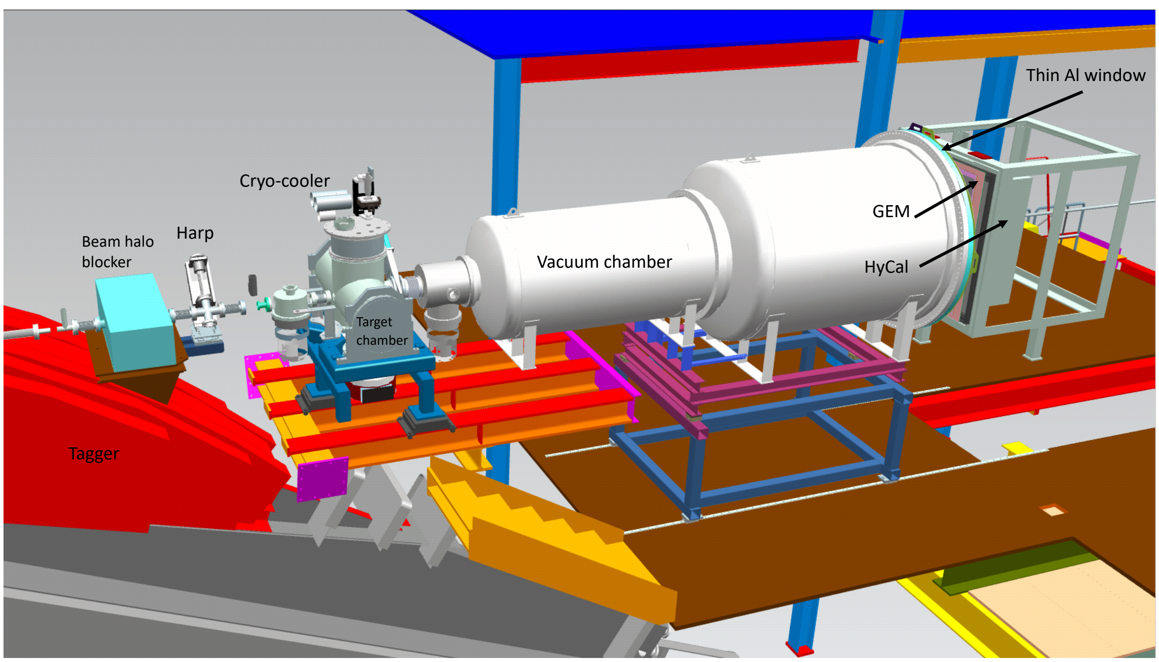

FIG. 14 (Color online) The schematics of the PRad experiment in Hall B at Jefferson Lab. In this figure, the electron beam is from left to right (figure credit: Eugene Pasyuk and others (Brock *et al.*, 2021)).

The PRad experiment innovated electron-scattering measurements in the following ways. Instead of using a magnetic spectrometer, which usually limits the forward-most scattering angles due to its physical size, the PRad experiment used a two-dimensional large-area, granular, high-resolution electromagnetic calorimeter with a hole at the center for the electron beam to pass through. The novel design allows the access to significantly smaller scattering angles ($\sim$ 0.7°) in comparison to experiments using magnetic spectrometers. To overcome major background issues associated with small-angle scattering, the PRad experiment used a windowless, cryogenically cooled, flowing hydrogen gas target. The internal target was a first for Jefferson Lab, giving the facility's electron beam unobstructed access to the windowless hydrogen target. In order to have an excellent control of the integrated luminosity for the electron-proton elastic scattering cross section measurements, Møller scattering, a well-known QED process, was used as a reference process and was measured simultaneously during the e-p scattering. Lastly, to improve the scattering angle (Q^2) determination, a large plane of Gas Electron Multiplier (GEM) detectors was used. The GEM detector used in PRad was the largest ever used in any experiment at the time.

The schematics of the PRad experiment are shown in Fig. 14, in which the electron beam is from left to right. PRad was the first experiment to complete its data taking in June 2016 after the Continuous Electron Beam Accelerator Facility (CEBAF) – consisting of a polarized electron source, an injector and a pair of superconducting radio frequency (RF) linear accelerators – energy upgrade from 6 GeV to 12 GeV at Jefferson Lab was completed. Two values of electron beam energies were used in the PRad experiment, 1.1 and 2.143 GeV. For the 1.1 GeV data set, most of the data were obtained at a beam current of 15 nA with the rest at 10 nA, while for the 2.143 GeV data, the nominal beam current was 55 nA. To minimize the background from the air, the scattered electrons traveled through a two-stage vacuum chamber followed by the GEM detector and a hybrid electromagnetic calorimeter (HyCal) built originally for precision measurements of the neutral pion lifetime (Larin *et al.*, 2011, 2020). More details about the PRad target and the experimental setup can be found in (Pierce *et al.*, 2021; Xiong *et al.*, 2019; Xiong, 2020).

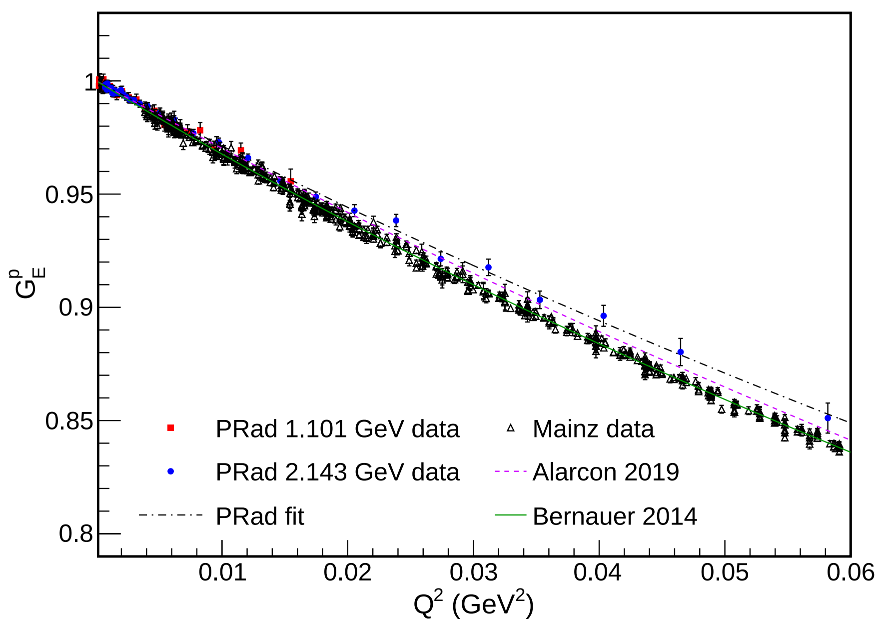

FIG. 15 (Color online) The proton electric form factor G_E^p from the PRad experiment together with results from the Mainz experiment (Bernauer *et al.*, 2010; Bernauer, Jan C., 2020) in the overlapping Q^2 region. Both data sets include statistical and systematic uncertainties (see text). Two fits of the PRad data (Alarcón *et al.*, 2019; Xiong *et al.*, 2019) and a fit of the Mainz data (Bernauer *et al.*, 2014) are also shown (figure credit: Weizhi Xiong).

The proton electric form factor values in the Q^2 range of 2×10^{-4} to 0.06 (GeV/c)^2 have been extracted from the PRad experiment with statistical uncertainties of $\sim$ 0.2% at 1.1 GeV, and $\sim$ 0.15% at 2.143 GeV per data point, respectively. The systematic uncertainties range from $\sim$ 0.1% to 0.6% (relative) for the entire PRad data set (Xiong, 2020). The PRad G_E^p results with statistical and systematic uncertainties combined in quadrature are presented in Fig. 15. The Mainz G_E^p results (Bernauer, Jan C., 2020) extracted from the Mainz experiment (Bernauer *et al.*, 2010) including both the statistical and systematic uncertainties in the Q^2 overlapping region of these two experiments are shown in Fig. 15. Also shown are the fits of the PRad results

(Alarcón *et al.*, 2019; Xiong *et al.*, 2019), and also a fit of the Mainz data (Bernauer *et al.*, 2014). In Fig. 16, additional G_E^p data from (Hand and Wilson, 1963; Murphy *et al.*, 1974b; Simon *et al.*, 1980) are also shown normalized to that of the standard dipole form. Other than the data by (Hand and Wilson, 1963) which has rather larger uncertainties, the PRad results are systematically higher than other data in the higher end of the Q^2 range covered by the PRad experiment, specifically $\sim$ 0.03 (GeV/c)^2 and higher.

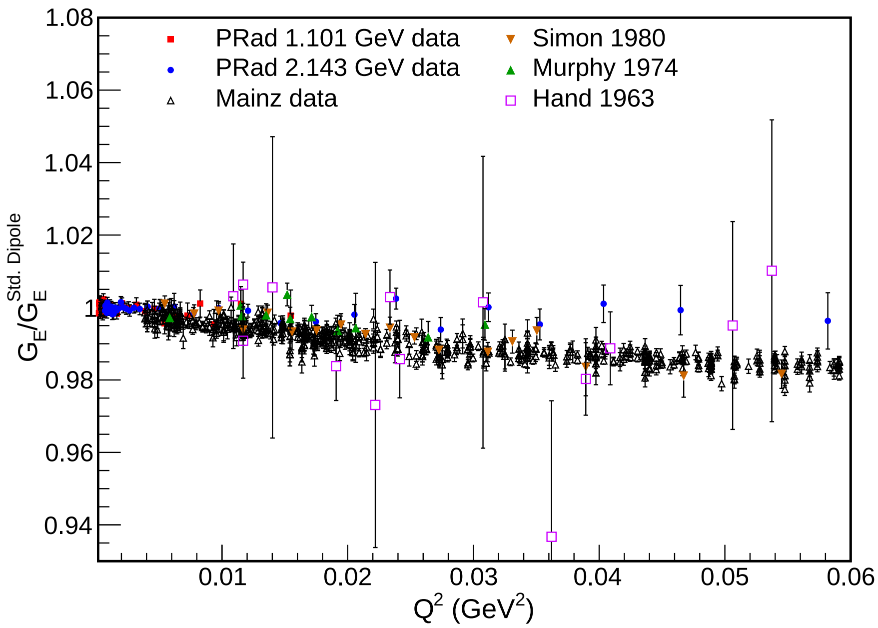

FIG. 16 (Color online) The proton electric form factor G_E^p from the PRad experiment together with those from (Bernauer, Jan C., 2020; Hand and Wilson, 1963; Murphy *et al.*, 1974b; Simon *et al.*, 1980) normalized to the standard dipole form in the overlapping Q^2 region, on linear scale (figure credit: Weizhi Xiong).

Yan *et al.* (Yan *et al.*, 2018) studied how to extract the proton charge radius in the low Q^2 region from the measured G_E^p values in a robust way and demonstrated that the rational (1,1) function, defined in Eq. (57) is such a function and the best choice for the PRad data. Fig. 17 shows fits using various rational functions of pseudo-data generated with nine proton form factor models including the projected PRad statistical and systematic uncertainties. Apart from monopole, dipole and Gaussian functional forms, the proton form factor parameterizations and fits from (Alarcón and Weiss, 2018; Arrington, 2007; Bernauer *et al.*, 2014; Kelly, 2004; Ye *et al.*, 2018) have been used. Additional details including fits of other functional forms can be found in (Yan *et al.*, 2018). The PRad collaboration adopted the rational (1,1) functional form to fit the data with two individual normalization parameters, n_1 and n_2, corresponding to the two separate beam energy values for which the data were taken, while keeping the rest of the rational (1,1) parameters the same, i.e. $n_1\frac{1+p_1Q^2}{1+p_2Q^2}$, and $n_2\frac{1+p_1Q^2}{1+p_2Q^2}$. At $Q^2=0$, this normalization parameter is just the proton charge, which should be 1. The results from the fit are given by:

$$\begin{aligned}\langle r_{Ep}^2\rangle^{1/2} &= 0.831\pm0.007(\text{stat.})\pm0.012(\text{syst.})\ \text{fm},\\ n_1 &= 1.0002\pm0.0002(\text{stat.})\pm0.0020(\text{syst.}),\\ n_2 &= 0.9983\pm0.0002(\text{stat.})\pm0.0013(\text{syst.}),\end{aligned}\tag{72}$$

showing that the two normalization values obtained are consistent with 1.

The PRad result for the proton charge radius is smaller than the two latest $\langle r_{Ep}^2\rangle^{1/2}$ values extracted from electron scattering experiments (Bernauer *et al.*, 2010; Zhan *et al.*, 2011), but consistent with the $\langle r_{Ep}^2\rangle^{1/2}$ values from the muonic hydrogen spectroscopic measurements (Antognini *et al.*, 2013a; Pohl *et al.*, 2010). While this result is also consistent with two recent hydrogen spectroscopic measurements (Beyer *et al.*, 2017; Bezginov *et al.*, 2019), it is not consistent with (Fleurbaey *et al.*, 2018). These latest hydrogen spectroscopic measurements will be discussed in later sections.

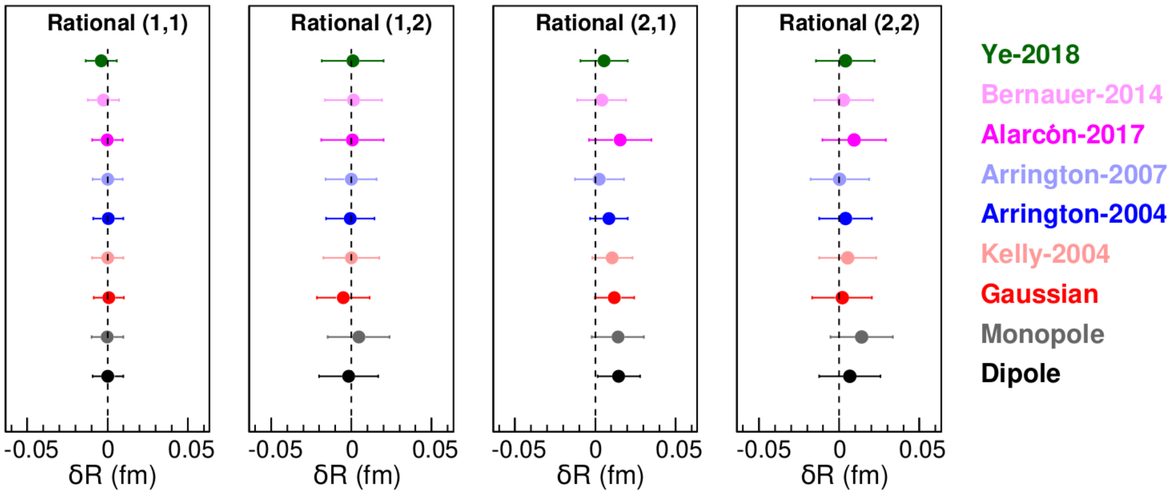

FIG. 17 (Color online) Sample fits using rational functions of pseudo-data generated with nine proton form factor models including the projected PRad statistical and systematic uncertainties. The figure is from (Yan *et al.*, 2018).

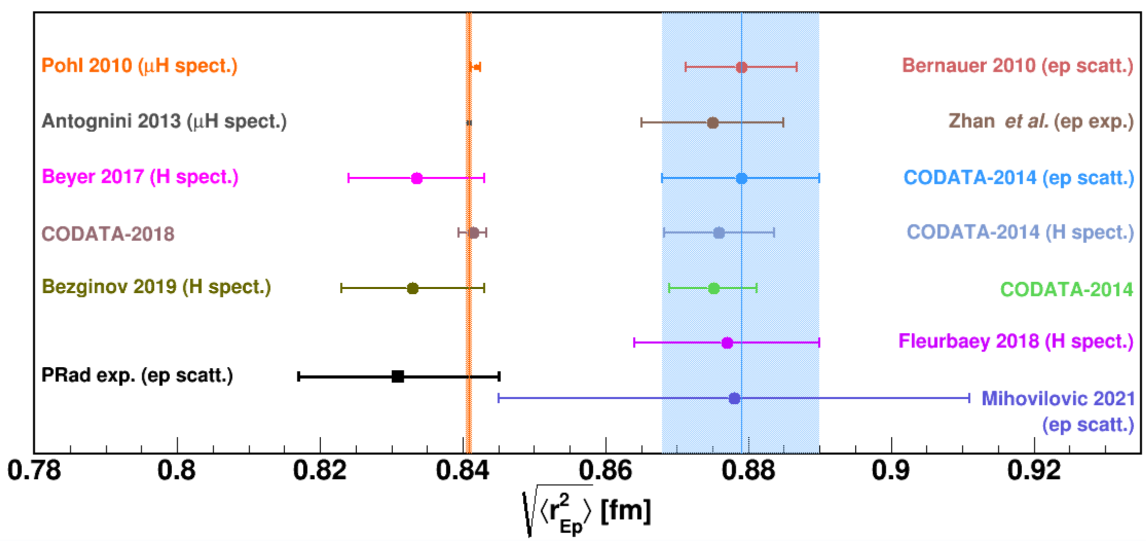

FIG. 18 (Color online) The proton charge radius $\langle r^2_{Ep}\rangle^{1/2}$ as extracted from electron scattering and spectroscopic experiments since 2010 and before 2020 together with CODATA-2014 and CODATA-2018 recommended values. Note the reinterpreted result from the Mainz ISR experiment is published in 2021 (figure credit: Jingyi Zhou).

Fig. 18 shows the PRad result for the proton charge radius together with the recent results from the hydrogen spectrocopic measurements, and the muonic hydrogen results. Also shown are the latest CODATA-2018 value (Tiesinga *et al.*, 2021), CODATA-2014 values (Mohr *et al.*, 2016), results from (Bernauer *et al.*, 2010; Zhan *et al.*, 2011) and also the result from the Mainz ISR experiment (Mihovilovič *et al.*, 2021). One interesting observation is that among the most precise measurements from hydrogen spectroscopic and electron scattering measurements in recent years (Beyer *et al.*, 2017; Bezginov *et al.*, 2019; Fleurbaey *et al.*, 2018; Xiong *et al.*, 2019), three experiments reported a value that is smaller than the one from the muonic results, though they are all consistent within experimental uncertainties. Improving the precision of such measurements will be crucial to investigate whether there might be a substantiated difference between results from muonic versus electronic systems.

E. Proton charge radius from modern analyses of proton electric form factor data

In addition to new experiments, numerous analyses have been carried out in recent years in order to understand the difference between the $\langle r_{Ep}^2\rangle^{1/2}$ values determined from electron scattering experiments, especially the modern precision electron-proton scattering experiment at Mainz (Bernauer *et al.*, 2010), and the muonic hydrogen results (Antognini *et al.*, 2013a; Pohl *et al.*, 2010). Some of these analyses obtain results consistent with the precise values from muonic hydrogen, while others are in agreement with larger values of r_{Ep}. Below we describe some of these analyses.

Hill and Paz (Hill and Paz, 2010) carried out a model-independent determination of the proton charge radius from electron scattering by first performing a conformal mapping of the domain of analyticity onto the unit circle in terms of $z(t, t_{cut}, t_0)$ defined in Eq. (54), where $t = q^2$, $t_{cut} = 4m_\pi^2$, and t_0 is a free parameter mapping onto $z = 0$. The form factor $G_E(q^2)$ can then be written as a function of z, where a z expansion can be carried out with the advantage that higher-order terms in z are suppressed. Using electron-proton scattering data sets, a proton charge radius value of $\langle r_{Ep}^2\rangle^{1/2} = 0.870 \pm 0.023 \pm 0.012$ fm is obtained (see Ref. (Hill and Paz, 2010) for details).

Lorenz, Hammer and Meissner (Lorenz and Meissner, 2012) analyzed the 2010 Mainz data using a dispersive approach to ensure analyticity and unitarity in the description of the nucleon form factors. In their analysis they have included the world data on the proton and also the neutron, obtaining a charge radius value of $\langle r_{Ep}^2\rangle^{1/2} = 0.84 \pm 0.01$ fm, consistent with the result from muonic hydrogen. Lorenz and Meissner (Lorenz, 2014) later also reanalyzed the Mainz data using a fit function based on conformal mapping, and showed that the extracted value for the proton charge radius – with a larger statistical uncertainty than that from (Bernauer *et al.*, 2010) – is in agreement with the value from muonic hydrogen spectroscopic measurements, and also their previous dispersive analysis. Lorenz *et al.* (Lorenz *et al.*, 2015) calculated the TPE corrections to the electron-proton scattering, and applied these corrections to the Mainz data (Bernauer *et al.*, 2010). They also investigated the impact on the extraction of the proton form factors from the inclusion of physical constraints and the extraction of $\langle r_{Ep}^2\rangle^{1/2}$ due to the enforcement of a realistic spectral function, which dominates the latter. Very recently, a further improvement of the dispersive description has been presented in (Lin *et al.*, 2021) using an improved two-pion continuum based on a Roy-Steiner analysis of pion-nucleon scattering (Hoferichter *et al.*, 2016a,b), resulting in a value $\langle r_{Ep}^2\rangle^{1/2} = 0.838 \pm 0.005 \pm 0.004$ fm, where the first error is due to the fitting procedure and the second is from the spectral function.

Adamuscin *et al.* (Adamuscin *et al.*, 2012) analyzed all nucleon electromagnetic form factor data using their unitary and analytic ten-resonance model of the nucleon electromagnetic structure in order to find the corresponding behavior of the proton electric form factor in the extended space-like region. The non-dipole behavior of G_{Ep} is found to have a zero around $Q^2 = 13$ (GeV/c)^2. The extracted proton radius from this global analysis is $\langle r_{Ep}^2\rangle^{1/2} = 0.84894 \pm 0.0069$ fm.

The first analysis of the electron-proton elastic scattering data based on Bayesian statistical methods was carried out by Graczyk and Juszczak (Graczyk and Juszczak, 2014) and the most probable proton charge radius value was found to be $\langle r_{Ep}^2\rangle^{1/2} = 0.899 \pm 0.003$ fm. This analysis was done by accounting for the TPE effect using a box diagram model, including nucleon and $\Delta(1232)$ states.

The effect of TPE corrections in extracting the proton charge radius has also been studied in an earlier analysis of the electron-proton scattering data (Borisyuk, 2010). Using a dispersive formalism for the TPE for the nucleon elastic contribution, Borisyuk (Borisyuk, 2010) reported a value $\langle r_{Ep}^2\rangle^{1/2} = 0.912 \pm 0.009(\text{stat}) \pm 0.007(\text{syst})$ fm.

Lee, Arrington and Hill carried out a comprehensive global analysis (Lee *et al.*, 2015) of the world electron-proton elastic scattering data with a focus on the Mainz measurements (Bernauer *et al.*, 2010). This study involves enforcing model-independent constraints from form factor analyticity, and systematic studies of possible systematic effects. The extracted proton radius from this improved analysis of the Mainz data is $\langle r_{Ep}^2\rangle^{1/2} = 0.895(20)$ fm, while $\langle r_{Ep}^2\rangle^{1/2} = 0.916(24)$ fm from analyzing the world data without including the Mainz data. Arrington and Sick (Arrington, 2015) carried out a global examination of the elastic electron-proton scattering data and recommended a proton charge radius value of 0.879(11) fm.

Griffioen, Carlson and Maddox (Griffioen and Maddox, 2016) analyzed the Mainz data set (Bernauer *et al.*, 2010) using a continued fraction functional form to map the G_E assuming it is monotonically falling and inflectionless. They obtained a proton charge radius value of 0.840(16) fm, consistent with the mounic hydrogen result after rescaling different data sets on a level that is smaller than the original normalization uncertainties, and also inflating the point-to-point systematic uncertainty by 15%.

A proton charge radius value consistent with muonic hydrogen results was also obtained by Higinbotham *et al.* (Higinbotham *et al.*, 2016) from analyzing data in the low momentum transfer region from Mainz in the 1980s (Simon *et al.*, 1980) and Saskatoon in 1974 (Murphy *et al.*, 1974a,c) using a stepwise regression of Maclaurin series and applying the F-test and the Akaike information criterion. Including the Mainz results on G_{Ep} (Bernauer *et al.*, 2014), the same analysis favors a radius that is consistent with the muonic hydrogen results, though their result is more sensitive to the range of the data included in the analysis.

Horbatsch and Hessels (Horbatsch and Hessels, 2016a) also analyzed the Mainz data (Bernauer *et al.*, 2010) and obtained $\langle r_{Ep}^2\rangle^{1/2}$ values ranging at least from 0.84 to 0.89 fm using two single-parameter form factor models with one being a dipole form, and the other a linear fit to a conformal-mapping variable.

Sick and Trautmann (Sick and Trautmann, 2017) argued that the smaller values of $\langle r_{Ep}^2\rangle^{1/2}$ from (Griffioen and Maddox, 2016; Higinbotham *et al.*, 2016; Horbatsch and Hessels, 2016a) are due to the neglect of higher moments in these analyses. Kraus *et al.* (Kraus *et al.*, 2014) found that fits of the proton charge form factor with truncated polynomials give too small values for the proton charge radius. In a later paper by Horbatsch *et al.* (Horbatsch *et al.*, 2017), a $\langle r_{Ep}^2\rangle^{1/2}$ value of 0.855(11) fm was obtained with the higher moments fixed to the values based on Chiral Perturbation theory.

Alarcón, Higinbotham, Weiss, and Ye (Alarcón *et al.*, 2019) used a new theoretical frame work that combines chiral effective field theory and dispersion analysis. The behavior of the spacelike form factor in the finite Q^2 region correlates with its derivative at $Q^2 = 0$ due to the analyticity in the momentum transfer. In this approach, predictions for spacelike form factors are made with the proton charge radius as a free parameter. By comparing the predictions for different values of the proton radius with a descriptive global fit (Lee *et al.*, 2015) of the spacelike form factor data, the authors of (Alarcón *et al.*, 2019) extracted a proton radius value of 0.844(7) fm, that is consistent with the muonic hydrogen results. A more recent analysis by Alarcón, Higinbotham, and Weiss (Alarcón *et al.*, 2020) using the aforementioned method to extract both the proton magnetic and charge radius from the Mainz A1 data (Bernauer *et al.*, 2010), obtained $\langle r_{Mp}^2\rangle^{1/2} = 0.850 \pm 0.001(\text{fit } 68\%) \pm 0.010$ (theory full range) fm, and $\langle r_{Ep}^2\rangle^{1/2} = 0.842 \pm 0.002$ (fit) $\pm$ 0.010 (theory) fm. Including the PRad data (Xiong *et al.*, 2019) into their fit, they found no change in the extracted radius values within uncertainties.

Sick (Sick, 2018) carried out a detailed study to reduce the model dependence associated with the required extrapolation in determining $\frac{dG_E}{dQ^2}(Q^2 = 0)$ to extract $\langle r_{Ep}^2\rangle^{1/2}$. The approach takes into account the fact that G_{Ep} in regions of lower than experimentally measured momentum transfer values is closely related to the charge density $\rho(r)$ at large values of r, which is constrained using form factor data at finite values of Q^2, reducing model dependence in extrapolation. While corrections for relativistic effects are applied in this analysis, it is however not possible to rigorously define an accurate 3-dimensional charge density for the proton as has been discussed above. Using different form factor parameterizations of the data prior to 2010, Sick obtains a $\langle r_{Ep}^2\rangle^{1/2}$ value of 0.887(12) fm, that is consistent with the Mainz result (Bernauer *et al.*, 2010), but inconsistent with the muonic hydrogen results (Antognini *et al.*, 2013a; Pohl *et al.*, 2010).

Zhou *et al.* (Zhou *et al.*, 2019) adopted a flexible approach within a Bayesian paradigm which does not make any parametric assumptions for G_{Ep}, but with two physical constraints – a normalization constraint for $G_{Ep}(0)$, and G_{Ep} being monotonically decreasing as Q^2 increases. The value of the proton charge radius extracted from the Mainz data is found to be sensitive to the Q^2 range of the data used in this analysis.

Horbatsch (Horbatsch, 2020) analyzed the PRad data on the proton G_E following a proposal by Hagelstein and Pascalutsa (Hagelstein and Pascalutsa, 2019) by taking the logarithm to yield a Q^2 dependent radius function. This analysis shows that the PRad data is in agreement with theoretical predictions from dispersively improved chiral perturbation theory.

Atac *et al.* (Atac *et al.*, 2021) extracted both the proton and the neutron charge radius from a global analysis of the world proton and neutron form factor data by carrying out a flavor separation of the Dirac form factor F_1 assuming isospin symmetry. The u- and d-quark root-mean-squared transverse radii are subsequently determined from a fit to the slope of the corresponding flavor-dependent Dirac form factors, from which both the proton and the neutron charge radii are reconstructed. In this analysis, a proton charge radius value of $0.852 \pm 0.002_{(stat.)} \pm 0.009_{(syst.)}$ fm is obtained, which is consistent with the muonic hydrogen results as well as the latest result from the PRad experiment (Xiong *et al.*, 2019). Excluding the PRad data, a $\langle r_{Ep}^2\rangle^{1/2}$ value of 0.857(13) fm is extracted, consistent with the value including the PRad data but with a larger uncertainty.

Borisyuk and Kobushkin (Borisyuk and Kobushkin, 2020) reanalyzed the Mainz data (Bernauer *et al.*, 2010) and found that the radius value obtained under certain conditions can be consistent with the muonic hydrogen results.

Cui *et al.* (Cui *et al.*, 2021) extracted values of $\langle r_{Ep}^2\rangle^{1/2}$ using the electron-proton scattering data from the PRad experiment at JLab (Xiong *et al.*, 2019) and the A1 experiment at Mainz (Bernauer *et al.*, 2010) using a statistical sampling approach based on the Schlessinger Point Method (SPM). The SPM method, with an important feature that no specific functional form is assumed for the interpolation, is used in this analysis for the interpolation and extrapolation of smooth functions to minimize biases associated with assumed forms. The authors obtained a radius value of $\langle r_{Ep}^2\rangle^{1/2} = 0.838 \pm 0.005_{\text{stat}}$ fm from the PRad experiment, and a value of $\langle r_{Ep}^2\rangle^{1/2} = 0.856 \pm 0.014_{\text{stat}}$ fm from the Mainz A1 experiment including data up to a Q^2 value of 0.014 (GeV/c)^2. Combining these two values, Cui *et al.* finds a proton charge radius value of

$$\langle r_{Ep}^2 \rangle^{1/2} = 0.847 \pm 0.008_{\rm stat}\ {\rm fm}, \tag{73}$$

from the two most recent experiments (Bernauer *et al.*, 2010; Xiong *et al.*, 2019) measuring the unpolarized electron-proton elastic scattering cross sections, that is consistent with the muonic hydrogen results (Antognini *et al.*, 2013a; Pohl *et al.*, 2010), as well as the most recent ordinary hydrogen spectroscopy results (Bezginov *et al.*, 2019; Grinin *et al.*, 2020) for the proton charge radius.

Most recently, Gramolin and Russell (Gramolin and Russell, 2021) analyzed the entire Mainz data set (Bernauer *et al.*, 2010) using the two-dimensional Fourier transform of the Dirac form factor $F_1(Q^2)$, i.e., the proton transverse charge density discussed in Section III.C. The proton charge radius is related to the second moment of this transverse charge density. With this approach, they obtained a radius value $\langle r_{Ep}^2 \rangle^{1/2} = 0.889(5)_{\rm stat}(5)_{\rm syst}(4)_{\rm model}$ fm, that is consistent with the original Mainz result (Bernauer *et al.*, 2010).

Fig. 19 shows proton charge radius results from electron-proton scattering experiments since 2010 and the extracted $\langle r_{Ep}^2 \rangle^{1/2}$ values from some of the various analyses described above. Also included are the muonic hydrogen results as well as the CODATA-2014 recommended value. While the results of some of these analyses are consistent with muonic hydrogen results on the $\langle r_{Ep}^2 \rangle^{1/2}$, others are consistent with the CODATA-2014 recommended value based on electron scattering data, and few are in between. There is no conclusive statement one can draw regarding the proton charge radius puzzle from these analyses of electron-proton scattering data. New and further improved measurements from lepton scattering are highly desirable, which we describe in Section VII.

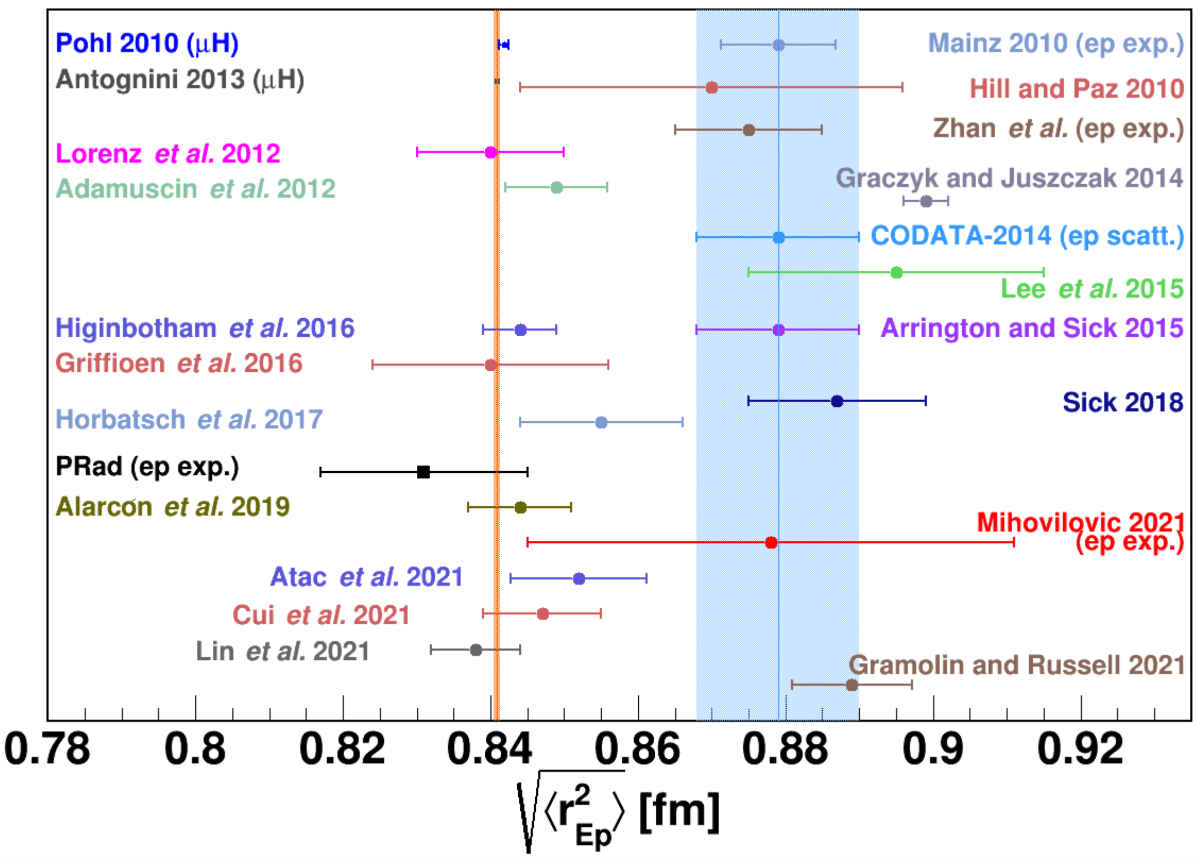

FIG. 19 (Color online) The proton charge radius values determined from electron scattering experiments since 2010 together with the results from the various analyses of electron-proton scattering data (see text) (figure credit: Jingyi Zhou).

VI. MODERN SPECTROSCOPIC MEASUREMENTS

A. Muonic hydrogen spectroscopic experiments

The first determination of the proton charge radius using muonic hydrogen atoms was carried out by Pohl *et al.* (Pohl *et al.*, 2010) at the Paul Scherrer Institute (PSI) by measuring the transition frequency between the

$2S_{1/2}^{F=1}$ and the $2P_{3/2}^{F=2}$ states at wavelengths around 6.01 μm using pulsed laser spectroscopy, see Fig. 20. The muonic hydrogen atoms were produced by stopping negative muons in a hydrogen gas target with a pressure of 1 hPa (1 mbar) at the πE5 beam-line of the proton accelerator at PSI. The muonic atoms produced are in the $n \approx 14$ excited state, which then decay with about 1% probability to the $2S$ metastable state, while the majority (99%) decay to the $1S$ ground state. The lifetime of the long-lived $2S$ state at 1 hPa pressure is 1 μs. A 5-ns pulsed laser with a wavelength tunable around 6 μm is incident upon and illuminates the target volume about 0.9 μs after the muons reach the target. The laser wavelength is scanned through the resonance of the $2S \to 2P$ transition. Upon the excitation, the $2P$ state with a lifetime of 8.5 ps will decay to the $1S$ state via emission of the 1.9-keVK_α x-ray. Therefore, in this pulsed muonic atom laser spectroscopic measurement, the resonance curve is recorded by the coincidence of the 1.9-keV x-ray and the laser pulse as a function of the laser wavelength. A coincidence time window of 0.9 to 0.975 μs is chosen, i.e. 0.9 μs after the muons enter the H_2 target, and the 75-ns window corresponds to the confinement time of the laser light within the optics surrounding the target.

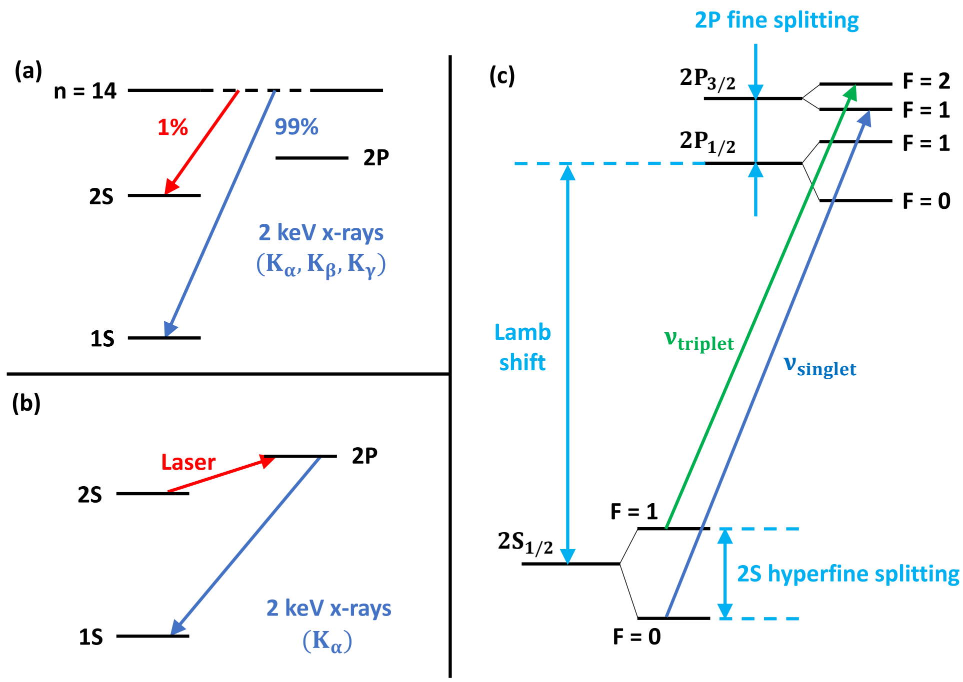

FIG. 20 (Color online) The muonic hydrogen energy levels relevant to the proton charge radius measurement (figure credit: Jingyi Zhou).

The resonance frequency for the transition between the $2S_{1/2}^{F=1}$ and the $2P_{3/2}^{F=2}$ states was measured to be 49881.88 (76) GHz (Pohl *et al.*, 2010), which gave a proton charge radius value of $\langle r_{Ep}^2 \rangle^{1/2} = 0.84184(67)$ fm based on the state-of-the-art QED calculations. In a follow-up paper by the CREMA collaboration (Antognini *et al.*, 2013a), the tunable laser wavelength was scanned from 5.5 to 6.0 μm, and in addition to the original transition between the $2S_{1/2}^{F=1}$ (triplet) and the $2P_{3/2}^{F=2}$ states, a second transition between $2S_{1/2}^{F=0}$ (singlet) and the $2P_{3/2}^{F=1}$ states was also measured. The corresponding resonance frequencies were determined to be

$$\nu_t = 49881.35\,(57)_{\rm stat.}(30)_{\rm syst.}\ \text{GHz},$$
$$\nu_s = 54611.16\,(1.00)_{\rm stat.}(30)_{\rm syst.}\ \text{GHz}.$$

From these two transitions, the Lamb shift (LS) and the hyperfine splitting (HFS) can be independently determined and they are:

$$\Delta E_{LS}^{exp} = 202.3706\,(23)\ \text{meV}, \qquad (74)$$
$$\Delta E_{HFS}^{exp} = 22.8089\,(51)\ \text{meV}.$$

Relating the state-of-the-art theory calculations of the Lamb shift (Borie, 2012; Eides, 2001; Jentschura, 2011;

Karshenboim, 2010; Karshenboim *et al.*, 2012; Pachucki, 1996, 1999) to the proton $\langle r_{Ep}^2\rangle$, one obtains (in meV):

$$\Delta E_{LS}^{th}(2P-2S) = 206.0336\,(15) \\ -\,5.2275\,(10)\,\langle r_{Ep}^2\rangle + \Delta E_{TPE}, \quad (75)$$

where the last term is due to the two-photon-exchange proton polarizability contribution discussed in Section IV. Using the estimate of Eq. (71) for the latter, the extracted value for the proton charge radius is:

$$\langle r_{Ep}^2\rangle^{1/2} = 0.84087(26)_{\rm exp}(29)_{\rm th}\ {\rm fm} = 0.84087(39)\ {\rm fm}. \quad (76)$$

This result is not only consistent with the earlier result from the muonic hydrogen spectroscopic measurement (Pohl *et al.*, 2010), but also represents the most precise value for the proton charge radius. Both these results have been included in the 2018 CODATA compilation (Tiesinga *et al.*, 2021) and dominate its recommended value for the proton charge radius.

One notices from Eq. (71) that the uncertainty (δ) of the present TPE estimate for the muonic hydrogen $2P-2S$ Lamb shift, $\delta(\Delta E_{TPE}) = 2.0\ \mu$eV, is comparable to the present experimental Lamb shift precision, $\delta(\Delta E_{LS}^{exp}) = 2.3\ \mu$eV, see Eq. (74). A further improvement on the proton charge radius extraction from muonic hydrogen spectroscopy results therefore hinges upon further improving the TPE estimates.

B. Ordinary Hydrogen spectroscopic experiments

Since the release of the first muonic hydrogen spectroscopic determination of the proton charge radius (Pohl *et al.*, 2010), there have been four atomic hydrogen spectroscopic measurements of the proton charge radius (Beyer *et al.*, 2017; Bezginov *et al.*, 2019; Fleurbaey *et al.*, 2018; Grinin *et al.*, 2020) with Bezginov *et al.* (Bezginov *et al.*, 2019) being a direct measurement of the hydrogen Lamb shift.

Beyer *et al.* (Beyer *et al.*, 2017) carried out a measurement of the $2S-4P$ transition of ordinary hydrogen atoms using a cryogenic beam of H atoms. A major improvement over previous experiments in overcoming the limitation due to the electron-impact excitation used to produce atoms in the metastable $2S$ state is the use of the Garching $1S-2S$ apparatus (Matveev *et al.*, 2013; Parthey *et al.*, 2011) as a well-controlled cryogenic source of 5.8-K cold $2S$ atoms. In this case, the $2S_{1/2}^{F=0}$ sublevel is almost exclusively populated via Doppler-free two-photon excitation without imparting additional momentum on the atoms. The line shifts due to quantum interference of neighboring atomic resonances, and the first-order Doppler shift are the two remaining major systematic issues of this experiment. In (Beyer *et al.*, 2017), apart from the use of a cryogenic H source which reduces the thermal velocity of atoms by a factor of 10 compared with prior experiments, the employment of a specifically developed active fiber-based retroreflector (Beyer *et al.*, 2016) allows for a high level of compensation of the first-order Doppler shift – 4 parts in 10^6 of the full collinear shift. To suppress the quantum interference effect in order to determine the absolute $2S-4P$ transition frequency, the experiment was designed to observe line shifts due to the quantum interference effect and to simulate the line shifts fully using an atomic line shape model. Finally the quantum interference effect is removed using the Fano-Voigt line shape to obtain the unperturbed transition frequency for both the $2S_{1/2}^{F=0} - 4P_{1/2}^{F=1}$ and the $2S_{1/2}^{F=0} - 4P_{3/2}^{F=1}$ transitions. Combining with previous precision measurements of the $1S-2S$ transition by the same group (Matveev *et al.*, 2013; Parthey *et al.*, 2011), values for both the Rydberg constant and the proton charge radius were determined to be (Beyer *et al.*, 2017):

$$R_\infty = 10\,973\,731.568\,076(96)\ {\rm m}^{-1}, \\ \langle r_{Ep}^2\rangle^{1/2} = 0.8335(95)\ {\rm fm}.$$

The uncertainty on the proton charge radius from this single experiment is comparable to the prior aggregate atomic hydrogen world data. This result is consistent with the muonic hydrogen results on the proton charge radius, but 3.3 combined standard deviations smaller than the 2014 CODATA recommended value (Mohr *et al.*, 2016) based on previous world data from ordinary hydrogen.

Fleurbaey *et al.* (Fleurbaey *et al.*, 2018) in Paris reported a result on the proton charge radius and the Rydberg constant in 2018 by combining their measurement of the $1S-3S$ transition from ordinary atomic hydrogen with the $1S-2S$ transition measurement performed by the Garching group (Parthey *et al.*, 2011). The Paris experiment measured the $1S-3S$ two-photon hydrogen transition frequency using a continuous-wave laser with a wavelength of 205 nm and through the Balmer-α $3S-2P$ fluorescence detection. A room temperature atomic hydrogen beam was used in the experiment and the main systematic effect of the experiment is the second-order Doppler effect due to the room-temperature atomic velocity distribution. The results presented included data taken during two different periods (2013 and 2016-2017) with improvements taking place between the two periods. The reported results are (Fleurbaey *et al.*, 2018):

$$R_\infty = 10\,973\,731.568\,53(14)\ {\rm m}^{-1}, \\ \langle r_{Ep}^2\rangle^{1/2} = 0.877(13)\ {\rm fm}.$$

While the extracted r_{Ep} value is consistent with the CODATA-2014 (Mohr *et al.*, 2016) recommended value, it disagrees with the muonic hydrogen Lamb shift result (Antognini *et al.*, 2013a) by 2.6 standard deviations. This experiment and the aforementioned experiment (Beyer *et al.*, 2017) used a similar measurement technique in which two transition frequencies are involved. Each transition is between two ordinary hydrogen energy levels, corresponding to two different principal quantum numbers n_1 and n_2 with at least one of them being a S state. We note that both the Rydberg constant and the proton charge radius determined from the Paris experiment (Fleurbaey *et al.*, 2018) disagree with those from the Garching experiment (Beyer *et al.*, 2017) at a level of about 2 standard deviations. It will be important to resolve such a discrepancy especially by repeating the same transition, either the $1S-3S$ or the $2S-4P$ transition.

To determine the proton charge radius from ordinary hydrogen spectroscopic measurements, one can also measure the Lamb shift (the $2S_{1/2}{-}2P_{1/2}$ transition) directly, in which case, the principal quantum numbers for the two states between the transition are the same, and as such the precision of the Rydberg constant from other experiments is sufficient and the Lamb shift measurement itself together with the state-of-the-art QED calculation is used to extract $\langle r^2_{Ep}\rangle^{1/2}$. The most recent r_{Ep} determination (Bezginov *et al.*, 2019) from ordinary atomic hydrogen spectroscopy is such a measurement. In the experiment by Bezginov *et al.* (Bezginov *et al.*, 2019), a fast beam of hydrogen atoms was created by passing protons – which were accelerated to 55 keV – through a molecular hydrogen target chamber. About half of the protons were neutralized into hydrogen atoms from collisions with the molecules, and about 4% were created in the metastable $2S$ state. The experiment used two different radio frequency cavities to drive the $2S$ state away from the $F=1$ substates so that only the $F=0$ substate survives. The transition between the $2S_{1/2}(F=0)\rightarrow 2P_{1/2}(F=1)$ is the Lamb shift measured in this experiment using the experimental technique of frequency-offset separated oscillatory field (Kato *et al.*, 2018; Vutha and Hessels, 2015), which is a modified Ramsey technique of separated oscillatory fields (Ramsey, 1949). The measured transition frequency of $2S_{1/2}(F=0)\rightarrow 2P_{1/2}(F=1)$ from this experiment is 909.8717(32) MHz. The Lamb shift determined is 1057.8298(32) MHz after including the contribution from hyperfine structure, which is 147.9581 MHz (Horbatsch and Hessels, 2016b). The proton charge radius value deduced from this experiment is (Bezginov *et al.*, 2019):

$$\langle r^2_{Ep}\rangle^{1/2} = 0.833(10)\text{ fm}, \tag{77}$$

which is consistent with the muonic hydrogen Lamb shift measurements (Antognini *et al.*, 2013a; Pohl *et al.*, 2010), the 2017 ordinary hydrogen measurement (Beyer *et al.*, 2017), and the PRad result from electron scattering (Xiong *et al.*, 2019). It disagrees however with the Paris measurement (Fleurbaey *et al.*, 2018) at a level of about two standard deviations.

Most recently, a new result on $\langle r^2_{Ep}\rangle^{1/2}$ from ordinary hydrogen spectroscopy has been published (Grinin *et al.*, 2020). This experiment measured the same $1S-3S$ transition as that of (Fleurbaey *et al.*, 2018) but with significantly improved precision. Major improvements in reducing systematic uncertainties have been achieved by using a cold atomic beam and a two-photon direct frequency comb technique. The experiment also achieved an almost shot noise limited statistical uncertainty of 110 Hz. The unperturbed frequency for the $1S(F=1)-3S(F=1)$ transition determined from this experiment is 2,922,742,936,716.72(72) kHz, and $f_{1S-3S}(\text{centroid}) = 2,922,743,278,665.79(72)$ KHz after subtracting the hyperfine shifts. Combing this new result on the $1S-3S$ transition with the $1S-2S$ transition frequency measured by the same group (Matveev *et al.*, 2013) before, Grinin *et al.* obtained (Grinin *et al.*, 2020):

$$\begin{aligned} R_\infty &= 10\,973\,731.568\,226(38)\text{ m}^{-1}, \\ \langle r^2_{Ep}\rangle^{1/2} &= 0.8482(38)\text{ fm}. \end{aligned}$$

This extracted Rydberg constant is in agreement with the latest CODATA-2018 (Tiesinga *et al.*, 2021) recommended value. The new proton charge radius result from (Grinin *et al.*, 2020) is more than a factor of two more precise but also 2.9 standard deviations smaller compared with the CODATA-2014 recommended value from ordinary hydrogen spectroscopic measurements. It is more than a factor of three more precise, but 2.1 standard deviations smaller than the Paris result (Fleurbaey *et al.*, 2018). Compared with muonic hydrogen results on $\langle r^2_{Ep}\rangle^{1/2}$, this new result from the $1S-3S$ transition is about two standard deviations larger. Fig. 21 shows the results on $\langle r^2_{Ep}\rangle^{1/2}$ from these four latest spectroscopic measurements using ordinary hydrogen atoms (Beyer *et al.*, 2017; Bezginov *et al.*, 2019; Fleurbaey *et al.*, 2018; Grinin *et al.*, 2020) together with the muonic hydrogen results (Antognini *et al.*, 2013a; Pohl *et al.*, 2010). Also shown is the CODATA-2014 (Mohr *et al.*, 2016) recommended value based on ordinary hydrogen spectroscopy. While major progress has been made in recent years, and most of these recent measurements of the proton charge radius support a smaller value including the PRad result (Xiong *et al.*, 2019), the comparison of $\langle r^2_{Ep}\rangle^{1/2}$ extractions between electronic versus muonic systems is not fully settled. This situation highlights the importance of future high-precision scattering experiments, to improve on the result obtained by PRad. It is also highly desirable to have future spectroscopic measurements from ordinary hydrogen to achieve a comparable precision, i.e., a relative precision of 0.5% or better. The PRad-II and other ongoing and upcoming scattering experiments will be discussed in the following section.

Table IV provides a summary of the aforementioned spectroscopic measurements using both muonic and ordinary hydrogen published since 2010.

Experiment	Type	Transition(s)	$\sqrt{< r_{Ep}^2 >}$ (fm)	r_∞ (m^{-1})
Pohl 2010	μH	$2S_{1/2}^{F=1} - 2P_{3/2}^{F=2}$	0.84184(67)	
Antognini 2013	μH	$2S_{1/2}^{F=1} - 2P_{3/2}^{F=2}$	0.84087(39)	
		$2S_{1/2}^{F=0} - 2P_{3/2}^{F=1}$		
Beyer 2017	H	$2S - 4P$	0.8335(95)	10 973 731.568 076 (96)
		with $(1S - 2S)$		
Fleurbaey 2018	H	$1S - 3S$	0.877(13)	10 973 731.568 53(14)
		with $(1S - 2S)$		
Bezginov 2019	H	$2S_{1/2} - 2P_{1/2}$	0.833(10)	
Grinin 2020	H	$1S - 3S$	0.8482(38)	10 973 731.568 226(38)
		with $(1S - 2S)$		

TABLE IV Summary of proton charge radius results from muonic and ordinary hydrogen spectroscopic measurements published since 2010.

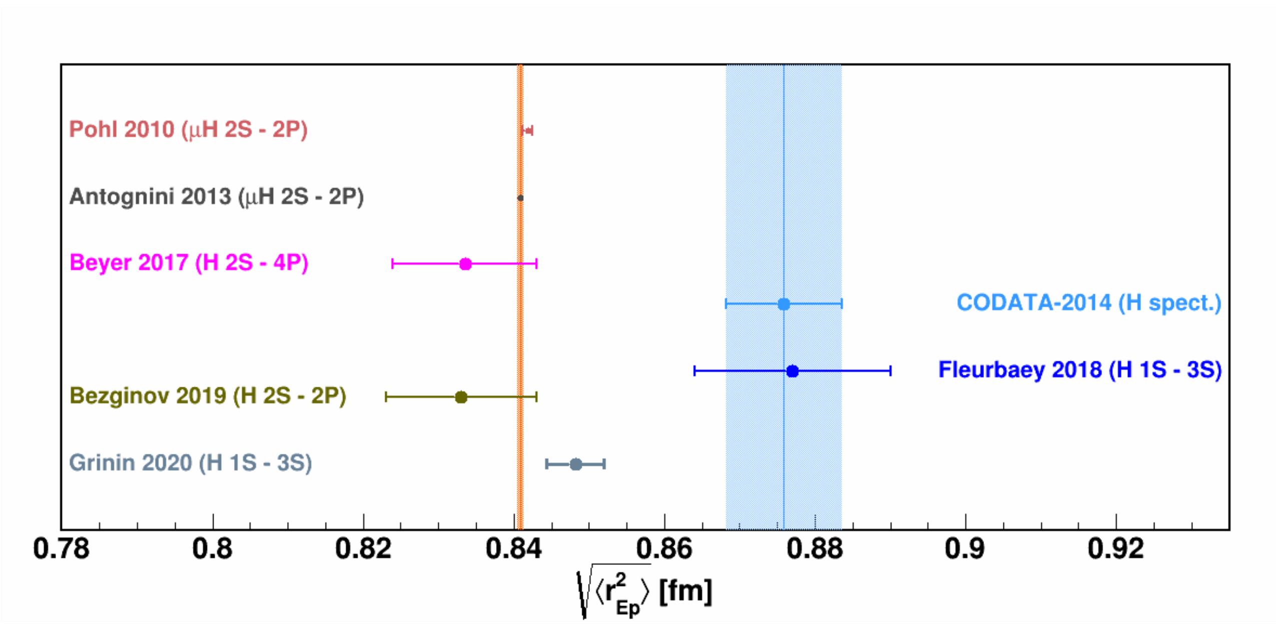

FIG. 21 (Color online) The latest proton charge radius results from ordinary hydrogen spectroscopic measurements together with muonic hydrogen results and the CODATA-2014 recommended value based on ordinary hydrogen spectroscopy (figure credit: Jingyi Zhou).

VII. ONGOING AND UPCOMING EXPERIMENTS

In this section we aim to briefly describe the current and planned experiments aimed at extracting the proton charge radius. Some of these plans have also been discussed in a recent review by Karr, Marchand, and Voutier (Karr and Voutier, 2020).

A. The MUSE experiment at PSI

The muonic hydrogen spectroscopic results on the proton charge radius (Antognini *et al.*, 2013a; Pohl *et al.*, 2010) also motivated lepton-proton scattering measurements with muon beams. The MUon proton Scattering Experiment (MUSE) (Gilman *et al.*, 2013, 2017) at PSI is currently ongoing, in which measurements of lepton-proton elastic scattering cross sections utilizing both the μ^+ and μ^- (muon) beams will be compared to those performed with electron and positron beams. The MUSE experiment uses the PSI $\pi M1$ beam line with $e^\pm$, and $\mu^\pm$ beams at incident momentum values of 115, 153 and 210 MeV/c to allow for simultaneous measurements of the $\mu^\pm p$ and $e^\pm p$ elastic scattering cross sections. The coverage of the scattering angle for the MUSE experiment is 20-100°, corresponding to a Q^2 range of 0.0016 (with 115

MeV/c beam momentum) to 0.08 (GeV/c)^2 (210 MeV/c incident beam momentum). Due to the mass difference of $e^{\pm}$, and $\mu^{\pm}$, there is a small difference in the Q^2 coverage between the two. The lowest Q^2 value reached by MUSE is comparable to that of the Mainz experiment (Bernauer *et al.*, 2010), but much higher than that of the PRad experiment (Xiong *et al.*, 2019), 0.0002 (GeV/c)^2. In addition to the μ and e beam particles, there are also pions in the $\pi M1$ mixed beam. Therefore, beam-line detectors for identifying various beam particles, determining the beam particle momentum and trajectories into the target, and counting the beam particles are important for the MUSE experiment. The beam-line detectors include a beam hodoscope (fast scintillator array) measuring times relative to the accelerator RF to identify beam particle type, GEM detectors, a veto scintillator, a beam monitor and a calorimeter. A liquid hydrogen target is the main target for the production data taking with two symmetric spectrometers each equipped with detectors consisting of two scattered particle scintillator (SPS) paddles and two straw-tube trackers (STT). A schematic setup of the MUSE experiment is shown in Fig. 22. The uncertainties from the MUSE experiment in the proton charge radius separately determined with μ^+p, μ^-p, e^+p, and e^-p are expected to be nearly the same, around 0.01 fm. In addition to the determination of the proton charge radius, the MUSE experiment will allow for tests of the two-photon-exchange effect in lepton scattering by comparing the $\mu^{\pm}p$ and $e^{\pm}p$ cross section, and a direct test of lepton universality. More details about the MUSE experiment can be found in (Cline *et al.*, 2021). The MUSE collaboration is working towards commissioning the entire experiment with production data taking expected to start in the fall of 2021.

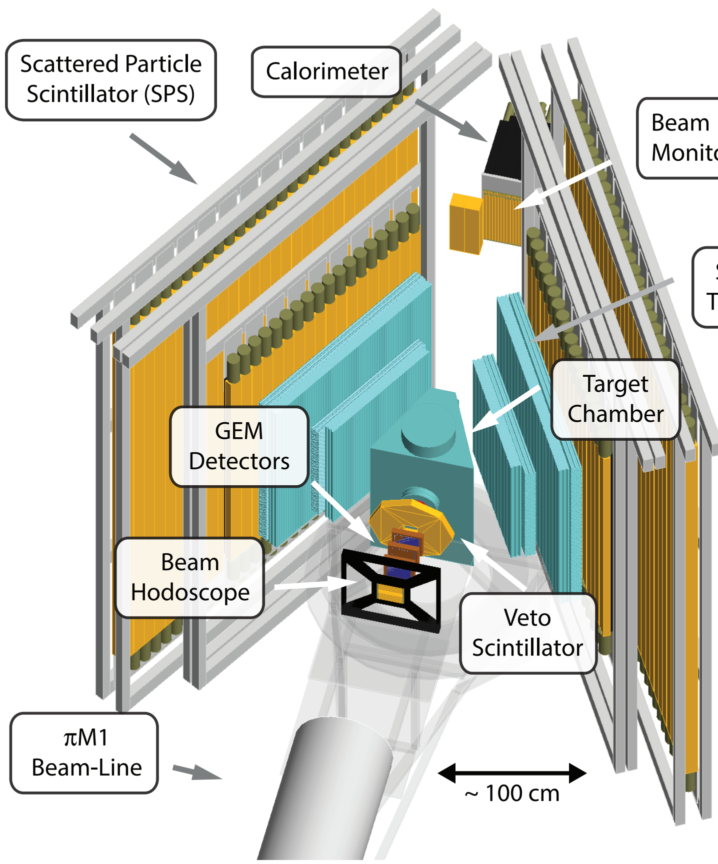

FIG. 22 (Color online) The schematic of the MUSE experiment at PSI (figure credit: Steffen Strauch).

B. The AMBER Experiment at CERN

The COMPASS collaboration proposed a precision measurement of elastic μp scattering at high energy and low Q^2 with the M2 beam-line at CERN with AMBER (Dreisbach *et al.*, 2019). By carrying out muon-proton scattering at high energies – compared with low-energy lepton-proton scattering – the proposed experiment has different, and in some cases favorable systematics. The AMBER measurement of the proton radius will use 100 GeV muons of the CERN M2 beam-line. The hydrogen target will be an active target – a high-pressure time projection chamber (TPC) – in which the recoil protons will be measured for proton energies of 0.5 to 20 MeV. For small-angle scattered muon detection, silicon detectors will be used for precision tracking. The triggers will be formed by scattered muons using the 200 μm SciFi stations, and the inner tracking and the ECAL of the COMPASS spectrometer will be used for measuring the scattered muons. The proposed experiment with 200 days of beam time will extract the proton electric form factor in a Q^2 range of 0.001 to 0.04 (GeV/c)^2 with relative point-to-point precision better than 0.001. The projected precision in the determination of the proton charge radius is expected to be better than 0.01 fm. The experiment has been approved to run at CERN in the coming years. Fig. 23 shows the schematics of the AMBER setup for the proton charge radius measurement (top) including the time-projection chamber, scintillating-fiber hodoscope, and the silicon-pixel detectors. The entire setup in the AMBER spectrometer with relevant parts shown is illustrated in the bottom part of Fig. 23.

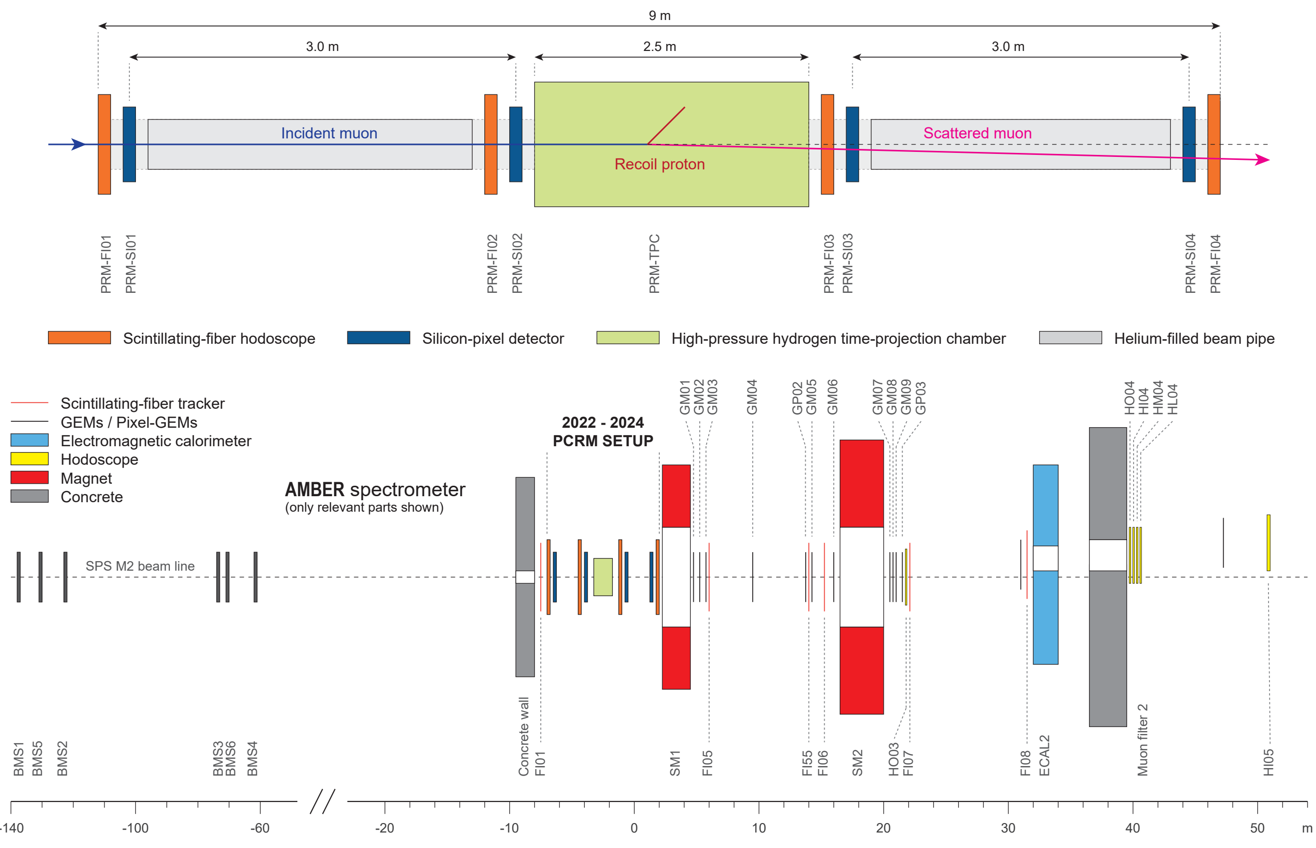

FIG. 23 (Color online) Top: schematics of the AMBER setup for the proton charge radius measurement. Bottom: the entire setup in the AMBER spectrometer with relevant parts shown (figure credit: AMBER Collaboration).

C. The PRad-II experiment at Jefferson Lab

Following the PRad experiment (Xiong *et al.*, 2019), the PRad collaboration proposed a new and upgraded experiment, PRad-II (Gasparian *et al.*, 2020; Jefferson Lab Proposal PR12-20-004, Spokespersons: D. Dutta, H. Gao, A. Gasparian (contact), K. Gnanvo, D. Higinbotham, N. Liyanage, E. Pasyuk, and C. Peng, 2020) to the Jefferson Lab program advisory committee (PAC). Leading the next generation of the proton charge radius measurements, PRad-II will use an electromagnetic calorimeter together with two planes of tracking detectors with several major upgrades and improvements over the PRad experiment. The experiment has been approved by the PAC with the highest scientific rating.

One important aspect of PRad-II compared with PRad is to reduce the statistical uncertainty of the electron-proton elastic scattering cross section measurement by a factor of 4. Furthermore, a number of upgrades will improve the precision in determining the proton electric form factor and the charge radius significantly by reducing systematic uncertainties. The upgrades include (i) adding a second tracking detector plane for improving the tracking capability and further suppressing the beam-line related background; (ii) upgrading the HyCal by replacing its outer-region lead glass modules with $PbWO_4$ crystals to improve the detector resolutions and uniformity and to suppress the inelastic contamination; (iii) adding a set of cross-shaped scintillator detectors in order to detect scattered electrons from *ep* at scattering angles as forward as 0.5° while still being cleanly separated from *ee* scattering; (iv) upgrading the HyCal readout to flash ADC to enhance the data taking rate; (v) adding a second beam halo blocker together with improved beam-line vacuum to further suppress the background; (vi) and future improved radiative correction calculations at the next-to-next-to-leading order (NNLO) for both *ep* and *ee* scattering. These upgrades and improvements will lead to the reduction of the overall experimental uncertainty in the radius determination by a factor of 3.8 compared to PRad. As the muonic hydrogen result with its unprecedented precision ($\sim$0.05%) dominates the CODATA value of the proton charge radius, it is critically important to help evaluate possible systematic uncertainties associated with muonic experiments using different experimental methods with high precision and different systematics. The PRad-II experiment, with its projected total uncertainty smaller than 0.5%, could potentially inform whether there is any systematic difference in the radius results between $e-p$ scattering and muonic hydrogen measurements. PRad-II will cover a Q^2 range of 4×10^{-6} to 2×10^{-2} (GeV/c)^2 – the first lepton scattering experiment to reach below 10^{-4} (GeV/c)^2 – with three proposed incident beam energies: 0.7, 1.4 and 2.1 GeV. Fig. 24 shows the schematics of the proposed PRad-II setup. The tracking detectors proposed can be built based on the new μRWELL technology (Bencivenni *et al.*, 2015), or the GEM as used in the PRad experiment.

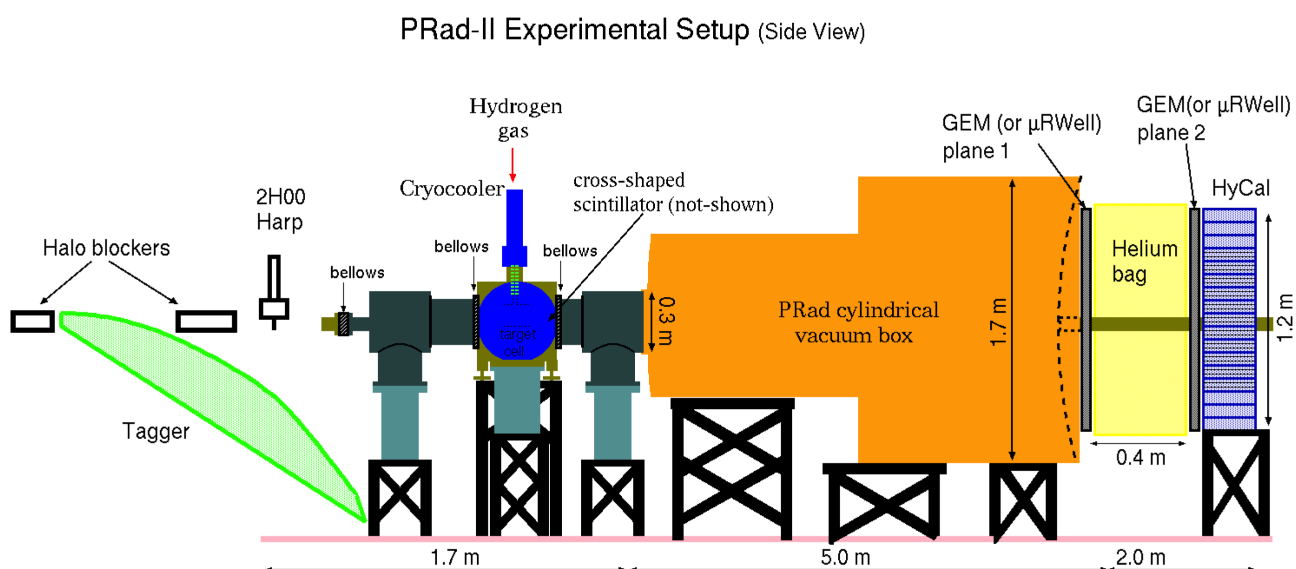

FIG. 24 (Color online) Schematic of the setup for the proposed PRad-II experiment. The incident electron beam is from left to right (figure credit: Dipangkar Dutta).

Fig. 25 shows the projected radius measurement from PRad-II together with some of the most recent results on the proton radius including the $e-p$ scattering results (Xiong *et al.*, 2019), the two muonic hydrogen results (Antognini *et al.*, 2013a; Pohl *et al.*, 2010), and the three recent atomic hydrogen spectroscopic results (Beyer *et al.*, 2017; Bezginov *et al.*, 2019; Grinin *et al.*, 2020). Also shown is the CODATA 2018 (Tiesinga *et al.*, 2021) recommended value. The blue line and the band represent the weighted average of the $\langle r_{Ep}^2 \rangle^{1/2}$ value and its uncertainty of the three proton radius values (Beyer *et al.*, 2017; Bezginov *et al.*, 2019; Xiong *et al.*, 2019) from ordinary hydrogen spectroscopy and electron-proton scattering. The grey line and band are the results from the weighted average of all four including the result from (Grinin *et al.*, 2020). This figure illustrates two points: (i) the importance of improving the precision of $\langle r_{Ep}^2 \rangle^{1/2}$ measurements from electronic systems whether it be ordinary hydrogen spectroscopy or electron-proton scattering; (ii) additional new measurements from ordinary hydrogen in addition to the results from (Grinin *et al.*, 2020) and the upcoming PRad-II will be essential to determine whether there is a difference between $\langle r_{Ep}^2 \rangle^{1/2}$ determined between the electronic versus the muonic systems.

For the PRad-II projection, it is shown that with all proposed upgrades and improvements, the projected overall uncertainty in the proton radius measurement will be 0.0036 fm, which is slightly smaller than the 0.0038 fm precision from the latest hydrogen spectroscopy result of (Grinin *et al.*, 2020) – the most precise measurement from ordinary hydrogen atomic spectroscopy.

If the PRad $\langle r_{Ep}^2 \rangle^{1/2}$ value would prevail, the PRad-II result could signal a more than 2.7 standard deviations smaller value than the muonic hydrogen result. While it does not seem possible in the foreseeable future for lepton-scattering experiments to reach the precision of muonic hydrogen spectroscopic measurements, the improvement of PRad-II is significant and will have great potential to inform whether there is any systematic difference between muonic hydrogen results and results from electron scattering. The PRad-II measurement together with future improvements in ordinary hydrogen spectroscopic measurements will shed light on whether there is any systematic difference between the proton charge radius determined from electronic versus muonic systems. Therefore, they may uncover interesting new physics such as the violation of lepton universality.

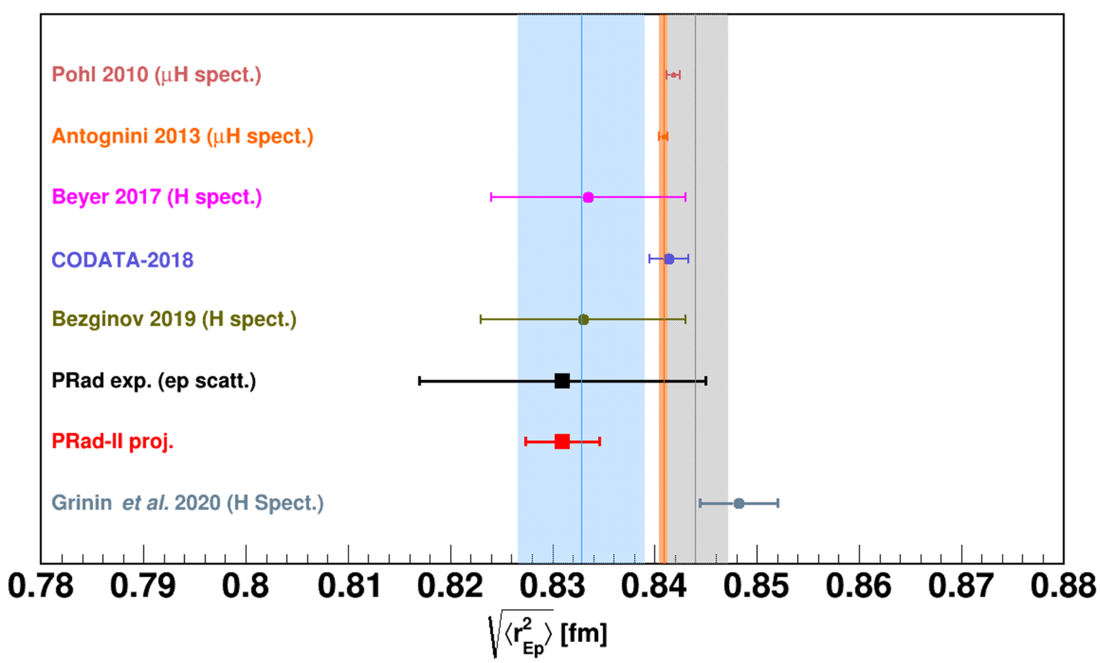

FIG. 25 (Color online) The PRad-II projection for $\langle r_{Ep}^2 \rangle^{1/2}$ with all proposed upgrades and improvements shown with a few selected results from other experiments and CODATA-2018 recommendations (see text) (figure credit: Jingyi Zhou).

D. Electron scattering experiments at Mainz University

There are two major new programs at Mainz University aimed at measuring the electron-proton elastic scattering at low Q^2, which will provide new results on the proton charge radius in the coming years.

The first is the PRES experiment (Belostotski *et al.*, 2019; Vorobyev, 2019; Vorobyov and Denig, 2017) at the Microtron MAMI in the A2 experimental hall. In this experiment the polar angle of the scattered electron will be measured with high accuracy using a Forward Tracker. For the recoil proton the energy and the angle will be measured with a time projection chamber (TPC). Therefore, the experiment will have overdetermined kinematics, and access $e-p$ elastic scattering in a Q^2 region from 0.001 to 0.04 $(\mathrm{GeV/c})^2$. Compared with other $e-p$ scattering experiments in which scattered electrons are commonly measured, the Mainz PRES experiment will have different systematics. The projected systematic error for the cross section will be controlled with an accuracy of 0.1% (relative) and 0.2% (absolute). The PRES experiment is projected to reach 0.5% statistical precision on $\langle r_{Ep}^2 \rangle^{1/2}$, with systematic errors $\leq 0.3\%$. The combination of the electron scattering result from the PRES experiment and the muon scattering result from COMPASS++/AMBER will allow for a test of lepton universality in the proton charge radius, taking advantage of a very similar experimental approach used in both measurements. Also, PRES will provide crucial input for calibration of the TPC setup at COMPASS++/AMBER, taking advantage of the high-quality electron beam delivered by MAMI.

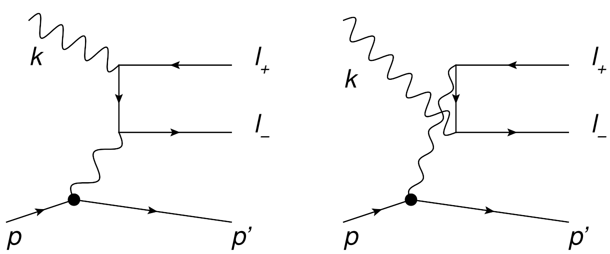

FIG. 26 Bethe-Heitler direct (left) and crossed (right) diagrams to the $\gamma p \to l^- l^+ p$ process, where the four-momenta of the external particles are: k for the photon, $p(p')$ for initial (final) protons, and l_-, l_+ for the lepton pair.

A further test of the lepton universality in the proton charge radius extraction was proposed in (Pauk and Vanderhaeghen, 2015) through the photoproduction of a lepton pair on a proton target in the limit of small momentum transfer, in which this reaction is dominated by the Bethe-Heitler process shown in Fig. 26. By detecting the recoiling proton in the $\gamma p \to l^- l^+ p$ reaction, it was shown that a measurement of a cross section ratio of $e^-e^+ + \mu^-\mu^+$ vs e^-e^+, above vs below dimuon threshold respectively, accesses the same information as muon vs electron scattering experiments. Furthermore such a measurement is free from hadronic background if one performs the measurement in the di-lepton mass window between di-muon threshold and below $\pi\pi$ threshold. It thus complements a comparison of elastic $l-p$ scattering data, as the overall normalization uncertainty due to the photon flux drops out of the di-lepton photoproduction cross section ratio. The feasibility of such experiment using a high-pressure TPC as an active target in combination with the Crystal Ball/TAPS setup at MAMI is currently under study (Sokhoyan, 2020).

The second program at Mainz consists of two parts. The first is the A1@MAMI, an ongoing experiment (Bernauer, Jan C., 2020) in the A1 experimental hall with the MAMI accelerator using a hydrogen gas jet target to provide better control of a few systematic uncertainties associated with the original A1 experiment (Bernauer *et al.*, 2010), and also to investigate the systematic difference in the G_E^p results between the PRad (Xiong *et al.*, 2019) and the A1 experiments. The second (MAGIX@MESA) is centered around the Mainz Superconducting Energy Recovery Linac (MESA), which is a new accelerator presently under construction at the University of Mainz (Hug *et al.*, 2020). MESA is designed as a recirculating superconducting linear accelerator which provides an external beam with high current and high degree of polarization. In the energy recovery mode, MESA will deliver an electron beam with 20 - 105 MeV and a current of 1 mA, which is ideal for precision experiments. The MAGIX experiment (Mainz Gas-Internal Target Experiment) at MESA will consist of a quadrupole in front of two medium sized dipole magnets, see Fig. 27. The compact design of the spectrometers will allow for a relative momentum resolution of order 10^{-4}. For the focal-plane detector, a time projection chamber with an open field cage and GEM readout is being developed (Caiazza *et al.*, 2020; Gülker *et al.*, 2019). Finally, a windowless internal gas-jet target (Grieser *et al.*, 2018), which has already been commissioned at MAMI (Schlimme *et al.*, 2021), will be used.

With the MAGIX experiment at MESA, for the first time in hadron physics, an experiment will be developed that combines the advantages of an ultra-light windowless gas target with the high intensity of an Energy Recovery Linac accelerator. This combination of a high beam intensity and a target, in which multiple scattering of the outgoing particles will be minimized, will lead to competitive luminosities in the range of 10^{35} cm^{-2} s^{-1}, while providing at the same time a very clean experimental environment. With the low beam energies of MESA, it will be possible to reach Q^2 values in $e-p$ scattering down to 10^{-4} $(\mathrm{GeV/c})^2$, and a relative precision on the proton electron form factor G_{Ep} down to 0.05 %. It will also significantly improve the determination of the proton magnetic radius (Bernauer, Jan C., 2020).

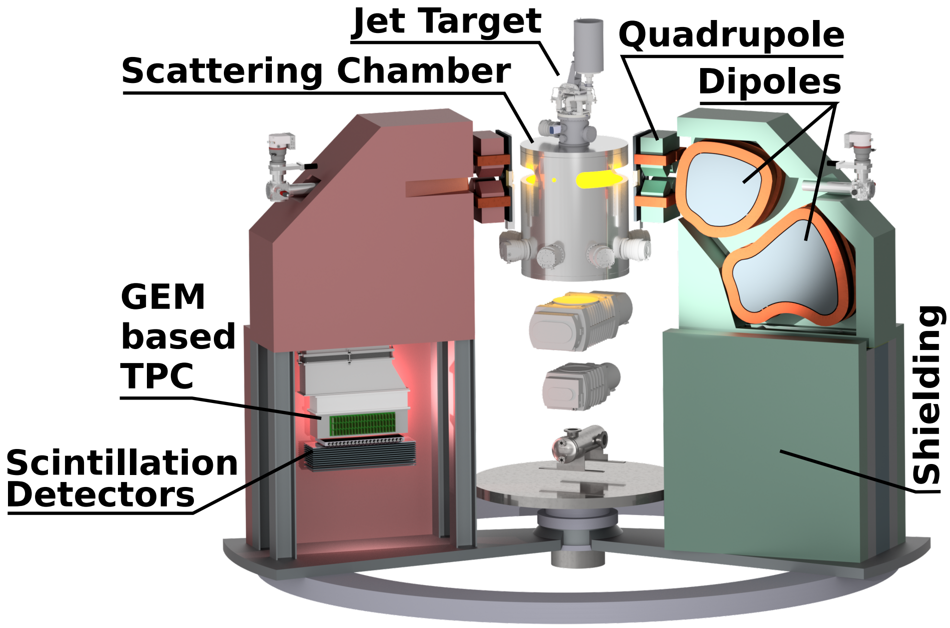

FIG. 27 (Color online) The MAGIX high resolution dual-spectrometer setup at the MESA accelerator. The gas-jet target in the centre is also visible (figure credit: MAGIX Collaboration, (Schlimme *et al.*, 2021)).

E. The ULQ^2 experiment at Tohoku University

The Ultra-Low Q^2 (ULQ^2) (Suda, T., 2018) collaboration has proposed to carry out an electron-scattering experiment at the Research Center for Electron-Photon Science at Tohoku University using its 60 MeV electron linac. This experiment will use the electron beam at energies from 20-60 MeV with a scattering angular range of 30 to 150°, corresponding to a Q^2 range of 0.0003 to 0.008 $(\mathrm{GeV/c})^2$ for $e-p$ elastic scattering, aiming at an absolute cross section measurement with a precision of 0.1 %. The ULQ^2 experiment will use a CH_2 target with elastic $e-{}^{12}$C as a reference reaction for normalization purposes. The root-mean-square charge radius of the ^{12}C nucleus is known to a relative precision of $\sim 3 \times 10^{-3}$. The proton electric form factor G_{Ep} will be extracted using the Rosenbluth separation technique. The proposed experimental setup will consist of two magnetic spectrometers for Rosenbluth separation measurements, and luminosity monitoring. To carry out this experiment, a new beam line and a high-resolution new spectrometer with single-sided silicon detectors (SSD) have been built and commissioned already. The SSD, developed together with the J-PARC muon g-2 and the neutron electric dipole moment experiments (Sato, 2017) are employed as the focal plane detector. The second spectrometer for luminosity monitoring is under construction and will be commissioned in the near future. This experiment is aiming at a precision of $\sim$ 1% (relative.) in determining the proton charge radius, and is expected to start data taking in 2022. Fig. 28 shows the schematics of the ULQ^2 experimental setup.

In Table V we provide a summary of these ongoing and future lepton scattering experiments in terms of beam type(s), the location, the Q^2 coverage, the projected precision in the proton charge radius determination when available, and the status of each experiment.

VIII. THE DEUTERON CHARGE RADIUS

A less well known charge radius puzzle is concerning the deuteron, the simplest nucleus in nature, which is loosely bound with a binding energy of 2.2 MeV. Like the proton, the deuteron charge radius can be determined by the extraction of the deuteron charge form factor, $G_{Cd}(Q^2)$ at low values of Q^2 from electron-deuteron elastic scattering first, and the subsequent extrapolation of the measured $G_{Cd}(Q^2)$ to the unmeasured region in order to determine its slope at $Q^2 = 0$.

The unpolarized elastic $e-d$ scattering cross section is described in the one-photon exchange picture as

$$\frac{\mathrm{d}\sigma}{\mathrm{d}\Omega}(E,\theta) = \sigma_{NS}\left\{A_d(Q^2) + B_d(Q^2)\,\tan^2\frac{\theta}{2}\right\}, \qquad (78)$$

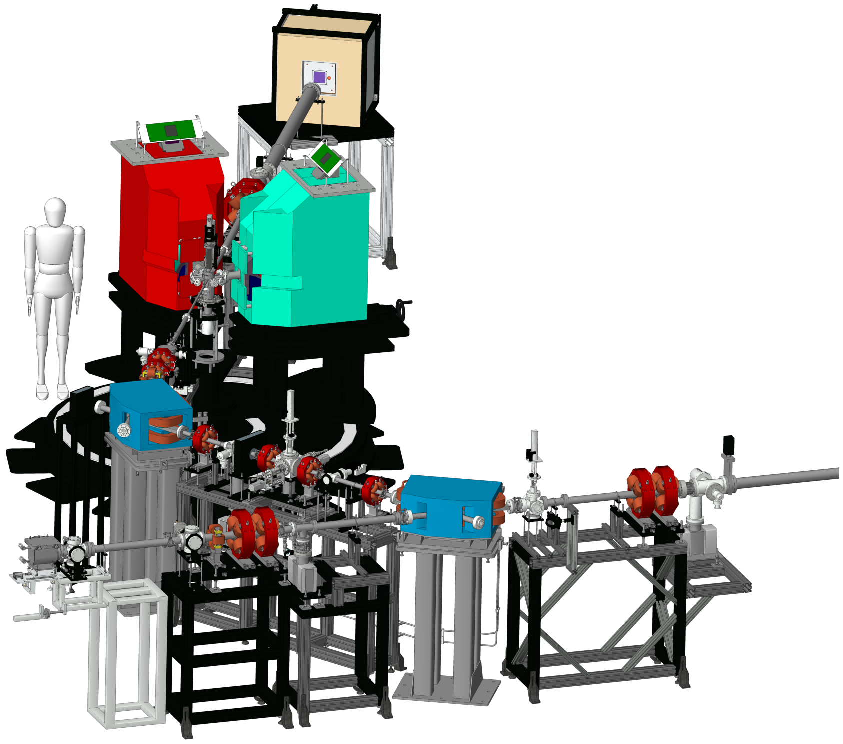

FIG. 28 (Color online) The schematics of the ULQ^2 experimental setup (figure credit: Toshimi Suda).

Experiment	Beam	Laboratory	Q^2 (GeV/c)^2	δr_p (fm)	Status
MUSE	$e^\pm$, $\mu^\pm$	PSI	0.0015 - 0.08	0.01	Ongoing
AMBER	$\mu^\pm$	CERN	0.001 - 0.04	0.01	Future
PRad-II	e^-	Jefferson Lab	4×10^{-5} - 6×10^{-2}	0.0036	Future
PRES	e^-	Mainz	0.001 - 0.04	0.6% (rel.)	Future
A1@MAMI (jet target)	e^-	Mainz	0.004 - 0.085		Ongoing
MAGIX@MESA	e^-	Mainz	$\geq 10^{-4} - 0.085$		Future
ULQ^2	e^-	Tohoku University	3×10^{-4} - 8×10^{-3}	$\sim 1\%$ (rel.)	Future

TABLE V Summary of ongoing and future lepton scattering experiments on proton charge radius measurements.

where σ_{NS} is the differential cross section for the elastic scattering from a point-like and spinless particle at a scattering angle θ and an incident energy E. For a spin-1 object such as the deuteron, its electromagnetic structure can be described by three form factors: the charge G_{Cd}, the magnetic dipole G_{Md}, and the electric quadrupole G_{Qd}. The structure functions $A_d(Q^2)$, $B_d(Q^2)$ are related to these form factors via (Gourdin, 1963; Jankus, 1956):

$$A_d(Q^2) = G_{Cd}^2(Q^2) + \frac{2}{3}\,\tau_d G_{Md}^2(Q^2) + \frac{8}{9}\,\tau_d^2 G_{Qd}^2(Q^2),$$
$$B_d(Q^2) = \frac{4}{3}\,\tau_d(1+\tau_d)G_{Md}^2(Q^2), \tag{79}$$

with $\tau_d \equiv Q^2/(4M_d^2)$, where M_d is the deuteron mass. Also, there are the following additional relations:

$$G_{Cd}(0) = 1, \quad G_{Md}(0) = \mu_d, \quad G_{Qd}(0) = Q_d,$$

with μ_d being the deuteron magnetic dipole moment (in units $e/(2M_d)$), and Q_d, the electric quadrupole moment (in units e/M_d^2). With three form factors, one needs to carry out three measurements with independent combinations of the three form factors in order to separate them for each Q^2 value. It was shown in (Carlson and Vanderhaeghen, 2009) how these three form factors allows one to map out the transverse charge densities in a deuteron, in a state of helicity 0 or ±1, as viewed from a light front moving towards the deuteron. Furthermore, the charge densities for a transversely polarized deuteron are characterized by monopole, dipole and quadrupole patterns.

At low values of Q^2 most relevant for the charge radius determination, in the range 10^{-2} to 10^{-4} (GeV/c)^2, and small scattering angles, the unpolarized $e-d$ elastic scattering cross section is dominated by the deuteron charge form factor. One can therefore extract G_{Cd} with negligible systematic uncertainties using data driven parameterizations for G_{Md}, and G_{Qd} (Zhou *et al.*, 2021) from measured scattering cross section. The deuteron rms charge radius radius can then be determined by fitting the experimental G_{Cd} data as a function of Q^2, and calculating the slope of this function at $Q^2 = 0$, according to

$$\langle r_{Cd}^2 \rangle \equiv -6 \left. \frac{\mathrm{d}G_C^d(Q^2)}{\mathrm{d}Q^2} \right|_{Q^2=0}, \tag{80}$$

in analogy to how $\langle r_{Ep}^2 \rangle$ is obtained. Zhou *et al.* (Zhou *et al.*, 2021) demonstrated how one can extract r_d reliably using robust fitters.

Like the proton charge radius, the deuteron r_d can also be determined from atomic spectroscopic measurements using ordinary deuterium or muonic deuterium atoms. The CREMA collaboration has reported a deuteron charge radius value from a muonic spectroscopy-based measurement of three $2P \to 2S$ transitions in muonic deuterium atoms as (Pohl *et al.*, 2016) (labeled as μD 2016 in Fig. 27.)

$$\langle r_{Cd}^2 \rangle^{1/2} = 2.12562 \pm 0.00078 \text{ fm}, \tag{81}$$

which is 2.7 times more accurate but 7.5 standard deviations smaller than the CODATA-2010 recommended value (Mohr, 2012). Newer values of $\langle r_{Cd}^2 \rangle^{1/2}$ based on the muonic deuterium spectroscopic measurement (Pohl *et al.*, 2016) with improved theoretical calculations are (Hernandez *et al.*, 2018)

$$\langle r_{Cd}^2 \rangle^{1/2} = 2.12616 \pm 0.00090 \text{ fm},$$

and (Kalinowski, 2019; Pachucki *et al.*, 2018)

$$\langle r_{Cd}^2 \rangle^{1/2} = 2.12717 \pm 0.00082 \text{ fm}.$$

From the spectroscopic measurement of $1S \to 2S$ transitions from ordinary deuterium atoms (Parthey *et al.*, 2010), Pohl *et al.* extracted a deuteron radius value (Pohl *et al.*, 2017):

$$\langle r_{Cd}^2 \rangle^{1/2} = 2.1415 \pm 0.0045 \text{ fm},$$

which is 3.5 standard deviations larger than the extracted value of Eq. (81) from muonic deuterium atoms.

Another spectroscopic method commonly used to extract the deuteron charge radius utilizes the isotope shift of the $1S \to 2S$ transition between atomic hydrogen and deuterium (Huber *et al.*, 1998; Parthey *et al.*, 2010), from which one can precisely determine the difference between the squares of the deuteron and proton charge radii (Jentschura *et al.*, 2011):

$$\langle r_{Cd}^2 \rangle - \langle r_{Ep}^2 \rangle = 3.82007(65) \text{ fm}^2.$$

Combining the proton charge radius values with the isotope shift results, one can extract $\langle r_{Cd}^2 \rangle^{1/2}$. In fact, the CODATA-2010 recommended value

$$\langle r_{Cd}^2 \rangle^{1/2} = 2.1415\,(21) \text{ fm},$$

used the isotope shift results on the radii and the proton charge radius values from electron scattering.

From the electron scattering side, all the elastic $e-d$ scattering measurements with rather large experimental uncertainties are not able to resolve the discrepancy between the $\langle r_{Cd}^2 \rangle^{1/2}$ values obtained from ordinary deuterium and muonic deuterium spectroscopic measurements. The re-analysis of world $e-d$ data gives (Sick and Trautmann, 1998):

$$\langle r_{Cd}^2 \rangle^{1/2} = 2.130 \pm 0.003\,(\text{stat.}) \pm 0.009\,(\text{syst.}) \text{ fm}.$$

With rather large overall uncertainty, this deuteron charge radius value from the re-analysis is consistent with both the muonic deuterium result as well as that from ordinary deuterium spectroscopic measurements.

A recent analysis (Hayward and Griffioen, 2020) gives a deuteron charge radius value that is consistent with muonic deuterium results with a larger statistical uncertainty:

$$\langle r_{Cd}^2 \rangle^{1/2} = 2.092 \pm 0.019\,(\text{stat.}) \text{ fm}.$$

In the same work, the analysis of the electron-proton scattering data prefers a proton radius value consistent with muonic hydrogen results.

Therefore, a significantly improved $\langle r_{Cd}^2 \rangle^{1/2}$ determination from a new electron-deuteron scattering experiment is needed to help resolve the current situation surrounding the deuteron charge radius. Fig. 29 is a summary of results on the deuteron charge radius discussed above including the CODATA 2014 value (Mohr *et al.*, 2016) shown with the uncertainty as a band, and the CODATA 2018 recommended value (Tiesinga *et al.*, 2021). Also included is an extraction of the r_d using the isotope shift (Jentschura *et al.*, 2011) and the muonic hy-

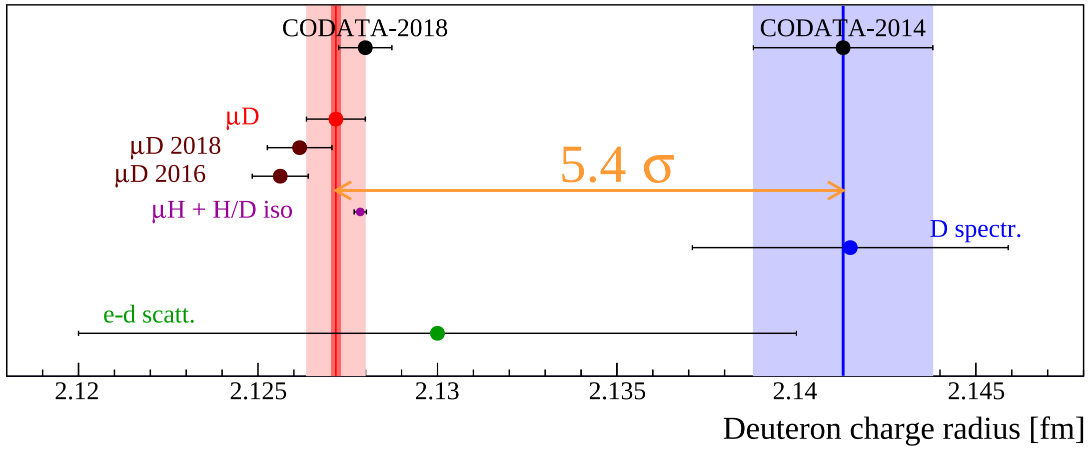

FIG. 29 (Color online) The existing results on the deuteron charge radius $\langle r_{Cd}^2 \rangle^{1/2}$, see text for details (figure credit: Randolf Pohl).

drogen result of the $\langle r_{Ep}^2 \rangle$ (Antognini *et al.*, 2013a). The two latest extractions of the deuteron charge radius from the muonic deuterium measurement are labeled as μD 2018 (Hernandez *et al.*, 2018), and μD (Kalinowski, 2019; Pachucki *et al.*, 2018), respectively in Fig. 29.

The PRad collaboration proposed a new electron-deuteron elastic scattering experiment, called DRad (Jefferson Lab Proposal PR12-20-006, Spokespersons: D. Dutta, H. Gao, A. Gasparian (contact), D. Higinbotham, N. Liyanage, and E. Pasyuk, 2020), using an apparatus modified from that for the proposed PRad-II experiment by installing a low-energy Silicon-based recoil detector in a cylindrical shape inside the windowless gas flowing target to detect the recoil deuterons in coincidence with the scattered electrons. As demonstrated by the PRad experiment (Xiong *et al.*, 2019), the proposed DRad experiment will also employ a well-known QED process, Møller scattering, to control the systematic uncertainties associated with measuring the absolute $e-d$ cross section. The DRad experiment will aim at an overall precision that is 0.22% (relative) or better in the determination of the r_d, in an essentially model-independent way.

An elastic $e-d$ cross section measurement (Schlimme *et al.*, 2016) was carried out at the Mainz Microtron several years ago in a momentum transfer squared range of 2.2×10^{-3} to 0.28 $(\mathrm{GeV/c})^2$ with the goal of extracting the deuteron charge form factor and ultimately the deuteron charge radius. The data analysis is ongoing.

Furthermore, Carlson and Vanderhaeghen investigated the sensitivity of the cross section for lepton pair production off a deuteron target, $\gamma d \to e^+e^-d$, to the deuteron charge radius (Carlson *et al.*, 2019). They demonstrated that for small momentum transfer this reaction is dominated by the Bethe-Heitler process, shown in Fig. 26. They propose to measure the deuteron at a fixed angle, and scan the momentum transfer (t) dependence of the $\gamma d \to e^+e^-d$ cross section ratio defined as:

$$R(t, t_0) \equiv \frac{d\sigma/dt\, dM_{ll}^2(t)}{d\sigma/dt\, dM_{ll}^2(t_0)}, \tag{82}$$

with $t = (p' - p)^2$ the momentum transfer, which is in one-to-one relation with the recoil deuteron lab momentum, $|\vec{p}\,'|^{lab} = 2M_d\sqrt{\tau_d(1+\tau_d)}$, with $\tau_d \equiv -t/(4M_d^2)$. Furthermore in Eq. (82), M_{ll}^2 is the squared invariant mass of the dilepton pair, which at a fixed deuteron angle is a function of t, and the denominator in the ratio R is the cross section for the same deuteron scattering angle and for a reference momentum transfer t_0. This ratio is shown in Fig. 30 for three extractions of the deuteron charge radius displayed in Fig. 29: the muonic deuterium Lamb shift value (Pohl *et al.*, 2016) (gold solid line, with uncertainty comparable to the width of the line); *e-d* elastic scattering value (Sick and Trautmann, 1998) (green dashed line, with uncertainty limits indicated by the green band) and the deuterium atomic spectroscopy value (Pohl *et al.*, 2017) (red dot-dashed line, with uncertainty limits indicated by the red band). One sees from Fig. 30 that such cross section ratio measurement of about 0.1% relative accuracy could give a deuteron charge radius more accurate than the current $e-d$ scattering value (Sick and Trautmann, 1998) and sufficiently accurate to distinguish between the electronic and muonic atomic values.

IX. CONCLUSIONS

In this paper, we reviewed the experimental progress towards the resolution of the proton charge radius puzzle over the past decade as well as the related theoretical background and developments. In light of the lat-

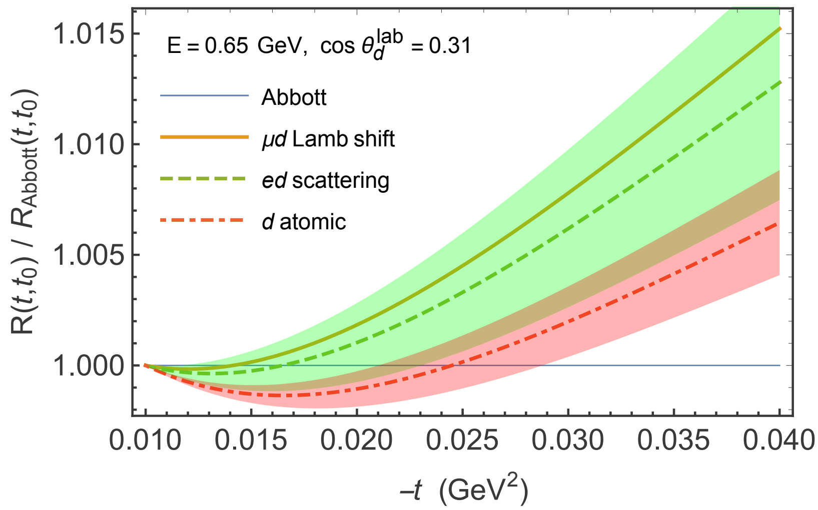

FIG. 30 (Color online) The momentum transfer t-dependence of the $\gamma d \to e^+e^- d$ cross section ratio $R(t, t_0)$, defined in Eq. (82), for reference value $t_0 = -0.01$ GeV^2, at fixed deuteron lab angle, and for beam energy 0.65 GeV. For convenience, the ratio is normalized to the result using Abbott *et al.* form factors (Abbott *et al.*, 2000). The curves and associated error bands are for different extractions of the deuteron charge radius (see text for details). Figure from (Carlson *et al.*, 2019).

est precise determinations of the proton charge radius from ordinary atomic hydrogen spectroscopic measurements, the PRad electron scattering experiment, and several improved re-analyses of electron scattering data, some might be tempted to conclude that the puzzle has been resolved. We point out however, while the recent experimental results prefer the CREMA value at about 0.84 fm, they are still within 3 standard deviations from the previously compiled value of about 0.88 fm. Furthermore, the most precisely determined value of r_{Ep} (Grinin *et al.*, 2020) from ordinary hydrogen spectroscopy – also the most recent measurement – is about two standard deviations larger than the muonic hydrogen results. We believe more experiments, especially those with improved precision from electron scattering, and new results from muon scattering will be essential to fully resolve this puzzle. To answer a more tantalizing question – whether there is a difference in the proton charge radius determined from experiments involving electronic (e-p and ordinary hydrogen) versus muonic systems – significantly improved precision from lepton scattering and also measurements from ordinary hydrogen spectroscopy with precision comparable to that of (Grinin *et al.*, 2020) will be critical. Pushing the precision frontier has more than once proven to be the harbinger of new discoveries.

X. ACKNOWLEDGMENTS

H.G. thanks Xiangdong Ji for bringing the proton charge radius issue to her attention for the first time in the late 1990s. H.G. wishes to thank all members of the PRad Collaboration, especially Chao Peng, Weizhi Xiong, Xinzhan Bai, Chao Gu, Xuefei Yan, Dipangkar Dutta, Ashot Gasparian, Kondo Gnanvo, Mahbub Khandaker, Douglas Higinbotham, Nilanga Liyanage, Eugene Pasyuk, Jingyi Zhou, Yang Zhang, and Vladimir Khachatryan.

M.V. wishes to thank his collaborators on various works summarized here, especially Carl Carlson, Mikhail Gorchtein, Michel Guidal, Nikolai Kivel, Cédric Lorcé, Vladimir Pascalutsa, Barbara Pasquini, Vladyslav Pauk, Oleksandr Tomalak.

H.G and M.V. wish to thank Randolf Pohl for helpful discussions concerning the deuteron charge radius measurements, Stephan Paul for the AMBER experiment, Jan Bernauer for Mainz experiments, Ron Gilman for the MUSE experiment, Toshimi Suda for the ULQ^2 experiment, Weizhi Xiong and Jingyi Zhou for their assistance in making a number of figures used in this paper, and Gregory Matousek for careful reading of the manuscript. H.G. and M.V. also thanks Alexandr Gramolin, Douglas Higinbotham, Cédric Lorcé, Vahe Sokhoyan, and Nikos Sparveris for helpful comments about the manuscript.

The work of H.G. is supported in part by the U.S. Department of Energy under Contract No. DE-FG02-03ER41231.

The work of M.V. is supported by the Deutsche Forschungsgemeinschaft (DFG, German Research Foundation), in part through the Collaborative Research Center [The Low-Energy Frontier of the Standard Model, Projektnummer 204404729 - SFB 1044], and in part through the Cluster of Excellence [Precision Physics, Fundamental Interactions, and Structure of Matter] (PRISMA$^+$ EXC 2118/1) within the German Excellence Strategy (Project ID 39083149).

REFERENCES

Abbott, D, *et al.* (JLAB t20) (2000), "Phenomenology of the deuteron electromagnetic form-factors," Eur. Phys. J. **A7**, 421–427.

Abrahamyan, S, *et al.* (HAPPEX, PREX) (2012), "New Measurements of the Transverse Beam Asymmetry for Elastic Electron Scattering from Selected Nuclei," Phys. Rev. Lett. **109**, 192501.

Accardi, A, *et al.* (2016), "Electron-ion collider: The next qcd frontier," The European Physical Journal A **52**, 268.

Adamuscin, C, S. Dubnicka, and A.Z. Dubnickova (2012), "New value of the proton charge root mean square radius," Progress in Particle and Nuclear Physics **67** (2), 479–485, from Quarks and Gluons to Hadrons and Nuclei.

Adikaram, D, *et al.* (CLAS) (2015), "Towards a resolution of the proton form factor problem: new electron and positron scattering data," Phys. Rev. Lett. **114**, 062003.

Afanasev, Andrei, Igor Akushevich, and N. P. Merenkov (2002), "Nucleon Compton scattering with two space - like photons," in *Exclusive Processes at High Momentum Transfer*, arXiv:hep-ph/0208260.

Ahmed, Jaseer, P. G. Blunden, and W. Melnitchouk (2020), "Two-photon exchange from intermediate state resonances in elastic electron-proton scattering," Phys. Rev. C **102** (4), 045205.

Alarcón, J M, D. W. Higinbotham, and C. Weiss (2020), "Precise determination of the proton magnetic radius from electron scattering data," Phys. Rev. C **102**, 035203.

Alarcón, J M, D. W. Higinbotham, C. Weiss, and Zhihong Ye (2019), "Proton charge radius extraction from electron scattering data using dispersively improved chiral effective field theory," Phys. Rev. C **99**, 044303.

Alarcón, JM, and C. Weiss (2018), "Accurate nucleon electromagnetic form factors from dispersively improved chiral effective field theory," Physics Letters B **784**, 373 – 377.

Alarcon, Jose Manuel, Vadim Lensky, and Vladimir Pascalutsa (2014), "Chiral perturbation theory of muonic hydrogen Lamb shift: polarizability contribution," Eur. Phys. J. C **74** (4), 2852.

Alexandrou, C, S. Bacchio, M. Constantinou, J. Finkenrath, K. Hadjiyiannakou, K. Jansen, G. Koutsou, and A. Vaquero Aviles-Casco (2019), "Proton and neutron electromagnetic form factors from lattice QCD," Phys. Rev. D **100** (1), 014509.

Alexandrou, Constantia, Kyriakos Hadjiyiannakou, Giannis Koutsou, Konstantin Ottnad, and Marcus Petschlies (2020), "Model-independent determination of the nucleon charge radius from lattice QCD," Phys. Rev. D **101** (11), 114504.

Androic, D, *et al.* (G0) (2011), "Transverse Beam Spin Asymmetries at Backward Angles in Elastic Electron-Proton and Quasi-elastic Electron-Deuteron Scattering," Phys. Rev. Lett. **107**, 022501.

Androić, D, *et al.* (QWeak) (2020), "Precision Measurement of the Beam-Normal Single-Spin Asymmetry in Forward-Angle Elastic Electron-Proton Scattering," Phys. Rev. Lett. **125** (11), 112502.

Anselmino, M, A. Mukherjee, and A. Vossen (2020), "Transverse spin effects in hard semi-inclusive collisions," Progress in Particle and Nuclear Physics **114**, 103806.

Antognini, A, *et al.* (2013a), "Proton Structure from the Measurement of 2S-2P Transition Frequencies of Muonic Hydrogen," Science **339**, 417.

Antognini, Aldo, Franz Kottmann, Francois Biraben, Paul Indelicato, Francois Nez, and Randolf Pohl (2013b), "Theory of the 2S-2P Lamb shift and 2S hyperfine splitting in muonic hydrogen," Annals Phys. **331**, 127–145.

Arbuzov, Andrej B, Eduard A Kuraev, Nikolay P Merenkov, and Luca Trentadue (1998), "Hadronic cross sections in electron-positron annihilation with tagged photon," Journal of High Energy Physics **1998** (12), 009–009.

Armstrong, David S, *et al.* (G0) (2007), "Transverse Beam Spin Asymmetries in Forward-Angle Elastic Electron-Proton Scattering," Phys. Rev. Lett. **99**, 092301.

Arnold, R, Carlson CE Gross F (1981), "Polarization transfer in elastic electron scattering from nucleons and deuterons," Phys. Rev. C **23**, 363.

Arrington, J, P. G. Blunden, and W. Melnitchouk (2011), "Review of two-photon exchange in electron scattering," Prog. Part. Nucl. Phys. **66**, 782–833.

Arrington, J, Melnitchouk W Tjon JA (2007), "Global analysis of proton elastic form factor data with two-photon exchange corrections," Phys. Rev. C. **76**, 035205.

Arrington, J, Sick I (2015), "Evaluation of the Proton Charge Radius from Electron-Proton Scattering," J. Phys. Chem. Ref. Data **44**, 031204.

Ashman, J, *et al.* (1988), "A measurement of the spin asymmetry and determination of the structure function g_1 in deep inelastic muon-proton scattering," Physics Letters B **206**, 364–370.

Atac, H, M. Constantinou, Z.-E. Meziani, M. Paolone, and N. Sparveris (2021), "Charge radii of the nucleon from its flavor dependent dirac form factors," The European Physical Journal A **57** (2), 65.

Aubert, B, *et al.* (BABAR Collaboration) (2004), "J/ψ production via initial state radiation in $e^+e^- \to \mu^+\mu^-\gamma$ at an e^+e^- center-of-mass energy near 10.6 GeV," Phys. Rev. D **69**, 011103.

Balaguer Rios, D (2012), "Two-photon exchange and normal spin asymmetries in the A4 experiment," Nuovo Cim. C **035N04**, 198–202.

Barker, W A, Glover F N (1955), "Reduction of Relativistic Two-Particle Wave Equations to Approximate Forms. III," Phys. Rev. **99**, 317–324.

Belitsky, AV, Xiangdong Ji, and Feng Yuan (2004), "Quark imaging in the proton via quantum phase-space distributions," Phys. Rev. D **69**, 074014.

Belitsky, AV, and A.V. Radyushkin (2005), "Unraveling hadron structure with generalized parton distributions," Phys. Rept. **418**, 1–387.

Belostotski, S, N. Sagidova, and A. Vorobyev (2019), "Proton radius reconstruction from simulated electron-proton elastic scattering cross sections at low transfer momenta," arXiv:1903.04975 [hep-ph].

Bencivenni, G, R. De Oliveira, G. Morello, and M. Poli Lener (2015), "The micro-resistive WELL detector: a compact spark-protected single amplification-stage MPGD," Journal of Instrumentation **10** (02), P02008–P02008.

Berkeland, D J, Hinds EA Boshier MG (1995), "Precise Optical Measurement of Lamb Shifts in Atomic Hydrogen," Phys. Rev. Lett. **75**, 2470.

Bernauer, J, *et al.* (2010), "High-Precision Determination of the Electric and Magnetic Form Factors of the Proton," Phys. Rev. Lett. **105**, 242001.

Bernauer, J C, *et al.* (A1) (2014), "Electric and magnetic form factors of the proton," Phys. Rev. C **90** (1), 015206.

Bernauer, Jan C., (2020), "The proton radius puzzle - 9 years later," EPJ Web Conf. **234**, 01001.

Beyer, A, *et al.* (2016), "Active fiber-based retroreflector providing phase-retracing anti-parallel laser beams for precision spectroscopy," Opt. Express **24** (15), 17470–17485.

Beyer, Axel, *et al.* (2017), "The Rydberg constant and proton size from atomic hydrogen," Science **358** (6359), 79–85.

Bezginov, N, T. Valdez, M. Horbatsch, A. Marsman, A. C. Vutha, and E. A. Hessels (2019), "A measurement of the atomic hydrogen Lamb shift and the proton charge radius," Science **365** (6457), 1007–1012.

Birse, M C, McGovern JA (2012), "Proton polarisability contribution to the Lamb shift in muonic hydrogen at fourth order in chiral perturbation theory," Eur. Phys. J. A **48**, 120.

Bloom, Elliott D, *et al.* (1969), "High-Energy Inelastic e p Scattering at 6-Degrees and 10-Degrees," Phys. Rev. Lett. **23**, 930–934.

Blunden, P G, W. Melnitchouk, and J. A. Tjon (2003), "Two photon exchange and elastic electron proton scattering," Phys. Rev. Lett. **91**, 142304.

Boffi, Sigfrido, and Barbara Pasquini (2007), "Generalized parton distributions and the structure of the nucleon," Riv. Nuovo Cim. **30**, 387.

Borie, E (2012), "Lamb shift in light muonic atoms: Revisited," Annals Phys. **327**, 733–763.

Borisyuk, Dmitry (2010), "Proton charge and magnetic rms radii from the elastic ep scattering data," Nuclear Physics A **843** (1), 59–67.

Borisyuk, Dmitry, and Alexander Kobushkin (2009), "Perturbative QCD predictions for two-photon exchange," Phys. Rev. D **79**, 034001.

Borisyuk, Dmitry, and Alexander Kobushkin (2015), "Two-photon exchange amplitude with πN intermediate states: Spin-1/2 and spin-3/2 channels," Phys. Rev. C **92** (3), 035204.

Borisyuk, Dmitry, and Alexander Kobushkin (2020), "Re-analysis of low-energy electron-proton scattering data and proton radius," Nuclear Physics A **1002**, 121998.

Bourzeix, S, *et al.* (1996), "High Resolution Spectroscopy of the Hydrogen Atom: Determination of the 1S Lamb Shift," Phys. Rev. Lett. **76**, 384.

Breidenbach, Martin, Jerome I. Friedman, Henry W. Kendall, Elliott D. Bloom, D. H. Coward, H. C. DeStaebler, J. Drees, Luke W. Mo, and Richard E. Taylor (1969), "Observed behavior of highly inelastic electron-proton scattering," Phys. Rev. Lett. **23**, 935–939.

Breit, G (1929), "The Effect of Retardation on the Interaction of Two Electrons," Phys. Rev. **34**, 553–573.

Breit, G (1930), "The Fine Structure of HE as a Test of the Spin Interactions of Two Electrons," Phys. Rev. **34**, 383–397.

Breit, G (1932), "Dirac's Equation and the Spin-Spin Interactions of Two Electrons," Phys. Rev. **39**, 616–624.

Brock, J, G Gnanvo, P. Hemler, D. Kashy, N. Liyanage, G. Swift, and others. (2021), additional people who contributed to the PRad setup drawing (Fig. 14 of this work).

Brodsky, Stanley J, Guy F. de Teramond, Hans Gunter Dosch, and Joshua Erlich (2015), "Light-Front Holographic QCD and Emerging Confinement," Phys. Rept. **584**, 1–105.

Burkardt, M (2000), "Impact parameter dependent parton distributions and off forward parton distributions for zeta —> 0," Phys. Rev. D **62**, 071503, [Erratum: Phys.Rev.D 66, 119903 (2002)].

Burkardt, M (2003), "Impact parameter space interpretation for generalized parton distributions," Int. J. Mod. Phys. A **18**, 173–208.

Burkardt, M (2006), "Hadron Tomography," International Journal of Modern Physics A **21**, 926–929.

Caiazza, S S, *et al.* (2020), "The MAGIX focal plane time projection chamber," J. Phys. Conf. Ser. **1498**, 012022.

Carlson, Carl E (2015), "The Proton Radius Puzzle," Prog. Part. Nucl. Phys. **82**, 59–77.

Carlson, Carl E, Vladyslav Pauk, and Marc Vanderhaeghen (2019), "Dilepton photoproduction on a deuteron target," Phys. Lett. B **797**, 134872.

Carlson, Carl E, and Marc Vanderhaeghen (2007), "Two-Photon Physics in Hadronic Processes," Ann. Rev. Nucl. Part. Sci. **57**, 171–204.

Carlson, Carl E, and Marc Vanderhaeghen (2008), "Empirical transverse charge densities in the nucleon and the nucleon-to-Delta transition," Phys. Rev. Lett. **100**, 032004, arXiv:0710.0835 [hep-ph].

Carlson, Carl E, and Marc Vanderhaeghen (2009), "Empirical transverse charge densities in the deuteron," Eur. Phys. J. A **41**, 1–5.

Carlson, Carl E, and Marc Vanderhaeghen (2011), "Higher-order proton structure corrections to the Lamb shift in muonic hydrogen," Phys. Rev. A **84**, 020102.

Cates, G D, C. W. de Jager, S. Riordan, and B. Wojtsekhowski (2011), "Flavor decomposition of the elastic nucleon electromagnetic form factors," Phys. Rev. Lett. **106**, 252003.

Chen, Y C, A. Afanasev, S. J. Brodsky, C. E. Carlson, and M. Vanderhaeghen (2004), "Partonic calculation of the two photon exchange contribution to elastic electron proton scattering at large momentum transfer," Phys. Rev. Lett. **93**, 122301.

Christy, M E, *et al.* (E94110) (2004), "Measurements of electron proton elastic cross-sections for 0.4 < Q**2 < 5.5 (GeV/c)**2," Phys. Rev. C **70**, 015206.

Chung, P L, W. N. Polyzou, F. Coester, and B. D. Keister (1988), "Hamiltonian Light Front Dynamics of Elastic electron Deuteron Scattering," Phys. Rev. C **37**, 2000–2015.

Cline, E, J. Bernauer, E. J. Downie, and R. Gilman (2021), "Muse: The muon scattering experiment," doi:10.21468/SciPostPhysProc.2.

Crawford, C, *et al.* (2007), "Measurement of the Proton's Electric to Magnetic Form Factor Ratio from ${}^1\vec{H}(\vec{e},e')$," Phys. Rev. Lett. **98**, 052301.

Cui, Zhu-Fang, Daniele Binosi, Craig D Roberts, and Sebastian M Schmidt (2021), "Fresh extraction of the proton charge radius from electron scattering," arXiv:2102.01180 [hep-ph].

De Rujula, A, J. M. Kaplan, and E. De Rafael (1971), "Elastic scattering of electrons from polarized protons and inelastic electron scattering experiments," Nucl. Phys. B **35**, 365–389.

Diehl, M (2002), "Generalized parton distributions in impact parameter space," Eur. Phys. J. C **25**, 223–232.

Diehl, M (2003a), "Generalized parton distributions," Phys. Rept. **388**, 41–277.

Diehl, M (2003b), "Generalized parton distributions in impact parameter space," Eur. Phys. J. C **31**, 277.

Djukanovic, D, T. Harris, G. von Hippel, P. M. Junnarkar, H. B. Meyer, D. Mohler, K. Ottnad, T. Schulz, J. Wilhelm, and H. Wittig (2021), "Isovector electromagnetic form factors of the nucleon from lattice QCD and the proton radius puzzle," arXiv:2102.07460 [hep-lat].

Donnelly, T W, and A. S. Raskin (1986), "Considerations of polarization in inclusive electron scattering from nuclei," Annuals of Physics **169**, 247–351.

Dreisbach, Christian, *et al.* (COMPASS++/AMBER working group) (2019), "Measuring the Proton Radius in High-Energy Muon-Proton Scattering," PoS **DIS2019**, 222.

Drell, S D, and Tung-Mow Yan (1970), "Connection of Elastic Electromagnetic Nucleon Form-Factors at Large Q**2 and Deep Inelastic Structure Functions Near Threshold," Phys. Rev. Lett. **24**, 181–185.

Dudek, J, *et al.* (2012), "Physics Opportunities with the 12 GeV Upgrade at Jefferson Lab," The European Physical Journal A **48**, 187.

Dye, Steven P, Matthew Gonderinger, and Gil Paz (2016), "Elements of QED-NRQED effective field theory: NLO scattering at leading power," Phys. Rev. D **94** (1), 013006.

Eides, MI, Grotch H Shelyuto VA (2001), "Theory of light hydrogenlike atoms," Physics Reports **342**, 63–261.

Ernst, FJ, Sachs RG, and K.C. Wali (1960), "Electromagnetic Form Factors of the Nucleon," Phys. Rev. **119**, 1105.

Fleurbaey, Hélène, *et al.* (2018), "New Measurement of the $1S-3S$ Transition Frequency of Hydrogen: Contribution to the Proton Charge Radius Puzzle," Phys. Rev. Lett. **120**, 183001.

Foldy, L L, Wouthuysen S A (1950), "On the Dirac Theory of Spin 1/2 Particles and Its Non-Relativistic Limit," Phys. Rev. **99**, 29–36.

Gao, H (2003), "Nucleon Electromagnetic Form Factors," International Journal of Modern Physics E **12**, 1–40.

Gao, H, *et al.* (2015), "Proton remains puzzling," The Universe **3**, 18.

Gasparian, A, H. Gao, D. Dutta, N. Liyanage, E. Pasyuk, D. W. Higinbotham, C. Peng, K. Gnanvo, W. Xiong, X. Bai, and the PRad collaboration (2020), "Prad-ii: A new upgraded high precision measurement of the proton charge radius," arXiv:2009.10510 [nucl-ex].

Gayou, O, *et al.* (Jefferson Lab Hall A) (2002), "Measurement of G(Ep) / G(Mp) in polarized-e p —> e polarized-p to Q**2 = 5.6-GeV**2," Phys. Rev. Lett. **88**, 092301.

Gilman, R, *et al.* (MUSE) (2013), "Studying the Proton "Radius" Puzzle with μ p Elastic Scattering," arXiv:1303.2160 [nucl-ex].

Gilman, R, *et al.* (MUSE) (2017), "Technical Design Report for the Paul Scherrer Institute Experiment R-12-01.1: Studying the Proton "Radius" Puzzle with μp Elastic Scattering," arXiv:1709.09753 [physics.ins-det].

Goeke, K, Maxim V. Polyakov, and M. Vanderhaeghen (2001), "Hard exclusive reactions and the structure of hadrons," Prog. Part. Nucl. Phys. **47**, 401–515.

Gorchtein, M, Pierre A. M. Guichon, and M. Vanderhaeghen (2004), "Beam normal spin asymmetry in elastic lepton-nucleon scattering," Nucl. Phys. A **741**, 234–248.

Gou, B, *et al.* (2020), "Study of Two-Photon Exchange via the Beam Transverse Single Spin Asymmetry in Electron-Proton Elastic Scattering at Forward Angles over a Wide Energy Range," Phys. Rev. Lett. **124** (12), 122003.

Gourdin, M (1963), "Deuteron electromagnetic form factors," Nuovo Cimento **28**, 533.

Graczyk, Krzysztof M, and Cezary Juszczak (2014), "Proton radius from bayesian inference," Phys. Rev. C **90**, 054334.

Gramolin, Alexander V, and Rebecca L. Russell (2021), "Transverse charge density and the radius of the proton," arXiv:2102.13022 [nucl-ex].

Grieser, S, *et al.* (2018), "A Cryogenic Supersonic Jet Target for Electron Scattering Experiments at MAGIX@MESA and MAMI," Nucl. Instrum. Meth. A **906**, 120–126.

Griffioen, K, Carlson C, and S. Maddox (2016), "Consistency of electron scattering data with a small proton radius," Phys. Rev. C. **93**, 065207.

Grinin, Alexey, Arthur Matveev, Dylan C. Yost, Lothar Maisenbacher, Vitaly Wirthl, Randolf Pohl, Theodor W. Hänsch, and Thomas Udem (2020), "Two-photon frequency comb spectroscopy of atomic hydrogen," Science **370** (6520), 1061–1066.

Gryniuk, Oleksii, Sylvester Joosten, Zein-Eddine Meziani, and Marc Vanderhaeghen (2020), "Υ photoproduction on the proton at the Electron-Ion Collider," Phys. Rev. D **102** (1), 014016.

Gryniuk, Oleksii, and Marc Vanderhaeghen (2016), "Accessing the real part of the forward J/ψ-p scattering amplitude from J/ψ photoproduction on protons around threshold," Phys. Rev. D **94** (7), 074001.

Guichon, Pierre A M, and Marc Vanderhaeghen (2003), "How to reconcile the Rosenbluth and the polarization transfer method in the measurement of the proton form-factors," Phys. Rev. Lett. **91**, 142303.

Guidal, Michel, Hervé Moutarde, and Marc Vanderhaeghen (2013), "Generalized Parton Distributions in the valence region from Deeply Virtual Compton Scattering," Rept. Prog. Phys. **76**, 066202.

Gülker, P, *et al.* (2019), "Development of large area focal plane detectors for MAGIX," arXiv:1906.05900 [physics.ins-det].

Guo, Yuxun, Xiangdong Ji, and Kyle Shiells (2021), "Novel twist-three transverse-spin sum rule for the proton and related generalized parton distributions," Nucl. Phys. B **969**, 115440.

Guttmann, Julia, Nikolai Kivel, Mehdi Meziane, and Marc Vanderhaeghen (2011), "Determination of two-photon exchange amplitudes from elastic electron-proton scattering data," Eur. Phys. J. A **47**, 77.

Hagelstein, Franziska (2017), *Exciting Nucleons in Compton Scattering and Hydrogen-Like Atoms*, Other thesis arXiv:1710.00874 [nucl-th].

Hagelstein, Franziska, Rory Miskimen, and Vladimir Pascalutsa (2016), "Nucleon Polarizabilities: from Compton Scattering to Hydrogen Atom," Prog. Part. Nucl. Phys. **88**, 29–97.

Hagelstein, Franziska, and Vladimir Pascalutsa (2019), "Lower bound on the proton charge radius from electron scattering data," Physics Letters B **797**, 134825.

Hagley, E W, and F.M. Pipkin (1994), "Separated oscillatory field measurement of hydrogen 2S1/2-2P3/2 fine structure interval," Phys. Rev. Lett. **72**, 1172.

Hand, L N, Miller DG, and Richard Wilson (1963), "Electric and Magnetic Form Factors of the Nucleon," Rev. of Modern Phys. **35**, 335.

Hasan, Nesreen, Jeremy Green, Stefan Meinel, Michael Engelhardt, Stefan Krieg, John Negele, Andrew Pochinsky, and Sergey Syritsyn (2018), "Computing the nucleon charge and axial radii directly at $Q^2 = 0$ in lattice QCD," Phys. Rev. D **97** (3), 034504.

Hasell, D, *et al.* (2011), "Spin-Dependent Electron Scattering from Polarized Protons and Deuterons with the BLAST Experiment at MIT-Bates," Ann. Rev. Nucl. Part. Sci. **61**, 409.

Hatta, Yoshitaka, and Di-Lun Yang (2018), "Holographic J/ψ production near threshold and the proton mass problem," Phys. Rev. D **98**, 074003.

Hayward, Timothy B, and Keith A. Griffioen (2020), "Evaluation of low-Q^2 fits to ep and ed elastic scattering data," Nucl. Phys. A **999**, 121767.

Henderson, B S, *et al.* (OLYMPUS) (2017), "Hard Two-Photon Contribution to Elastic Lepton-Proton Scattering: Determined by the OLYMPUS Experiment," Phys. Rev. Lett. **118** (9), 092501.

Hernandez, OJ, A. EkstrÃ¶m, N. Nevo Dinur, C. Ji, S. Bacca, and N. Barnea (2018), "The deuteron-radius puzzle is alive: A new analysis of nuclear structure uncertainties," Physics Letters B **778**, 377–383.

Higinbotham, Douglas W, Al Amin Kabir, Vincent Lin, David Meekins, Blaine Norum, and Brad Sawatzky (2016), "Proton radius from electron scattering data," Phys. Rev. C **93**, 055207.

Hill, Richard J, Gabriel Lee, Gil Paz, and Mikhail P. Solon (2013), "NRQED Lagrangian at order $1/M^4$," Phys. Rev. D **87**, 053017.

Hill, Richard J, and Gil Paz (2010), "Model-independent extraction of the proton charge radius from electron scattering," Phys. Rev. D **82**, 113005.

Hill, Richard J, and Gil Paz (2011), "Model Independent Analysis of Proton Structure for Hydrogenic Bound States," Phys. Rev. Lett. **107**, 160402.

Hoferichter, M, B. Kubis, J. Ruiz de Elvira, H. W. Hammer, and U. G. Meißner (2016a), "On the $\pi\pi$ continuum in the nucleon form factors and the proton radius puzzle," Eur. Phys. J. A **52** (11), 331.

Hoferichter, Martin, Jacobo Ruiz de Elvira, Bastian Kubis, and Ulf-G. Meißner (2016b), "Roy–Steiner-equation analysis of pion–nucleon scattering," Phys. Rept. **625**, 1–88.

Hofstadter, R, and R.W. McAllister (1955), "Electron scattering from the proton," Phys. Rev. **98**, 217.

Horbatsch, M, and E. A. Hessels (2016a), "Evaluation of the strength of electron-proton scattering data for determining the proton charge radius," Phys. Rev. C **93**, 015204.

Horbatsch, M, and E. A. Hessels (2016b), "Tabulation of the bound-state energies of atomic hydrogen," Phys. Rev. A **93**, 022513.

Horbatsch, Marko (2020), "Properties of the Sachs electric form factor of the proton on the basis of recent e-p scattering experiments and hydrogen spectroscopy," Physics Letters B **804**, 135373.

Horbatsch, Marko, Eric A. Hessels, and Antonio Pineda (2017), "Proton radius from electron-proton scattering and chiral perturbation theory," Phys. Rev. C **95**, 035203.

Hoyer, Paul (2009), "Bound states at lowest order in hbar," arXiv:0909.3045 [hep-ph].

Huber, A, Th. Udem, B. Gross, J. Reichert, M. Kourogi, K. Pachucki, M. Weitz, and T. W. Hänsch (1998), "Hydrogen-Deuterium $1S-2S$ Isotope Shift and the Structure of the Deuteron," Phys. Rev. Lett. **80**, 468–471.

Hug, Florian, Kurt Aulenbacher, Simon Friederich, Philipp Heil, Robert Heine, Ruth Kempf, Christoph Matejcek, and Daniel Simon (2020), "Status of the MESA ERL Project," in *63rd ICFA Advanced Beam Dynamics Workshop on Energy Recovery Linacs*.

Jaffe, Robert L (2021), "Ambiguities in the definition of local spatial densities in light hadrons," Phys. Rev. D **103** (1), 016017.

Jang, Yong-Chull, Rajan Gupta, Huey-Wen Lin, Boram Yoon, and Tanmoy Bhattacharya (2020), "Nucleon electromagnetic form factors in the continuum limit from (2+1+1)-flavor lattice QCD," Phys. Rev. D **101** (1), 014507.

Jankus, V Z (1956), "Calculation of Electron-Deuteron Scattering Cross Sections," Phys. Rev. **102**, 1586–1591.

Jarvinen, M (2005), "The Hydrogen atom in relativistic motion," Phys. Rev. D **71**, 085006.

Jefferson Lab Proposal E12-12-006, Spokespersons: K. Hafidi, X. Qian, N. Sparveris, Z.-E. Meziani (contact), and Z. W. Zhao, (2012), "Near Threshold Electroproduction of J/Ψ at 11 GeV,".

Jefferson Lab Proposal PR12-20-004, Spokespersons: D. Dutta, H. Gao, A. Gasparian (contact), K. Gnanvo, D. Higinbotham, N. Liyanage, E. Pasyuk, and C. Peng, (2020), "PRad-II: A New Upgraded High Precision Measurement of the Proton Charge Radius,".

Jefferson Lab Proposal PR12-20-006, Spokespersons: D. Dutta, H. Gao, A. Gasparian (contact), D. Higinbotham, N. Liyanage, and E. Pasyuk, (2020), "Precision Deuteron Charge Radius Measurement with Elastic Electron-Deuteron Scattering,".

Jentschura, UD (2011), "Lamb shift in muonic hydrogenÃ¢ÂÂI. Verification and update of theoretical predictions," Annals of Physics **326** (2), 500 – 515.

Jentschura, UD, A. Matveev, C.G. Parthey, J. Alnis, R. Pohl, Th. Udem, N. Kolachevsky, and T.W. Hänsch (2011), "Hydrogen-deuterium isotope shift: From the $1S-2S$-transition frequency to the proton-deuteron charge-radius difference," Phys. Rev. A **83**, 042505.

Ji, X (2003), "Viewing the proton through 'color' filters," Phys. Rev. Lett. **91**, 062001.

Ji, Xiang-Dong (1997a), "Deeply virtual Compton scattering," Phys. Rev. D **55**, 7114–7125.

Ji, Xiang-Dong (1997b), "Gauge-Invariant Decomposition of Nucleon Spin," Phys. Rev. Lett. **78**, 610–613.

Ji, Xiangdong (1995), "QCD Analysis of the Mass Structure of the Nucleon," Phys. Rev. Lett. **74**, 1071–1074.

Ji, Xiangdong, Feng Yuan, and Yong Zhao (2020), "Proton spin after 30 years: what we know and what we don't?" arXiv:2009.01291 [hep-ph].

Jones, M K, *et al.* (Jefferson Lab Hall A) (2000), "G(E(p)) / G(M(p)) ratio by polarization transfer in polarized e p —> e polarized p," Phys. Rev. Lett. **84**, 1398–1402.

Kalinowski, Marcin (2019), "Deuteron charge radius from the lamb-shift measurement in muonic deuterium," Phys. Rev. A **99**, 030501.

Karr, JP, Marchand D, and E. Voutier (2020), "The proton size," Nature Review Physics **2**, 601–614.

Karshenboim, S G, Korzinin E Yu Ivanov V G Shelyuto V A (2010), "Contribution of light-by-light scattering to energy levels of light muonic atoms," JETP Letters **92**, 8–14.

Karshenboim, Savely G, Vladimir G. Ivanov, and Evgeny Yu. Korzinin (2012), "Relativistic recoil corrections to the electron-vacuum-polarization contribution in light muonic atoms," Phys. Rev. A **85**, 032509.

Kato, K, T. D. G. Skinner, and E. A. Hessels (2018), "Ultrahigh-Precision Measurement of the $n=2$ Triplet P Fine Structure of Atomic Helium Using Frequency-Offset Separated Oscillatory Fields," Phys. Rev. Lett. **121**, 143002.

Kelly, J J (2004), "Simple parametrization of nucleon form factors," Phys. Rev. C **70**, 068202.

Kharzeev, D, H. Satz, A. Syamtomov, and G. Zinovjev (1999), "J/ψ photoproduction and the gluon structure of the nucleon," Eur. Phys. J. C **9**, 459–462.

Kivel, N, and M. Vanderhaeghen (2013), "Two-photon exchange corrections to elastic electron-proton scattering at large momentum transfer within the SCET approach," JHEP **04**, 029.

Kivel, Nikolai, and Marc Vanderhaeghen (2009), "Two-photon exchange in elastic electron-proton scattering: QCD factorization approach," Phys. Rev. Lett. **103**, 092004.

Kogut, JB, and D. Soper (1970), "Quantum Electrodynamics in the Infinite-Momentum Frame," Phys. Rev. D. **1**, 2901.

Kraus, E, K. E. Mesick, A. White, R. Gilman, and S. Strauch (2014), "Polynomial fits and the proton radius puzzle," Phys. Rev. C **90**, 045206.

Kuhn, S, *et al.* (2009), "Spin structure of the nucleon–status and recent results," Progress in Nuclear and Particle Physics **63**, 1–50.

Kumar, K S, Sonny Mantry, W. J. Marciano, and P. A. Souder (2013), "Low Energy Measurements of the Weak Mixing Angle," Ann. Rev. Nucl. Part. Sci. **63**, 237–267.

Kumericki, Kresimir, Simonetta Liuti, and Herve Moutarde (2016), "GPD phenomenology and DVCS fitting: Entering the high-precision era," Eur. Phys. J. A **52** (6), 157.

Larin, I, *et al.* (PrimEx Collaboration) (2011), "New Measurement of the π^0 Radiative Decay Width," Phys. Rev. Lett. **106**, 162303.

Larin, I, *et al.* (2020), "Precision measurement of the neutral pion lifetime," Science **368** (6490), 506–509.

Lee, Gabriel, John R. Arrington, and Richard J. Hill (2015), "Extraction of the proton radius from electron-proton scattering data," Phys. Rev. D **92**, 013013.

Lensky, Vadim, Franziska Hagelstein, Vladimir Pascalutsa, and Marc Vanderhaeghen (2018), "Sum rules across the unpolarized Compton processes involving generalized polarizabilities and moments of nucleon structure functions," Phys. Rev. D **97** (7), 074012.

Lin, Yong-Hui, Hans-Werner Hammer, and Ulf-G Meißner (2021), "High-precision determination of the electric and magnetic radius of the proton," Phys. Lett. B **816**, 136254.

Lorcé, C (2009), "Electromagnetic properties for arbitrary spin particles: Natural electromagnetic moments from light-cone arguments," Phys. Rev. D **79**, 113011.

Lorcé, C (2018), "On the hadron mass decomposition," The European Physical Journal C **78**, 120.

Lorcé, C, and B. Pasquini (2011), "Quark Wigner Distributions and Orbital Angular Momentum," Phys. Rev. D **84**, 014015.

Lorcé, Cédric (2020), "Charge Distributions of Moving Nucleons," Phys. Rev. Lett. **125** (23), 232002.

Lorcé, C, Pasquini B, and M. Vanderhaeghen (2011), "Unified framework for generalized and transverse-momentum dependent parton distributions within a 3Q light-cone picture of the nucleon," Journal of High Energy Physics **05**, 041.

Lorcé, C, Pasquini B Xiong X, and F. Yuan (2012), "The quark orbital angular momentum from Wigner distributions and light-cone wave functions," Phys. Rev. D **85**, 114006.

Lorenz, I T, Hammer H-W, and Ulf-G. Meissner (2012), "The size of the proton: Closing in on the radius puzzle," The European Physical Journal A **48**, 151–156.

Lorenz, I T, Ulf-G. Meißner, H.-W. Hammer, and Y.-B. Dong (2015), "Theoretical constraints and systematic effects in the determination of the proton form factors," Phys. Rev. D **91**, 014023.

Lorenz, I T, Meissner Ulf-G (2014), "Reduction of the proton radius discrepancy by 3σ," Physics Letters B **737**, 57–59.

Maas, F E, *et al.* (2005), "Measurement of the transverse beam spin asymmetry in elastic electron proton scattering and the inelastic contribution to the imaginary part of the two-photon exchange amplitude," Phys. Rev. Lett. **94**, 082001.

Matveev, Arthur, *et al.* (2013), "Precision Measurement of the Hydrogen $1S-2S$ Frequency via a 920-km Fiber Link," Phys. Rev. Lett. **110**, 230801.

Maximon, L C (1969), "Comments on Radiative Corrections," Rev. of Modern Phys. **41**, 193.

McAllister, RW, and R. Hofstadter (1956), "Elastic scattering of 188-mev electrons from the proton and the alpha particle," Phys. Rev. **102**, 851.

Meissner, S, Metz A, and M. Schlegel (2009), "Generalized parton correlation functions for a spin-1/2 hadron," Journal of High Energy Physics **08**, 056.

Meissner, S, Metz A Schlegel-M, and K. Goeke (2008), "Generalized parton correlation functions for a spin-0 hadron," Journal of High Energy Physics **08**, 038.

Melnikov, K, van Ritbergen T (2000), "Three-Loop Slope of the Dirac Form Factor of the 1S Lamb Shift in Hydrogen," Phys. Rev. Lett. **84**, 1673.

Metz, Andreas, Barbara Pasquini, and Simone Rodini (2020), "Revisiting the proton mass decomposition," Phys. Rev. D **102**, 114042.

Meziane, M, *et al.* (GEp2gamma) (2011), "Search for effects beyond the Born approximation in polarization transfer observables in $\vec{e}p$ elastic scattering," Phys. Rev. Lett. **106**, 132501.

Mihovilovič, M, *et al.* (2017), "First measurement of proton's charge form factor at very low Q2 with initial state radiation," Physics Letters B **771**, 194 – 198.

Mihovilovič, M, *et al.* (2021), "The proton charge radius extracted from the initial-state radiation experiment at MAMI," Eur. Phys. J. A **57** (3), 107.

Miller, G A (2019), "Defining the proton radius: A unified treatment," Phys. Rev. C **99**, 035202.

Miller, Gerald A (2007), "Charge Density of the Neutron," Phys. Rev. Lett. **99**, 112001.

Mo, L W, and Y.-S. Tsai (1969), "Radiative Corrections to Elastic and Inelastic ep and μp Scattering," Rev. of Modern Phys. **41**, 205.

Mohr, Peter J, David B. Newell, and Barry N. Taylor (2016), "CODATA Recommended Values of the Fundamental Physical Constants: 2014," Journal of Physical and Chemical Reference Data **45** (4), 043102.

Mohr, P J, Taylor BN-Newell DB (2008), "CODATA recommended values of the fundamental physical constants: 2006*," Rev. Modern Physics **80**, 633–730.

Mohr, P J, Taylor BN-Newell DB (2012), "CODATA recommended values of the fundamental physical constants: 2010*," Rev. Modern Physics **84**, 1527.

Müller, Dieter, D. Robaschik, B. Geyer, F.-M. Dittes, and J. Hořejši (1994), "Wave functions, evolution equations and evolution kernels from light ray operators of QCD," Fortsch. Phys. **42**, 101–141.

Murphy, J J, Y. M. Shin, and D. M. Skopik (1974a), "Erratum: Proton form factor from 0.15 to 0.79 fm^{-2}," Phys.

Rev. C **10**, 2111–2111.

Murphy, J J, Y. M. Shin, and D. M. Skopik (1974b), "Proton form factor from 0.15 to 0.79 fm-2," Phys. Rev. C **9**, 2125–2129, [Erratum: Phys.Rev.C 10, 2111–2111 (1974)].

Murphy, J J, Y. M. Shin, and D. M. Skopik (1974c), "Proton form factor from 0.15 to 0.79 fm^{-2}," Phys. Rev. C **9**, 2125–2129.

Pachucki, Krzysztof (1996), "Theory of the Lamb shift in muonic hydrogen," Phys. Rev. A **53**, 2092–2100.

Pachucki, Krzysztof (1999), "Proton structure effects in muonic hydrogen," Phys. Rev. A **60**, 3593–3598.

Pachucki, Krzysztof, Vojt ěch Patkóš, and Vladimir A. Yerokhin (2018), "Three-photon-exchange nuclear structure correction in hydrogenic systems," Phys. Rev. A **97**, 062511.

Paolone, M, *et al.* (E03-104 Collaboration) (2010), "Polarization Transfer in the ^{4}He($\vec{e}, e' \vec{p}$)^{3}H Reaction at $Q^2 = 0.8$ and 1.3 (GeV/c)^2," Phys. Rev. Lett. **105**, 072001.

Parthey, Christian G, Arthur Matveev, Janis Alnis, Randolf Pohl, Thomas Udem, Ulrich D. Jentschura, Nikolai Kolachevsky, and Theodor W. Hänsch (2010), "Precision Measurement of the Hydrogen-Deuterium $1S-2S$ Isotope Shift," Phys. Rev. Lett. **104**, 233001.

Parthey, Christian G, *et al.* (2011), "Improved Measurement of the Hydrogen $1S--2S$ Transition Frequency," Phys. Rev. Lett. **107**, 203001.

Pasquini, B, and M. Vanderhaeghen (2004), "Resonance estimates for single spin asymmetries in elastic electron-nucleon scattering," Phys. Rev. C **70**, 045206.

Pauk, Vladyslav, and Marc Vanderhaeghen (2015), "Lepton universality test in the photoproduction of e^-e^+ versus $\mu^-\mu^+$ pairs on a proton target," Phys. Rev. Lett. **115** (22), 221804.

Perdrisat, C F, V. Punjabi, and M. Vanderhaeghen (2007), "Nucleon Electromagnetic Form Factors," Prog. Part. Nucl. Phys. **59**, 694–764.

Peset, Clara, and Antonio Pineda (2014), "The two-photon exchange contribution to muonic hydrogen from chiral perturbation theory," Nucl. Phys. B **887**, 69–111.

Pierce, J, *et al.* (2021), "The PRad Windowless Gas Flow Target," arXiv:2103.01749 [Physics-Instrumentation and Detectors].

Pineda, Antonio (2003), "Leading chiral logs to the hyperfine splitting of the hydrogen and muonic hydrogen," Phys. Rev. C **67**, 025201.

Pohl, R, *et al.* (2010), "The size of the proton," Nature **466**, 213–216.

Pohl, Randolf, Ronald Gilman, Gerald A. Miller, and Krzysztof Pachucki (2013), "Muonic hydrogen and the proton radius puzzle," Ann. Rev. Nucl. Part. Sci. **63**, 175–204.

Pohl, Randolf, François Nez, Thomas Udem, Aldo Antognini, Axel Beyer, Hélène Fleurbaey, Alexey Grinin, Theodor W Hänsch, Lucile Julien, Franz Kottmann, Julian J Krauth, Lothar Maisenbacher, Arthur Matveev, and François Biraben (2017), "Deuteron charge radius and Rydberg constant from spectroscopy data in atomic deuterium," Metrologia **54** (2), L1–L10.

Pohl, Randolf, *et al.* (2016), "Laser spectroscopy of muonic deuterium," Science **353** (6300), 669–673.

Puckett, A J R, *et al.* (2010), "Recoil Polarization Measurements of the Proton Electromagnetic Form Factor Ratio to $Q^2 = 8.5$ GeV^2," Phys. Rev. Lett. **104**, 242301.

Punjabi, V, *et al.* (2005), "Proton elastic form-factor ratios to Q**2 = 3.5-GeV**2 by polarization transfer," Phys. Rev. C **71**, 055202, [Erratum: Phys.Rev.C 71, 069902 (2005)].

Rachek, I A, *et al.* (2015), "Measurement of the two-photon exchange contribution to the elastic $e^{\pm}p$ scattering cross sections at the VEPP-3 storage ring," Phys. Rev. Lett. **114** (6), 062005.

Radyushkin, AV (1996), "Scaling limit of deeply virtual Compton scattering," Phys. Lett. B **380**, 417–425.

Ramsey, Norman F (1949), "A New Molecular Beam Resonance Method," Phys. Rev. **76**, 996–996.

Rimal, D, *et al.* (CLAS) (2017), "Measurement of two-photon exchange effect by comparing elastic $e^{\pm}p$ cross sections," Phys. Rev. C **95** (6), 065201.

Rinehimer, Jared A, and Gerald A. Miller (2009), "Connecting the breit frame to the infinite momentum light front frame: How G_E turns into F_1," Phys. Rev. C **80**, 015201.

Riordan, Michael (1992), "The discovery of quarks," Science **256**, 1287.

Ron, G, *et al.* (2011), "Low-Q^2 measurements of the proton form factor ratio μ_pGE/GM," Phys. Rev. C. **84**, 055204.

Rosenbluth, MN (1950), "High Energy Elastic Scattering of Electrons on Protons," Phys. Rev. **79**, 615.

Sachs, RG (1962), "High-Energy Behavior of Nucleon Electromagnetic Form Factors," Phys. Rev. **126**, 2256.

Sato, Yutaro (2017), "muon g-2/EDM experiment at J-PARC," PoS **KMI2017**, 006.

Schlimme, B S, *et al.* (2016), "Deuteron form factor measurements at low momentum transfers," EPJ Web Conf. **113**, 04017.

Schlimme, B S, *et al.* (2021), "Operation and characterization of a windowless gas jet target in high-intensity electron beams," arXiv:2104.13503 [physics.ins-det].

Schwob, C, *et al.* (1999), "Optical Frequency Measurement of the 2S–12D Transitions in Hydrogen and Deuterium: Rydberg Constant and Lamb Shift Determinations," Phys. Rev. Lett. **82**, 4960.

Shifman, MA, A.I. Vainshtein, and V.I. Zakharov (1978), "Remarks on higgs-boson interactions with nucleons," Physics Letters B **78** (4), 443 – 446.

Shintani, Eigo, Ken-Ichi Ishikawa, Yoshinobu Kuramashi, Shoichi Sasaki, and Takeshi Yamazaki (2019), "Nucleon form factors and root-mean-square radii on a (10.8 fm)^4 lattice at the physical point," Phys. Rev. D **99** (1), 014510, [Erratum: Phys.Rev.D 102, 019902 (2020)].

Sick, Ingo (2018), "Proton charge radius from electron scattering," Atoms **6** (1), 2.

Sick, Ingo, and Dirk Trautmann (1998), "On the rms radius of the deuteron," Nuclear Physics A **637** (4), 559 – 575.

Sick, Ingo, and Dirk Trautmann (2017), "Reexamination of proton rms radii from low-q power expansions," Phys. Rev. C **95**, 012501.

Simon, G G, *et al.* (1980), "Absolute electron-proton cross sections at low momentum transfer measured with a high pressure gas target system," Nuclear Physics A **333**, 381–391.

Sokhoyan, Vahe (2020), "private communication,".

Soper, D (1977), "Parton model and the Bethe-Salpeter wave function," Phys. Rev. D. **15**, 1141–1149.

Suda, T., (2018), "Elastic electron scattering off protonusing 60 MeV electron linac of Tohoku University," .

Sufian, Raza Sabbir, Guy F. de Téramond, Stanley J. Brodsky, Alexandre Deur, and Hans Günter Dosch (2017), "Analysis of nucleon electromagnetic form factors from light-front holographic QCD : The spacelike region," Phys.

Rev. D **95** (1), 014011.

Tiesinga, Eite, Peter J. Mohr, David B. Newell, and Barry N. Taylor (2021), "Codata recommended values of the fundamental physical constants: 2018," Rev. Mod. Phys. **93**, 025010.

Tomalak, O, B. Pasquini, and M. Vanderhaeghen (2017a), "Two-photon exchange corrections to elastic e^--proton scattering: Full dispersive treatment of πN states at low momentum transfers," Phys. Rev. D **95** (9), 096001.

Tomalak, Oleksandr, Barbara Pasquini, and Marc Vanderhaeghen (2017b), "Two-photon exchange contribution to elastic e^- -proton scattering: Full dispersive treatment of πN states and comparison with data," Phys. Rev. D **96** (9), 096001.

Volotka, AV, *et al.* (2005), "Zemach and magnetic radius of the proton from the hyperfine splitting in hydrogen," The European Physical Journal D **33**, 23–27.

Vorobyev, A A (2019), "Precision Measurement of the Proton Charge Radius in Electron Proton Scattering," Physics of Particles and Nuclei Letters **16** (5), 524–529.

Vorobyov, AA, and A. Denig (2017), "MAMI A2 Proposal (PRES): High precision measurement of the ep elastic cross section at small Q2,".

Vutha, A C, and E. A. Hessels (2015), "Frequency-offset separated oscillatory fields," Phys. Rev. A **92**, 052504.

Weitz, M, *et al.* (1994), "Precision measurement of the hydrogen and deuterium 1 S ground state Lamb shift," Phys. Rev. Lett. **72**, 328.

Wells, S P, *et al.* (SAMPLE) (2001), "Measurement of the vector analyzing power in elastic electron proton scattering as a probe of double photon exchange amplitudes," Phys. Rev. C **63**, 064001.

van Wijngaarden, A, *et al.* (1998), "Lamb-shift measurement in hydrogen by the anisotropy method," Canadian Journal of Physics **76**, 95.

Xiong, W, *et al.* (2019), "A small proton charge radius from an electron–proton scattering experiment," Nature **575** (7781), 147–150.

Xiong, Weizhi (2020), *A High Precision Measurement of the Proton Charge Radius at JLab*, Ph.D. thesis (Duke University).

Yan, X, *et al.* (2018), "Robust extraction of the proton charge radius from electron-proton scattering data," Phys. Rev. C **98**, 025204.

Ye, Zhihong, John Arrington, Richard J. Hill, and Gabriel Lee (2018), "Proton and neutron electromagnetic form factors and uncertainties," Physics Letters B **777**, 8 – 15.

Zhan, X, *et al.* (2011), "High-precision measurement of the proton elastic form factor ratio $\frac{G_E}{G_M}$ at low Q^2," Physics Letters B **705**, 59–64.

Zhang, Y W, *et al.* (2015), "Measurement of the Target-Normal Single-Spin Asymmetry in Quasielastic Scattering from the Reaction $^3\mathrm{He}^{\uparrow}(e, e')$," Phys. Rev. Lett. **115** (17), 172502.

Zhou, Jingyi, Vladimir Khachatryan, Haiyan Gao, Douglas W. Higinbotham, Asia Parker, Xinzhan Bai, Dipangkar Dutta, Ashot Gasparian, Kondo Gnanvo, Mahbub Khandaker, Nilanga Liyanage, Eugene Pasyuk, Chao Peng, and Weizhi Xiong (2021), "Advanced extraction of the deuteron charge radius from electron-deuteron scattering data," Phys. Rev. C **103**, 024002.

Zhou, Shuang, P. Giulani, J. Piekarewicz, Anirban Bhattacharya, and Debdeep Pati (2019), "Reexamining the proton-radius problem using constrained Gaussian processes," Phys. Rev. C **99**, 055202.

Zyla, P A, *et al.* (Particle Data Group) (2020), "Review of Particle Physics," PTEP **2020** (8), 083C01.